Priscila Ferrari Silveira Rosa

Physical Properties of FeAs-based Intermetallic Compounds

Propriedades Físicas de
Compostos Intermetálicos à base de FeAs

Campinas, 2013

Universidade Estadual de Campinas

Instituto de Física "Gleb Wataghin"

Priscila Ferrari Silveira Rosa

Physical Properties of FeAs-based Intermetallic Compounds

Propriedades Físicas de Compostos Intermetálicos à base de FeAs

Doctorate Thesis/*Tese de Doutorado*

Doctorate thesis presented to the Physics Institute of the University of Campinas to obtain the degree of Doctor of Sciences.

Tese de doutorado apresentada ao Instituto de Física da Universidade Estadual de Campinas para obtenção do título de Doutora em Ciências.

Supervisor/*Orientador*: Prof. Dr. Pascoal José Giglio Pagliuso

Este exemplar corresponde à versão final da tese defendida por Priscila Ferrari Silveira Rosa e orientada pelo Prof. Dr. Pascoal José Giglio Pagliuso.

Campinas, 2013.

Ficha catalográfica
Universidade Estadual de Campinas
Biblioteca do Instituto de Física Gleb Wataghin
Valkíria Succi Vicente - CRB 8/5398

R71p
Rosa, Priscila Ferrari Silveira, 1988-
Physical properties of FeAs-based intermetallic superconductors / Priscila Ferrari Silveira Rosa. – Campinas, SP : [s.n.], 2013.

Orientador: Pascoal José Giglio Pagliuso.
Tese (doutorado) – Universidade Estadual de Campinas, Instituto de Física Gleb Wataghin.

1. Supercondutividade. 2. Antiferromagnetismo. 3. Magnetismo. 4. Compostos intermetálicos. I. Pagliuso, Pascoal José Giglio,1971-. II. Universidade Estadual de Campinas. Instituto de Física Gleb Wataghin. III. Título.

Informações para Biblioteca Digital

Título em outro idioma: Propriedades físicas de supercondutores intermetálicos à base de FeAs
Palavras-chave em inglês:
Superconductivity
Antiferromagnetism
Magnetism
Intermetallic compounds
Área de concentração: Física
Titulação: Doutora em Física
Banca examinadora:
Pascoal José Giglio Pagliuso [Orientador]
Michael Josef Nicklas
Raimundo Rocha dos Santos
Rickson Coelho Mesquita
Alex Antonelli
Data de defesa: 26-07-2013
Programa de Pós-Graduação: Física

IFGW Instituto de Física Gleb Wataghin

UNICAMP

MEMBROS DA COMISSÃO JULGADORA DA TESE DE DOUTORADO DE **PRISCILA FERRARI SILVEIRA ROSA – RA: 087206** APRESENTADA E APROVADA AO INSTITUTO DE FÍSICA "GLEB WATAGHIN", DA UNIVERSIDADE ESTADUAL DE CAMPINAS, EM 26 / 07 / 2013.

COMISSÃO JULGADORA:

Prof. Dr. Pascoal José Giglio Pagliuso
Orientador da Candidata - DEQ/IFGW/UNICAMP

Prof. Dr. Michael Josef Nicklas
Max Planck Institute for Chemical Physics of Solids

Prof. Dr. Raimundo Rocha dos Santos
IF/UFRJ

Prof. Dr. Rickson Coelho Mesquita
DRCC/IFGW/UNICAMP

Alex Antonelli

Prof. Dr. Alex Antonelli
DFMC/IFGW/UNICAMP

Acknowledgments

I would like to first sincerely thank my advisor Prof. Pascoal Pagliuso, for his outstanding guidance and support. His commitment to research was a constant motivation that made this work possible. My sincere thanks to Prof. Zachary Fisk for hosting me at the University of California at Irvine during two very productive months of my PhD. I would also like to show my appreciation to the professors in our group Prof. Carlos Rettori, Prof. Ricardo Urbano, Prof. Eduardo Granado, Prof. Oscar Ferreira de Lima, Prof. Kleber Pirota, Prof. Yakov Kopelevich and Prof. Marcelo Knobel for their time and positive advice toward my research. Furthermore, I would like to acknowledge with much appreciation the crucial role of the staff, especially Celso Alves, Zairo, Milton, Walter, Sérgio and Célia for their continued help. Also, many thanks for the graduate program (CPG) staff: Gilvani, Armando, Luciana, and Alessandra.

A special thanks goes to my friends Pedro (Poca), Victor and Vinícius with whom I have shared great moments of the graduate school journey with lively discussions about physics and about life. Many thanks to my friends at our group (GPOMS): Cris, Wellington, Thales, Lino, Guilherme, César and Camilo for their help and companionship since I arrived at the lab.

I would like to thank my parents Leni and Carmo and my brother Wendell for being a constant source of emotional support.

Finally I would like to thank the funding agency FAPESP for the financial support.

“Fall in love with some activity, and do it! Nobody ever figures out what life is all about, and it doesn’t matter. Explore the world. Nearly everything is really interesting if you go into it deeply enough. Work as hard and as much as you want to on the things you like to do the best. Don’t think about what you want to be, but what you want to do. Keep up some kind of a minimum with other things so that society doesn’t stop you from doing anything at all.”

— Richard P. Feynman

Abstract

The microscopic understanding of the intricate interplay between magnetism and unconventional superconductivity is currently one of the great open questions in condensed matter physics. In particular, compounds with a tetragonal crystal structure seems to be favorable to the emergence of such phenomena. The intermetallic compounds $\mathrm{BaFe_2As_2}$ and $\mathrm{EuFe_2As_2}$ crystallize in the tetragonal $\mathrm{ThCr_2Si_2}$-type structure ($I4/mmm$) with FeAs sheets separated by barium/europium layers. Both compounds exhibit a structural distortion accompanied by a magnetic spin-density wave (SDW) phase transition at $T_{SDW} = 140$ K and $T_{SDW} = 190$ K, respectively. Remarkably, this SDW phase can be tuned toward a superconducting state by substitution and applied pressure. In this thesis, we will present a systematic study of the intermetallic tetragonal compound $\mathrm{BaFe_2As_2}$ as a function of three parameters: Eu substitution in the Ba crystallographic site, transition metal (TM) substitution (TM = Mn, Co, Ni, Cu, and Ru) in the Fe site, and/or applied hydrostatic pressure. For this purpose, we have grown high-quality single crystals by the alternative In-flux method. The macroscopic characterization has been made by measurements of magnetic susceptibility, specific heat and electrical resistivity at ambient pressure and under hydrostatic pressure. Concerning the microscopic investigation, the experimental approach consists in using electron spin resonance (ESR) technique employing paramagnetic ions of $\mathrm{Eu^{2+}}$ and $\mathrm{Mn^{2+}/Cu^{2+}}$ as probes in the Ba and FeAs planes, respectively and X-ray absorption spectroscopy (XANES and EXAFS) in both As and Fe K edges. In this manner, it was possible to study the site specific spin dynamics and its relation with local distortions in the material. Our results evidentiate that the decrease in the Fe-As distance is intimately related to the SDW phase suppression and to a localization of the Fe $3d$ bands in the FeAs plane. This increase in the planar $xy/x^2 - y^2$ orbital character at the Fermi surface appears to be a propitious ingredient to the emergence of superconductivity in this class of materials.

Resumo

O entendimento microscópico da intrincada relação entre magnetismo e supercondutividade não-convencional é atualmente um dos grandes problemas em aberto em física da matéria condensada. Em especial, compostos com estrutura cristalina tetragonal parecem favorecer a emergência de tal fenômeno. Os compostos intermetálicos tetragonais $BaFe_2As_2$ e $EuFe_2As_2$ cristalizam na estrutura tetragonal $ThCr_2Si_2$ ($I4/mmm$) com camadas de FeAs separadas por átomos de bário/európio. Ambos os compostos apresentam uma distorção estrutural (tetragonal para ortorrômbica) acompanhada for uma transição de fase magnética do tipo onda de densidade de spin (ou SDW, na sigla em inglês) em $T_{SDW} = 140$ K e $T_{SDW} = 190$ K, respectivamente. É notável que esta fase magnética pode ser suprimida em direção ao estado supercondutor através de substituição química ou pressão aplicada. Neste trabalho, apresentamos o estudo sistemático das propriedades do composto intermetálico tetragonal $BaFe_2As_2$ em função de três parametros: substituição de Eu no sítio cristalográfico do Ba; substituição de metais de transição TM = Mn, Co, Ni, Cu e Ru no sítio cristalográfico do Fe e/ou pressão hidrostática. Para tal propósito, primeiramente sintetizamos amostras de alta qualidade através do método alternativo de fluxo metálico de In. A caracterização macroscópica dos compostos foi realizada através das técnicas experimentais de medidas de susceptibilidade magnética, calor específico, resistividade elétrica em pressão ambiente e sob pressão hidrostática, além da caracterização estrutural através da difração de pó de raios-X. No que diz respeito à caracterização microscópica, a investigação experimental foi realizada através da técnica de ressonância de *spin* eletrônico (RSE) utilizando como provas os íons paramagnéticos de Eu^{2+} e Mn^{2+}/Cu^{2+}, além do estudo de absorção de raios-X (EXAFS) tanto na borda K do As quanto na borda do Fe. Dessa forma, foi possível investigar a dinâmica de spins no plano e fora do plano de FeAs e sua relação com as distorções locais do material. Nossos resultados evidenciam que a diminuição da distância Fe-As está intimamente ligada à supressão da fase SDW e à localização das bandas $3d$ do Fe no plano Fe-As. O aumento do caráter orbital planar $xy/x^2 - y^2$ na superfície de Fermi parece ser um ingrediente propício para a emergência da supercondutividade nessa classe de compostos.

Contents

Acknowledgments **vii**

Abstract **xi**

Resumo **xiii**

1 Introduction **1**

1.1 Fe-based Superconductors: State of the Art 2

1.2 Specific problem: What is the important tuning parameter in $BaFe_2As_2$? 7

2 Theoretical Aspects **9**

2.1 Magnetism in Solids 9

2.1.1 Paramagnetism 10

2.1.2 Magnetic interactions 14

2.2 Superconductivity 20

2.2.1 Conventional Superconductivity 20

2.2.2 Unconventional Superconductivity 25

2.3 Crystal Field Effects 27

2.4 Electron Spin Resonance 29

3 Experimental Techniques **41**

3.1 Single Crystal Growth 41

3.2 Specific Heat Measurement 43

3.3 Electrical Resistivity Measurement 46

3.3.1 Under Hydrostatic Pressure 47

3.3.2 At High Magnetic Fields: Quantum Oscillations 47

3.4 Magnetic Susceptibility Measurement 49

3.5 X-Ray Absorption Fine Structure Spectroscopy: XANES and EXAFS 51

3.6 Electron Spin Resonance Measurement 55

4 Synthesis and Macroscopic Properties of 122 single crystals 57

4.1 Single Crystal Growth 57

4.2 Macroscopic characterization 62

4.2.1 Electrical Resistivity Measurements Under Hydrostatic Pressure 62

4.2.2 Electrical Resistivity Measurements at High Magnetic Fields 70

5 Microscopic Properties: The Role of Local Distortions 77

5.1 EXAFS and XANES Measurements 77

5.2 ESR Measurements 89

6 Conclusions and Perspectives 111

A List of Publications 115

Bibliography 117

List of Abbreviations

TM:	Transition Metal
SDW:	Spin-Density Wave
AFM:	Antiferromagnetism
SC:	Superconductivity
USC:	Unconventional Superconductivity
$\mathbf{T_c}$:	Superconducting Transition Temperature
$\mathbf{T_{SDW}}$:	Spin-Density Wave Transition Temperature
ESR:	Electron Spin Resonance
NMR:	Nuclear Magnetic Resonance
NQR:	Nuclear Quadrupolar Resonance
CEF:	Crystalline Eletric Field
EXAFS:	Extended X-Ray Absorption Fine Structure
XANES:	X-Ray Near Edge Spectroscopy
ARPES:	Angle-Resolved Photoemission Spectroscopy
FS:	Fermi Surface
$\eta(\mathbf{E_F})$:	Density of States at the Fermi Level
BCS:	Barden, Cooper, and Schrieffer
AG:	Abrikosov-Gorkov
J:	Exchange Interaction
SdH:	Shubnikov-de Haas
dHvA:	de Haas-van Alphen
SQUID:	Superconducting QUantum Interference Device
RRR:	Residual Resistivity Ratio
IFG:	In-flux grown
SFG:	Self-flux grown
TFG:	Tin-flux grown

List of Figures

1.1 Five different structural classes of iron-based superconductors that share a common layered structure based on a planar layer of iron atoms joined by tetrahedrally coordinated pnictogen (P, As) or chalcogen (S, Se, Te) anions arranged in a stacked sequence separated by alkali, alkaline-earth or rare-earth and oxygen/fluorine blocking layers. Figure extracted from ref. [1] 1

1.2 (a,d) Crystal structure and phase diagrams as a function of (b,e) substitution and (c,f) applied pressure for heavy fermion and cuprate compounds. Figures extracted from ref. [5, 6, 7, 8] 3

1.3 Phase diagram for the 122 system as a function of substitution (top) and of applied pressure (bottom). Figure extracted from ref. [9]. 3

1.4 a. Superconducting transition temperatures as a function of tetragonal lattice parameters c/a for various Ce- and Pu-members of the CeMIn$_5$ and PuMGa$_5$ families. Figure from ref. [22]. b. Relationship between T_c and the Cu-O-Cu buckling angle for the CuO$_2$ planes and the Cu-O apical bond distance for compounds with two CuO$_2$ layers. Square symbols are angles; round symbols are distances. Figure from ref. [21] 5

1.5 a) Tetrahedral symmetry in a cubic environment. b) Distorted tetrahedra in the real lattice. The Fe-As distance and the angle α changes among compounds with substitution and pressure. 5

1.6 (left) Fermi surface calculated by DFT+DMFT [23] and (right) Fe 3d orbitals. . . 6

1.7 a) Substitution of Eu^{2+} and Mn^{2+} in the Ba^{2+} and Fe^{2+} crystallographic sites, respectively. b) Specific heat versus temperature of the EuFe$_2$As$_2$ compound displaying antiferromagnetic ordering of the Fe ions at $T_{SDW} = 190$ K and of the Eu ions at $T_N = 19$ K. The inset shows both magnetic structures. Figure extracted from ref. [33]. 8

2.1 Summary of the magnetic susceptibility temperature dependence presented in this section. a) Pauli paramagnetism and diamagnetism; b) Curie paramagnetism; (c) ferromagnetism; (d) antiferromagnetism. Figure extracted from ref. [34]. 15

2.2 The Hartree-Fock radial densities of Gd^{3+} (similar to Eu^{2+}). Figure extracted from ref. [47] 17

2.3 Indirect J_{RKKY} exchange interaction of a free electron gas. 18

2.4 (a) Commensurate spin-density wave with wave vector $q = \pi/a$. (b) Incommensurate spin-density wave. Figure extracted from ref. [63]. 19

2.5 a) The resistivity of a capillary of mercury as a function of temperature. b) Magnetic flux expulsion from the interior of a superconductor (Meissner effect). Figure extracted from ref. [64]. 20

2.6 a) Specific heat of a conventional type-I superconductor: aluminum (Al). Figure extracted from ref. [65]. b) Specific heat of an unconventional superconductor: $CeCoIn_5$. Figure extracted from ref. [66]. 22

2.7 The spin-lattice relaxation rate in the normal and superconducting states. a) $1/T_1$ data for $^{69}Ga(1)$, as well as calculations for BCS isotropic s-wave (dashed), pure (dotted) and dirty (solid) d-wave gap functions. The solid line in the normal state shows $T^{0.35}$. b) $(T_1T)/(T_1T)_0^{-1}$ versus T/T_c for $PuCoGa_5$, as well as for the unconvenctionl cuprate superconductor $YBa_2Cu_3O_7$ ($T_c = 92$ K) and $CeCoIn_5$ ($T_c = 2.3$ K) and s-wave superconductors Al and MgB_2. Figure extracted from ref. [67]. . . 26

2.8 Crystal field scheme for a $3d^6$ Fe^{2+} ion in spherical, tetrahedral and distorted tetrahedral symmetry. 29

2.9 Zeeman splitting as a function of the static applied field H_0 for a single unpaired electron with $L = 0$. In an electron spin resonance measurement, a transverse oscillating magnetic field H_1 is applied and an absorption occcurs when $h\nu = g\mu_B H_{RES}$. 31

2.10 a) Real (dispersion) $\chi'(\omega)$ and imaginary (absorption) $\chi''(\omega)$ components of the spin susceptibility. b) Typical absorption line in a metal (Dysonian) and its observed first derivative. 32

2.11 Relaxation paths involved in the ESR linewidth. 33

2.12 Scattering event which, in part, is responsible for the Korringa relaxation rate. The incoming conduction electron $\mathbf{k}\downarrow$ spin-flips against the impurity to terminate in the state $\mathbf{k}+\mathbf{q}\uparrow$. 35

2.13 a) Cross-relaxation in the presence of fine-structure splitting. b) The spectrum of LaSb:Gd between 4 and 300 K. The low temperature resolved spectrum becomes progressively narrowed. Figure extracted from [79]. 38

2.14 (left) Cross-relaxation in the presence of hyperfine splitting. (right) Spectrum of a powdered sample of 100 p.p.m. Er^{167} in Au at 1.4 K and X-Band. Figure extracted from [79]. 38

3.1 Illustration of the metallic-flux technique. (left) The elements are placed inside an alumina crucible with the flux on the top. The crucible is sealed in a quartz tube under vaccum and then (right) submitted to a thermal treatment. 42

3.2 a) Calorimeter puck and b) thermal connections to sample and sample platform used in the heat capacity measurements. Figures extracted from ref. [81]. 44

3.3 PPMS measurement status viewer displaying the fit plot and the measured temperature versus time. 45

3.4 a) Resistivity sample puck with three samples mounted for four-wire resistance measurements. Figure extracted from ref. [82]. b) Photograph of a $EuIn_2As_2$ single crystal with four platinum leads attached to it by an epoxy resin. 46

3.5 3D modelling view of the pressure cell. Figure extracted from ref. [83]. 47

3.6 (a) Schematic of Landau levels for spherical Fermi surface as in a free electron has in a magnetic field H. (b) Schematic of Landau levels, when the applied magnetic field is increased to $H + \Delta H$. The Landau levels increase in area with an increase in magnetic field, causing fewer of them to be accomodated within the Fermi surface as the magnetic field is increased. Figure extracted from [84]. 48

3.7 Schematics of the MPMS magnetometer. Figure extracted from [85]. 50

3.8 Schematics of the MPMS magnetometer coils. 50

3.9 Schematics of the MPMS SQUID VSM probe. 51

3.10 a) Pictorial view of the photoelectron interference effect. b) XAFS spectrum of a Fe_2O_3 model compound (crystalline powder) at the Fe K-edge ($E_0 = 7112$ eV).The XANES region is more sensitive to the electronic structure and the symmetry, while the EXAFS region gives more information on bond distances, coordination numbers and local disorder. 53

3.11 Beamline specification at the Brazilian Synchrotron Laboratory (LNLS) a) XAFS2 and b) DXAS. 54

3.12 a) The general outlay of an ESR spectrometer. b) Block diagram of a microwave bridge. c) Magnetic and electric field patterns in a standard ESR cavity. d) The matching of a microwave cavity to waveguide. e) Field modulation and phase sensitive detection. Figure extracted from ref. [87]. 56

4.1 (left) Photograph of one of the largest pure single crystals grown by the In-flux technique. (right) EDS image of a Eu-substituted single crystal grown by the In-flux technique. 58

4.2 High resolution synchrotron X-ray diffraction of an IFG $BaFe_2As_2$ single crystal. (a) Radial ($\theta - 2\theta$) scans around the (2212) tetragonal reflection. (b) Temperature dependence of a, b and c lattice parameters. (c) Temperature dependence of unit cell volume. 59

4.3 In-plane resistivity as a function of temperature for $BaFe_2As_2$ single crystals grown by In- and Sn-flux. For comparison, we also show the resistivity of the self-flux [88] and polycrystalline [89] samples. 60

4.4 ^{75}As NMR signal for $BaFe_2As_2$ single crystals grown by In- and Sn-flux in the paramagnetic (tetragonal) phase. 61

4.5 **a)** In-plane electrical resistivity as a function of temperature for $Ba(Fe_{1-x}M_x)_2As_2$ single crystals grown by In flux (M = Co, Cu, Ni and Ru). The chosen samples presented the highest T_c within the obtained batches. The inset shows the maximum T_c achieved for self and In-flux grown crystals for different dopants [109, 106, 107, 108]; **(b)** In-plane electrical resistivity as a function of temperature for $Ba(Fe_{1-x}Co_x)_2As_2$ IFG single crystals (x = 0.03, 0.045 and 0.12). The inset shows field cooled (FC) and zero-field cooled (ZFC) magnetic susceptibility measurements for the optimally doped sample (x = 0.09). 62

4.6 $T - x$ phase diagram for IFG $Ba(Fe_{1-x}Co_x)_2As_2$ single crystals. The error bars represent variations in the doping levels x and T_c amongst different batches of same nominal Co content. 63

4.7 Temperature dependence of the in-plane electrical resistivity of $BaFe_{1.9}TM_{0.1}As_2$ (TM = Mn, Co, Ni, and Cu) single crystals at ambient pressure. 64

4.8 Temperature dependence of the in-plane electrical resistivity $\rho_{ab}(T)$ of $BaFe_{2-x}TM_xAs_2$ (TM = Co and Ni) single crystals at various pressures (∼ 7 –24 kbar) 65

4.9 Temperature dependence of the in-plane electrical resistivity of $BaFe_{1.9}Cu_{0.1}As_2$ single crystals under hydrostatic pressure. 66

4.10 X-Band spectra at T = 150 K for powdered crystals of $BaFe_{1.9}Cu_{0.1}As_2$. 67

4.11 Phase Diagram for $BaFe_{2-x}TM_xAs_2$ (TM = Co, Cu, and Ni) single crystals as a function of pressure: $T_c(P)$ normalized by its zero pressure value $T_c(0)$ *vs.* pressure and T_c *vs.* pressure (P) (inset). 68

4.12 Temperature dependence of the in-plane electrical resistivity of $\mathrm{BaFe}_{2-x}\mathrm{Mn}_x\mathrm{As}_2$ ($x = 0.007, 0.12$) single crystals at ambient pressure and under hydrostatic pressure (0 –25 kbar). 69

4.13 Temperature dependence of the in-plane electrical resistivity of $\mathrm{BaFe}_{1.805}\mathrm{Co}_{0.190}\mathrm{Mn}_{0.005}\mathrm{As}_2$ single crystals at ambient pressure. 70

4.14 Temperature dependence of the in-plane electrical resistivity of $\mathrm{Ba}_{0.8}\mathrm{Eu}_{0.2}\mathrm{Fe}_{1.9}\mathrm{Co}_{0.1}\mathrm{As}_2$ single crystals at ambient pressure and under hydrostatic pressure (0 –26 kbar). . . 71

4.15 Temperature dependence of the in-plane electrical resistivity of $\mathrm{Ba}_{0.99}\mathrm{Eu}_{0.01}\mathrm{Fe}_{1.9}\mathrm{Co}_{0.1}\mathrm{As}_2$ single crystals at ambient pressure and under hydrostatic pressure (0 –26 kbar). . . 71

4.16 Phase diagram T_c vs. P for $\mathrm{Ba}_{0.99}\mathrm{Eu}_{0.01}\mathrm{Fe}_{1.9}\mathrm{Co}_{0.1}\mathrm{As}_2$ and $\mathrm{Ba}_{0.8}\mathrm{Eu}_{0.2}\mathrm{Fe}_{1.9}\mathrm{Co}_{0.1}\mathrm{As}_2$ single crystals. 72

4.17 (left panel) Specific heat per mole versus temperature for $\mathrm{BaFe}_2\mathrm{As}_2$ and $\mathrm{EuFe}_2\mathrm{As}_2$ single crystals. (right panel) Temperature dependence of the in-plane electrical resistivity of $\mathrm{BaFe}_2\mathrm{As}_2$ and $\mathrm{EuFe}_2\mathrm{As}_2$ single crystals. 73

4.18 Raw-data resistivity and 4th order polynomial fit (background) as a function of the magnetic field for $\mathrm{EuFe}_2\mathrm{As}_2$. The inset shows the background subtracted data as a function of inverse magnetic field. 73

4.19 Fourier analysis of the quantum oscillations at two different angles $\theta = 0^\circ$ and $\theta = 25^\circ$ measured with respect to the c-axis. 74

4.20 (a-b) Effective masses for both $\mathrm{EuFe}_2\mathrm{As}_2$ and $\mathrm{BaFe}_2\mathrm{As}_2$ compounds, respectively. (c) Data from the literature [115] for $\mathrm{BaFe}_2\mathrm{As}_2$ 75

5.1 Temperature dependence of the in-plane resistivity of $\mathrm{BaFe}_2\mathrm{As}_2$, $\mathrm{Ba(Fe}_{0.937}Co_{0.063})_2\mathrm{As}_2$, $\mathrm{Ba}_{0.85}\mathrm{K}_{0.15}\mathrm{Fe}_2\mathrm{As}_2$. The arrows indicate the onset of superconductivity at T_c, and asterisks mark the antiferromagnetic transition temperatures. 78

5.2 k^2-weighted As K edge extended x-ray absorption fine structure [$k^2\chi(k)$] spectra of (a) $\mathrm{BaFe}_2\mathrm{As}_2$, (b) $\mathrm{Ba(Fe}_{0.937}Co_{0.063})_2\mathrm{As}_2$, and (c) $\mathrm{Ba}_{0.85}\mathrm{K}_{0.15}\mathrm{Fe}_2\mathrm{As}_2$ at $T = 298$ K. 79

5.3 Magnitude of the Fourier transform of As K edge $k^2\chi(k)$ curves given in Figs. 5.2(a)-5.2(c) for $\mathrm{BaFe}_2\mathrm{As}_2$, $\mathrm{Ba(Fe}_{0.937}Co_{0.063})_2\mathrm{As}_2$, and $\mathrm{Ba}_{0.85}\mathrm{K}_{0.15}\mathrm{Fe}_2\mathrm{As}_2$ at (a) $T = 298$ K and (b) $T = 2$ K. The intervals corresponding approximately to the first [As-(Fe,Co)] and second [As-(Ba,K)] As coordination shells are indicated as dashed areas. 80

5.4 (a) Envelope, real and imaginary components $\chi(R)$ for $\mathrm{BaFe}_2\mathrm{As}_2$ at $T = 298$ K in the first shell interval. (b) Real component of the backward Fourier transform of $\chi(R)$ ($1.6 < R < 2.5$ Å), $\chi(q)$. Circles: experimental data; solid lines: calculated. . 81

5.5 (a) k^2-weighted As K edge extended x-ray absorption fine structure $[k^2\chi(k)]$ spectra of $BaFe_2As_2$ at 298 K with the sample leaded into the diamond anvill cell with $P = 1.2$ GPa (thin line), and $P = 8.6$ GPa (thich line), and $P = 1.6$ GPa after release from $P = 8.6$ GPa (circles). (b) Real component of the Fourier transform of $k^2\chi(k)$ curves given in (a). 83

5.6 Pressure dependence of the As-Fe bond distance at 298 K for $BaFe_2As_2$ obtained from the fits to the As K edge x-ray absorption fine structure (see Fig. 5.5). Circles and triangles represent data taken in different runs. Data were taken for increasing pressures, except for the open circle at 1.6 GPa, which was obtained after releasing the cell from 8.6 GPa. Error bars are statistical only and were estimated from the standard deviation of the results obtained from repeated measurements under identical conditions. The solid line is a linear fit to the data below 6.1 GPa, representing a Fe-As bond compressibility of $\kappa = 3.3(3) \times 10^{-3}$ GPa^{-1}. 84

5.7 In-plane electrical resistivity of $BaFe_{2-x}Co_xAs_2$ as a function of temperature. The solid lines are guide to the eyes. 85

5.8 a) Observed and calculated Fe K edge XANES spectrum of pure $BaFe_2As_2$; calculated spectrum for the model compound $Ba_{0.75}La_{0.25}Fe_2As_2$ to simulate the effects of true electron doping. Prominent peaks and shoulders are indicated in $A - F$. The calculated spectra are shifted vertically for better visualization. (b) Energy first derivative of the spectra shown in (a). Derivative maxima and minima are represented as $A' - F'$ and $A'' - F''$, respectively. The reference Fe metal XANES spectrum is also shown for comparison. 86

5.9 (a) Normalized Fe K edge XANES spectra of $BaFe_{2-x}Co_xAs_2$ at room T. Prominent peaks and shoulders are indicated $A-F$. (b) First derivative of the XANES spectra in (a). Derivative maxima and minima are represented as $A' - F'$ and $A'' - F''$, respectively. 87

5.10 Fe K edge XANES spectra first derivative A', B', C', D' and E' feature (see Fig. 5.9) positions as a function of Co substitution in $BaFe_{2-x}Co_xAs_2$. The solid spline lines are the expected redshifts by true electron doping, obtained by simulated XANES spectra $Ba_{1-x}La_xFe_2As_2$ ($x = 0.00, 0.25$, and 0.50) model compounds. The dashed lines are the expected shifts obtained by a linear extrapolation using calculated XANES spectrum of $BaFe_{1.5}Co_{0.5}As_2$. 88

5.11 Specific heat per mole versus temperature of the $Ba_{1-x}Eu_xFe_2As_2$ series. The inset shows low-T data for $x = 0.55$ 90

5.12 Magnetic susceptibility as a function of temperature of the $Ba_{1-x}Eu_xFe_2As_2$ series. The insets show the high-T data and T_{SDW} for $x = 0.01$, respectively. 91

5.13 Normalized electrical resistivity versus temperature of the $Ba_{1-x}Eu_xFe_2As_2$ series. The inset shows the low-T data upturn for $x = 0.10$. 91

5.14 X-Band spectra at T= 300 K for $H||ab$ for the $Ba_{1-x}Eu_xFe_2As_2$ series. 92

5.15 T- dependence of the a) linewidth ΔH and b) g-value. The data for x= 0.01 (In) and x= 0.01 (FeAs) were taken in powderized crystals and several small crystals, respectively. 93

5.16 $Ba_{1-x}Eu_xFe_2As_2$ phase diagram displaying the Eu^{2+} AFM transition temperature (red circles), the Fe^{2+} SDW transition temperature (black circles), and the Korringa rate b (blue open circles). 94

5.17 ARPES dispersion for (a) $BaFe_2As_2$ and (b) $EuFe_2As_2$ at 300 K and (c-d) at 30 K. Figure extracted from [129]. 96

5.18 Physical properties of $Ba_{1-x}Eu_xFe_{2-y}TM_yAs_2$ single crystals (TM for transition metals Co, Cu, Mn, Ni, and Ru). The inset shows a) the resistivity going to zero at the superconducting transition, b) zero-field cooling/field cooling magnetic susceptibility. 99

5.19 X-Band ESR lines at T= 300 K for selected $Ba_{1-x}Eu_xFe_{2-y}TM_yAs_2$ single crystals. 100

5.20 T- dependence of the a) linewidth ΔH and the b) g-value taken in powderized crystals 101

5.21 Dependence of T_{SDW} and b as a function of the (a) out-of-plane and (b) in-plane substitution in $BaFe_2As_2$ 103

5.22 Linear fit of T_c as a function of pressure for Mn- and Cu-substituted compounds. . 105

5.23 Temperature dependence of macroscopic physical properties of $EuIn_2As_2$ single crystals. a) Magnetic susceptibility with applied field H= 1kOe parallel to the *hex*-plane and to the *c*-axis. b) Electrical in-plane resistivity. c) Specific heat per mole divided by temperature. 107

5.24 X and Q-Band Eu^{2+} ESR spectra at T= 100K for H parallel to the hex-plane and to the c-axis of $EuIn_2As_2$ single crystals. 108

5.25 Temperature dependence of Eu^{2+} ESR ΔH and g-factor in Q- and X-Bands. . . . 109

5.26 (upper panel) Q- and X-Bands Eu^{2+} ESR ΔH anisotropy at T = 100 K. (lower panel) Resistivity anisotropy for several applied magnetic fields at T = 100 K. . . 110

List of Tables

List of abbreviations **xvii**

List of Figures **xix**

List of Tables **xxvii**

2.1 The value of the effective moment p determined by the coefficient of $1/T$ (eq. 2.8) in the measured susceptibility compared with that given by $p_{eff} = g(JLS)[J(J+1)]^{1/2}$. 13

2.2 Calculated and measured effective magneton numbers p for the iron $3d$ group ions. 13

4.1 Parameters for the heat treatment, illustrated in Fig. 3.1, used in the growth of $BaFe_2As_2$ with different substituting atoms. The asterisk represents the compound $EuIn_2As_2$. 64

4.2 Samples studied by Shubunikov-de Haas oscillations and their residual resistivity ρ_0, residual resistivity ratio (RRR), and magnetoresistance. 72

5.1 Refined As-M (M = Fe, Co) distances and Debye-Waller factor obtained from the fits of x-ray absorption fine structure data at the As K edge at ambient pressure. Errors given in parentheses are statistical only, and are defined as the standard deviation of the results obtained from repeated measurements under identical conditions. 82

5.2 Experimental ESR exchange interaction ($< J^2_{fs}(\mathbf{q}) >^{1/2}$) for the compounds in the $Ba_{1-x}Eu_xFe_{2-y}TM_yAs_2$ series. 102

5.3 Experimental and calculated parameters for compounds of the $Ba_{1-x}Eu_xFe_{2-y}TM_yAs_2$ series. 104

Chapter 1

Introduction

In this thesis, we have experimentally studied the macroscopic and microscopic properties of the tetragonal compound $BaFe_2As_2$ as a function of three parameters: Eu substitution in the Ba crystallographic site, transition metal (TM) substitution (TM = Mn, Co, Ni, Cu, and Ru) in the Fe site, and/or applied hydrostatic pressure. The main motivation of this work consists in the existence of an interplay between magnetism and high-temperature superconductivity in a class of intermetallic systems that have a common local structure: FeAs superconducting sheets arranged in $FeAs_4$ tetrahedra, Fig. 1.1.

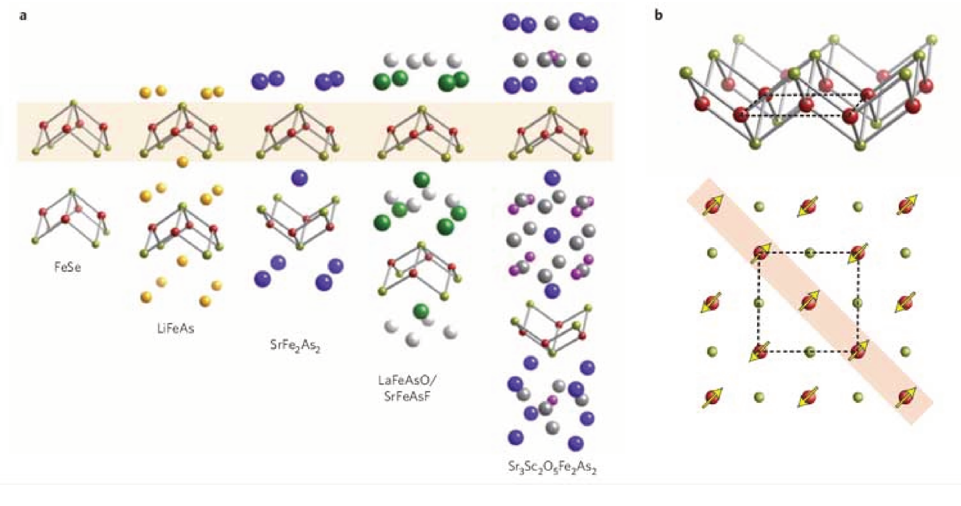

Figure 1.1: Five different structural classes of iron-based superconductors that share a common layered structure based on a planar layer of iron atoms joined by tetrahedrally coordinated pnictogen (P, As) or chalcogen (S, Se, Te) anions arranged in a stacked sequence separated by alkali, alkaline-earth or rare-earth and oxygen/fluorine blocking layers. Figure extracted from ref. [1]

Therefore, the initial objective of the present study is to systematically establish the magnetic and/or superconducting properties of $BaFe_2As_2$ with appropriate substitution and/or applied pressure. More specifically, we will employ local techniques, such as electron spin resonance (ESR) and X-ray absorption spectroscopy (XANES and EXAFS), to obtain information about the relationship between local structural distortions and the system spin dynamics.

In this Introdution, we will first present a general overview of the Fe-based superconductors and their connection with other unconventional superconductors. Thereon, we will approach the specific concern of this thesis. In Chapter 2, the theoretical background will be presented: magnetism in solids, superconductivity, crystal field effects and electron spin resonance. Chapter 3 presents an overview of the experimental techniques employed during this work. Chapters 4 and 5 present the results and discussions of the macroscopic and microscopic measurements, respectively. Finally, Chapter 5 contains the conclusions of this work. The papers published during this thesis are listed in Appendix 1.

1.1 Fe-based Superconductors: State of the Art

The report of superconductivity at a critical temperature T_c = 26 K in fluorine-substituted LaFeAsO have triggered intense scientific investigation since their discovery in 2008 [2]. When appropriately substituted, compounds in the RFeAsO (R =La−Gd) family become superconducting and can reach critical temperatures as high as 56 K in $Gd_{0.8}Th_{0.2}FeAsO$. The subsequent efforts to synthesize new materials with FeAs layers ultimately brought back to the scene the 122 family with the discovery of an oxygen-free new family of superconductors (SC) AFe_2As_2 (A = Ba, Sr,Ca, Eu) with a highest T_c of 38 K in the potassium-substituted $BaFe_2As_2$ [113]. Interesting, despite the fact that one class is an oxide family and the other is an intermetallic system, superconductivity can be found in both systems with comparable critical temperatures when the magnetic spin-density wave (SDW) phase ($100\,\mathrm{K} \lesssim \mathrm{T}_{SDW} \lesssim 200\,\mathrm{K}$) is suppressed by chemical substitution and/or applied pressure [4]. Moreover, both systems have an unconventional nature of the Cooper pairing state, meaning that the superconducting pair state is not an isotropic nodeless s-wave state, and the pairing interaction is other than the conventional electron-phonon interaction. Strikingly, several classes of unconventional superconductors (heavy fermion, cuprates, organic and iron-based SCs) have a low-symmetry layered structure and display an unsettling similar phase diagram, shown in Figures 1.2 and 1.3, with an antiferromagnetic parent compound, indicating that the pairing is magnetic-mediated. In fact, structural parameters in low-symmetry layered systems have played an important role in determining the symmetry and the dimensionality of the magnetic fluctuations. However, there is no consensus on the microscopic reason why these crystal structures seem to be favorable to the emergence of such phenomena.

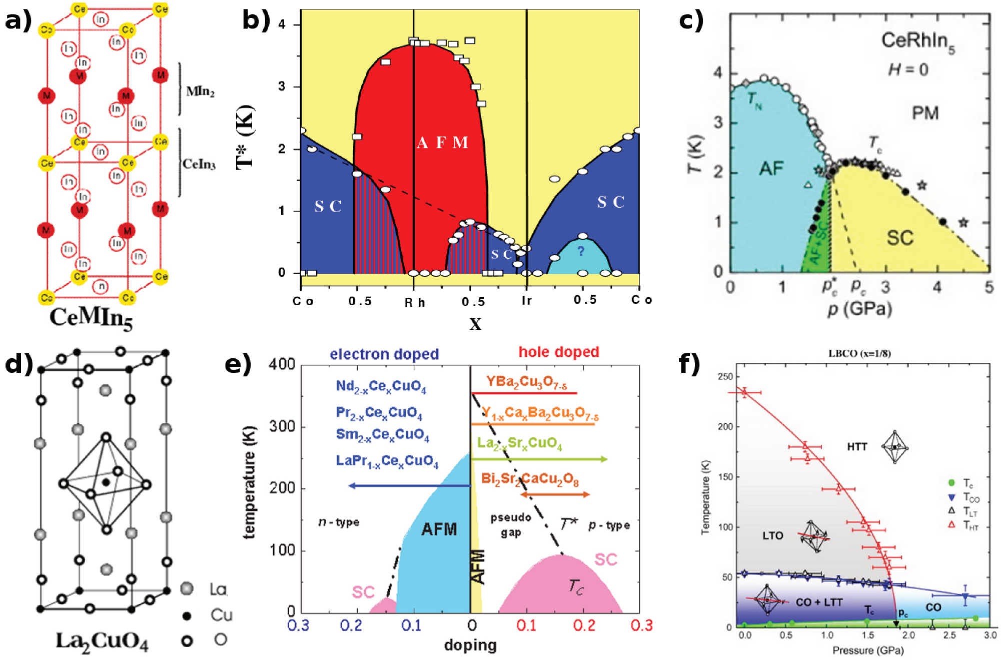

Figure 1.2: (a,d) Crystal structure and phase diagrams as a function of (b,e) substitution and (c,f) applied pressure for heavy fermion and cuprate compounds. Figures extracted from ref. [5, 6, 7, 8]

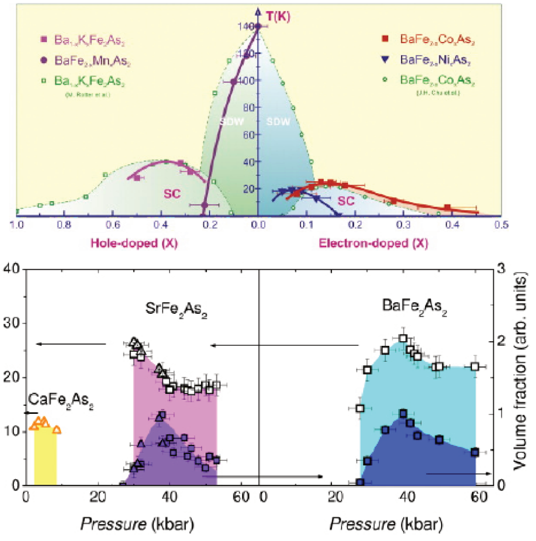

Figure 1.3: Phase diagram for the 122 system as a function of substitution (top) and of applied pressure (bottom). Figure extracted from ref. [9].

In particular, the $A\mathrm{Fe_2As_2}$ family crystallizes in the tetragonal $\mathrm{ThCr_2Si_2}$-type structure ($I4/mmm$) and exhibits a structural distortion closely related to the SDW phase transition. It is remarkable that this SDW phase can be tuned towards a SC state by both substitution (isovalent or "electron/hole") and applied pressure, suggesting that structural tuning plays a role, as in the heavy-fermion systems. Moreover, theoretical calculations using a supercell approach to density funcional theory (DFT) have shown that the substitutions mentioned above act as chemical pressure instead of effective doping [10]. The extra d electrons or holes from the impurity were actually concentrated at the substitute Co site. From the experimental point of view, Mössbauer spectroscopy measures the same s-electron density at the ^{57}Fe nuclei for both pure and substituted $\mathrm{BaFe_2As_2}$ [11, 12]. In addition, resonant photoemission spectroscopy reveals that the Co $3d$ state center of mass is observed at 250 meV higher binding energy than that of Fe, indicating that Co possesses one extra valence electron and that Fe and Co are in the same oxidation state. However, the Co $3d$ electrons are part of the Fermi sea determining the Fermi surface and this complex behavior reveals an inadequacy of a rigid-band shift description frequently used in angular resolved photoemission spectroscopy (ARPES) analysis to argue that there is charge doping in the Fermi surface [13]. Very recently, finally this apparent contradition with ARPES measurements were solved: Ni and Cu substituons in $\mathrm{BaFe_2As_2}$ were compared to the Co one. It was found that the Ni $3d$-derived features are formed below the Fe $3d$ band and that Cu $3d$-derived ones further below it. Moreover, the electron Fermi surface volumes in Ni- and Cu-122 are smaller than the value expected from the rigid-band model, suggesting that part of electrons doped by substitution of Ni or Cu preferentially occupy the Ni $3d$ or Cu $3d$ states, or are trapped around the impurity sites, and do not behave like a mobile carrier [14].

Concerning the structural tuning, crystalline electric field (CEF) effects are often important for the ground state determination in strongly correlated materials. Particularly, heavy fermion superconductors have f-electrons that strongly hybridize with the conduction bands and the single-ion anisotropy defined by the CEF effects can influence the spin fluctuations near the conduction bands. It has been shown that the superconducting transition temperature (T_c) trendly scales with the lattice parameters ratio c/a, Fig. 1.4a [5, 15, 16, 17, 18]. For the cuprates, structural parameters have been suggested for controling T_c: the bond length between copper and in-plane oxygen and the Cu-apical oxygen distance. It was proposed that the apical oxygen distance from the $\mathrm{CuO_2}$ plane also naively scales with T_c, Fig. 1.4b, and that the less the $d_{x^2-y^2}$ main band is hybridized with the d_{z^2} and $4s$ orbitals the higher the T_c [19, 20, 21].

Recently, several works in the iron-based SCs have shown a close relationship between the magnetic SDW phase and the structural parameters, such as the Fe-pnictogen/chalcogen distance and the tetrahedra shape, Fig. 1.5, that are believed to control the CEF levels and consequently

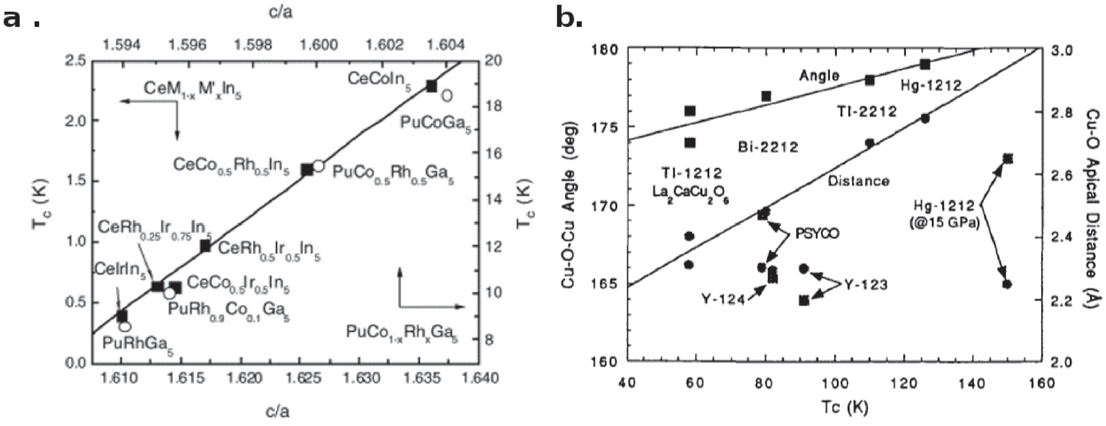

Figure 1.4: a. Superconducting transition temperatures as a function of tetragonal lattice parameters c/a for various Ce- and Pu-members of the CeMIn$_5$ and PuMGa$_5$ families. Figure from ref. [22]. b. Relationship between T_c and the Cu-O-Cu buckling angle for the CuO$_2$ planes and the Cu-O apical bond distance for compounds with two CuO$_2$ layers. Square symbols are angles; round symbols are distances. Figure from ref. [21]

the orbital weight in the Fermi surface bands [23].

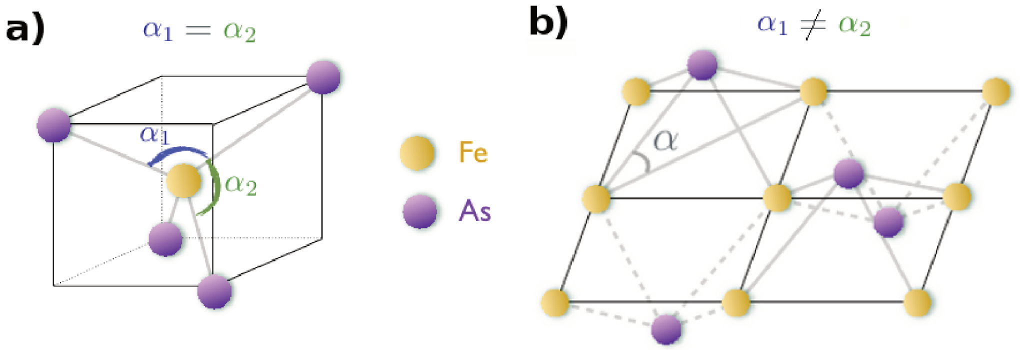

Figure 1.5: a) Tetrahedral symmetry in a cubic environment. b) Distorted tetrahedra in the real lattice. The Fe-As distance and the angle α changes among compounds with substitution and pressure.

The iron pnictide and chalcogenide superconductors have five Fe $3d$ bands at the Fermi surface with a Fermiology consisting typically of five separated pockets with varying degrees of interpocket nesting, Fig. 1.6. ARPES measurements of Fe-pnictides and chalcogenides have shown that this fermiology can change rapidly with a variety of substitutions [24]. In this manner, the CEF splitting of the $3d$ bands is important to determine which orbital character participates in the Fermi surface and this is crucial for the SDW phase formation and also for the emergence of superconductivity when the SDW phase is suppressed.

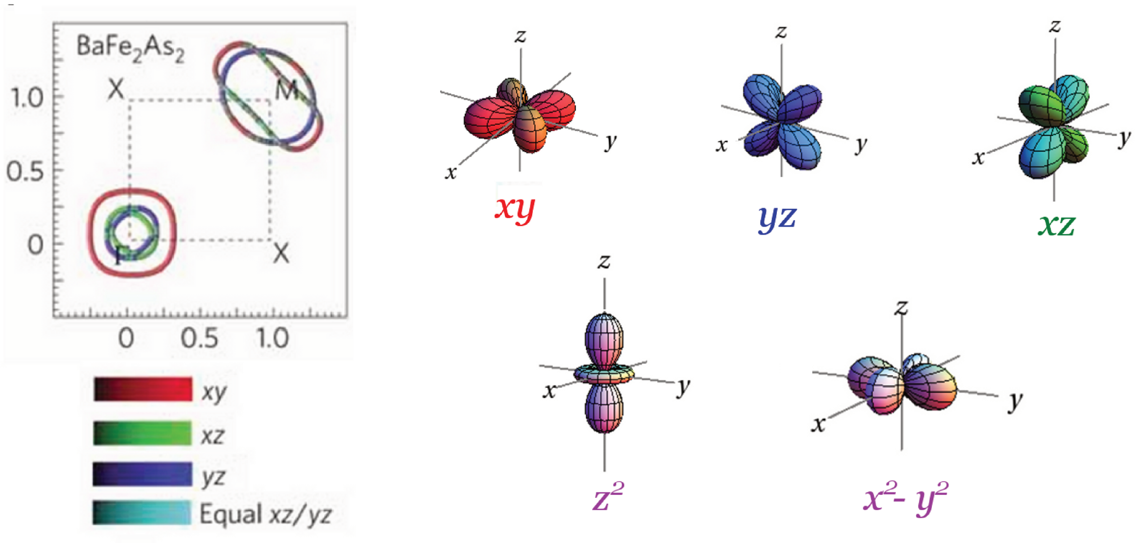

Figure 1.6: (left) Fermi surface calculated by DFT+DMFT [23] and (right) Fe $3d$ orbitals.

In many FeAs-based SCs, a SDW order is found to have a wave vector directed along (π, π) direction in the tetragonal unit cell with a real-space spin arrangement consisting of AFM stripes along one direction of the Fe sublattice and ferromagnetic stripes along the other, with an ordered moment typically smaller than one Bohr magneton [25]. There is an intense debate whether this magnetic phase has itinerant or localized degrees of freedom. Inelastic neutron scattering have shown itinerant spin excitations and a spin-fluctuation resonance in the 1111, 122, 111, and 11 structure superconductors below T_c, similar to the cuprates [26, 72]. In any case, it seems that a dual description is needed to properly describe the magnetic phase.

In addition, although there is a general consensus that magnetic interactions are important for superconductivity, much remains unknown concerning the microscopic origin of the magnetic states and the coexistence between SC and magnetism. Mössbauer spectroscopy reveals a clear magnetic hyperfine field A_{hf} below T_c for several substitution in BaFe$_2$As$_2$, indicating coexistence between magnetism and SC since it is reasonable that there is no phase separation on a length scale smaller then the SC coherence length, $\xi \sim 2$ nm [12]. Moreover, nuclear magnetic resonance (NMR) measurements clearly shows a microscopic coexistence between magnetism and SC [97].

As one can notice there are still several central questions remaining, including the role of magnetism, the nature of chemical and structural tuning, and the resulting pairing symmetry. A sensitivity of electronic structure and/or magnetic interactions to details of the internal structure of the Fe-As layers is relevant to unraveling this puzzle and to find universal properties and principles. This thesis intends to provide a microscopic understanding of the interplay between SDW and SC by using microscopic probes that can directly study the spin dynamics and the structural parameters.

1.2 Specific problem: What is the important tuning parameter in $\mathbf{BaFe_2As_2}$?

In addition to the Fe moment ($\sim \mu_B$) in the AFe$_2$As$_2$ members (A = Ba, Ca, Sr), the $EuFe_2As_2$ compounds have also Eu^{2+} ions with large local magnetic moments (7.94 μ_B) that order antiferromagnetically at $T_N = 19$ K (Fig. 1.7b). Mössbauer experiments have measured the oxidation state of europium ions (Eu^{2+}) and evidenced a small, but significant, coupling between the localized Eu^{2+} moments and the conduction electrons from the FeAs layers [27]. Upon substitution by K, Co, and P, $EuFe_2As_2$ also undergoes superconducting transitions but with slightly lower T_c compared to $BaFe_2As_2$ [28, 29, 30, 31]. Interesting, for both Co-substituted case and pressure, there is a reentrant behavior of the resistivity due to the Eu^{2+} antiferromagnetic ordering [32]. For the first case, an applied magnetic field is capable of polarizing the Eu^{2+} spins, leading to the coexistence between superconductivity and ferromagnetism.

Electron spin resonance (ESR) is a powerful microscopic spin probe that has been used to study the site specific spin dynamics in these compounds. By measuring locally the electronic susceptibility, $\chi^{''}$ ($\mathbf{q}$, ω), the electronic, structural and chemical properties of a material can be probed using a paramagnetic ion, such as Eu^{2+} or Mn^{2+} ions.

However, up to date, the ESR experiments have been focused on Eu-based samples far from diluted regime. For instance, Eu^{2+} ESR data in $EuFe_2As_2$ single crystals indicate a spatial confinement of the conduction electrons (*ce*) to the FeAs layers below T_{SDW} as evidenced by the change in the ESR linewidth from a typical metallic behavior (i.e., a linear Korringa-type increase [1] above T_{SDW} to a magnetic insulating behavior, where dipolar and crystalline electrical field effects dominate [42]. In hole doped $Eu_{0.5}K_{0.5}Fe_2As_2$, where the SDW phase is completely suppressed and SC arises for $T \leq 32$ K, a Korringa behavior also occurs for $T > T_c$ [43]. For the electron doped $EuFe_{2-x}Co_xAs_2$, the Korringa rate, T_{SDW} and T_c scale with x [44]. A recent report on polycrys-

---

[1] The Korringa parameter b represents the thermal broadening rate of the ESR line which is proportional to the relaxation rate ($1/T_1$, where T_1 is the spin-lattice relaxation time) of the Eu^{2+} resonating spins via conduction electrons and ultimately to the lattice. A detailed discussion is presented in Section 2.4)

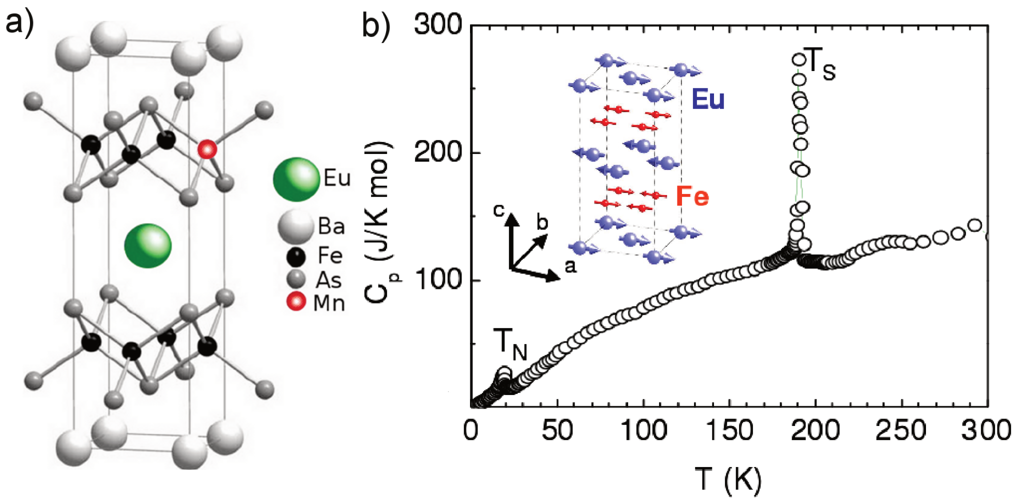

Figure 1.7: a) Substitution of Eu^{2+} and Mn^{2+} in the Ba^{2+} and Fe^{2+} crystallographic sites, respectively. b) Specific heat versus temperature of the EuFe$_2$As$_2$ compound displaying antiferromagnetic ordering of the Fe ions at $T_{SDW} = 190$ K and of the Eu ions at $T_N = 19$ K. The inset shows both magnetic structures. Figure extracted from ref. [33].

talline EuFe$_{2-x}$Co$_x$As$_2$ also shows a Korringa rate decreasing with Co-doping [45]. Interestingly, a slower Korringa rate b is obtained for all substitutions and it has been attributed to a change in the density of states at the Fermi level, $\eta(E_F)$. However, in the Eu-concentrated compounds, the Eu^{2+}-Eu^{2+} spin interaction always represents an important contribution to the ESR data and to the global properties of the compounds. Therefore, it is crucial to extrapolate such studies to a Eu^{2+} diluted regime in a host compound of great interest. BaFe$_2$As$_2$ is an obvious choice since it offers the possibility of growing high quality single crystals that can be tuned toward SC by pressure and substitution. In this manner, we aim to grow BaFe$_2$As$_2$ high-quality single crystals with substitutions of paramagnetic probes in both Ba and FeAs planes in order to gain microscopic insight about the important tuning parameters that lead to superconductivity, Fig. 1.7a.

Chapter 2

Theoretical Aspects

In this chapter, the underlying theory used throughout this thesis will be discussed: magnetism in solids, superconductivity and crystal field effects. Furthermore, we will approach resonance phenomena in order to understand how electron spin resonance can provide information about the physical systems of interest.

2.1 Magnetism in Solids

Let us first consider an atom with Z electrons in the presence of a weak uniform external static magnetic field ($\mathbf{H} = \nabla \times \mathbf{A}$). We can write the perturbed Hamiltonian as:

$$\mathcal{H} = \mathcal{H}_0 + \mu_B(\mathbf{L} + g\mathbf{S}) \cdot \mathbf{H} + \frac{e^2}{8m_e c^2} \sum_{i=1}^{Z} (\mathbf{H} \times \mathbf{r}_i)^2, \tag{2.1}$$

where $\mathcal{H}_0 = \sum_{i=1}^{Z} (\frac{p_i^2}{2m} + V_i)$ is the unperturbed Hamiltonian; $\mu_B = e\hbar/2m_e$ is the Bohr magneton; $\mathbf{L}$ and $\mathbf{S}$ are the total orbital angular momentum and total spin operator, respectively; $\mathbf{r_i}$ and $\mathbf{p_i}$ are the position and the momentum operators of the ith electron in the atom.

The energy shifts produced by eq. 2.1 are generally small on the scale of atomic excitation energies. Therefore, one can compute the changes in the energy levels induced by the field with ordinary perturbation theory.

In general, we define the magnetic susceptibility χ of a linear material composed of N ions in the presence of $\mathbf{H}$ as:

$$\chi = \frac{\partial M}{\partial H} = -\frac{N}{V} \frac{\partial^2 E_0}{\partial H^2}, \tag{2.2}$$

where M is the material magnetization (magnetic moment per volume). In the last equality we used the fact that there is negligible probability of the ion being in any but its ground state in thermal equilibrium.

In order to compute the second derivative in equation 2.2 one must retain terms up to the second order in H. Second-order perturbation theory then gives:

$$\Delta E_n = \mu_B \mathbf{H} \cdot \langle n|\mathbf{L}+g\mathbf{S}|n\rangle + \sum_{n'\neq n} \frac{|\langle n|\mu_B \mathbf{H}\cdot(\mathbf{L}+g\mathbf{S})|n'\rangle|^2}{E_n - E_{n'}} + \frac{e^2}{8mc^2} H^2 \langle n| \sum_i (x_i^2 + y_i^2)|n\rangle. \quad (2.3)$$

This equation is the basis for magnetic susceptibility theories of individual atoms, ions, or molecules.

In this manner, for the third term in equation 2.1 we have a weak, negative contribution of the order of 10^{-5} to the magnetic susceptibility:

$$\chi_d = -\frac{e^2 Z\langle r^2\rangle}{6m_e c^2}\frac{N}{V}, \quad (2.4)$$

known as the Larmor diamagnetic susceptibility[1]. We define $\langle r^2\rangle$ as the mean square ionic radius.

The term diamagnetism is applied to cases of negative susceptibility (i.e., cases in which the induced moment is opposite to the applied field) and all materials present it in some degree. In a simplified view, an external magnetic field alters the orbital velocity of the electrons around the nuclei, thus changing the magnetic dipole moment. According to Lenz's law, this opposes the external field. Consequently, diamagnetism is a form of magnetism that is only exhibited by a substance in the presence of an externally applied magnetic field. It is generally quite a weak effect in most materials, although superconductors exhibit a strong effect that we will discuss in section 2.2

2.1.1 Paramagnetism

Now we turn our attention to the second term in equation 2.1, known as Zeeman term, that plays a role in ions with partially filled shells. There are two distinguisable cases: if the shell has $J = L + S = 0$ and if it has $J = L + S \neq 0$.

Van Vleck Paramagnetism

If the shell[2] has $J = 0$, the first-order energy shift from perturbation theory $\langle 0|(\mathbf{L}+g\mathbf{S})|0\rangle$ is zero. Thus, the magnetic susceptibility can be written as:

---

[1] It is also referred to as the core diamagnetic susceptibility or Langevin susceptibility

[2] As is the case of d^4 and f^6, i.e., shells that are one electron short of being half filled

$$\chi_v = -\frac{N}{V}\left[\frac{e^2}{4mc^2}\langle 0|\sum_i (x_i^2 + y_i^2)|0\rangle - 2\mu_B^2 \sum_n \frac{|\langle 0|(\mathbf{L} + g\mathbf{S})|n\rangle|^2}{E_n - E_0}\right]. \tag{2.5}$$

The first term was already discussed and corresponds to the Larmor diamagnetic contribution. On the other hand, the total contribution from the second term is positive, and therefore favors aligment of the moment parallel to the field. This behavior is known as paramagnetism and this higher order correction independent of temperature is known as Van Vleck paramagnetism.

Curie Paramagnetism

If the shell has $J \neq 0$, we have a non-zero first-order term in the energy shift that is much larger than the other two terms. In this case, the ground state is $(2J+1)$-fold degenerate in zero field and we must diagonalize the $(2J+1)$-dimensional square matrix $\langle JLSJ_z|(\mathbf{L} + g\mathbf{S})|JLSJ_z'\rangle$. This can be done by using the Wigner-Eckart theorem, which states that the matrix elements of any vector in the $(2J+1)$-dimensional space of eigenstates of $\mathbf{J}^2$ and $\mathbf{J}_z$ with a given value of $\mathbf{J}$ are proportional to the matrix elements of $\mathbf{J}$ itself:

$$\langle JLSJ_z|(\mathbf{L} + g\mathbf{S})|JLSJ_z'\rangle = g(JLS)\langle JLSJ_z|\mathbf{J}|JLSJ_z'\rangle. \tag{2.6}$$

As the coefficient $g(JLS)$ does not depend on J_z, the matrix is already diagonal in the states of definite J_z and the $(2J+1)$-fold degenerate ground state is therefore split into states with definite values of J_z whose energies are uniformly separated bt $g(JLS)\mu_B H$. We notice that the ground $(2J+1)$ degenerate states in zero field are diagonal in J, L, and S and one can write $(\mathbf{L} + g\mathbf{S}) = g(JLS)\mathbf{J}$. Moreover, if the splitting between the zero-field atomic ground-state multiplet and the first excited multiplet is large compared with $k_B T$, then only the $(2J+1)$ states in the ground-state contribute appreciably to the free energy. In this case, we can interpret the first term in the energy shift of equation 2.3 as expressing the energy $E = -\vec{\mu}\cdot\vec{H}$ of the interaction of the field with a magnetic moment that is proportional to the total angular momentum of the ion:

$$\mu = -g(JLS)\mu_B \mathbf{J}. \tag{2.7}$$

Due to the fact that the zero-field ground state is degenerate, we can not calculate the susceptibility by equating the free energy to the ground-state energy as we did in the last section for the nondegenerate shells with $J = 0$. Considering that only the lowest $2J+1$ states are thermally excited with appreciable probability, we can calculate the free energy in the canonical ensemble[3] and we obtain a variation of the susceptibility inversely with temperature, known as Curie's law:

$$\chi_c = \frac{1}{3}\frac{N}{V}\frac{\mu_B^2 p_{eff}^2}{k_B T} = \frac{C}{T}, \tag{2.8}$$

where C is the Curie constant, $p_{eff} = g(JLS)[J(J+1)]^{1/2}$ is the effective Bohr magneton number[4] and g_J is the Landé g-factor given by:

$$g(JLS) = \frac{3}{2} + \frac{1}{2}\left[\frac{S(S+1) - L(L+1)}{J(J+1)}\right]. \tag{2.9}$$

It is worth noting that room temperature paramagnetic susceptibilities should be of the order 10^{-2} to 10^{-3} and its contribution completely dominates the diamagnetic one. However, we have to keep in mind that the Curie's law has conditions for its validity: $k_B T \gg h\mu_B H$; the magnetic interaction between ions can not be appreciable; the J-multiplet lying above the ground state can not be close in energy (so that second order terms can be neglected and only the lowest $2J+1$ states are thermally excited with appreciable probability). Moreover, the magnetism of rare-earth ions in an insulating solid is well described by treating them as isolated ions, as shown in Table 2.1.

However, this is not the case for transition metal ions. For ions from the iron group one finds that although Curie's law is obeyed, the value of p_{eff} is determined from equation 2.8 only if one assumes that, although S is still given by Hund's rules, L is zero and hence J is equal to S, as shown in Table 2.2. This phenomenon is known as the *quenching* of the orbital angular momentum and it is a particular example of crystal field effect, which we are going to discuss below in section 2.3.

The earliest attempt of a quantitative analysis of the ferromagnetic transition was put forward by P. Weiss and is known as mean (or molecular) field theory. Although there are sophisticated calculations nowadays, the mean field approximation is usually a good starting point to obtain the leading correction to Curie's law. If we focus our attention on a particular site $\mathbf{R}$ and replace each other spin by its mean value, we arrive at the Weiss' effective external field:

$$\mathbf{H}_{eff} = \mathbf{H} + \lambda\mathbf{M}, \qquad \lambda = \frac{V}{N}\frac{J_0}{(g\mu_B)^2} \quad \text{and} \quad J_0 = \sum_{\mathbf{R}} J(\mathbf{R}). \tag{2.10}$$

For high temperatures, we can then calculate the susceptibility using equations 2.2 and 2.8:

---

[3] The statistical mechanical calculation is discussed in detail, for example, in ref. [46]

[4] It is useful to replace the constant values in order to write the effective magnetic moment as $p_{eff} = \sqrt{8C}$

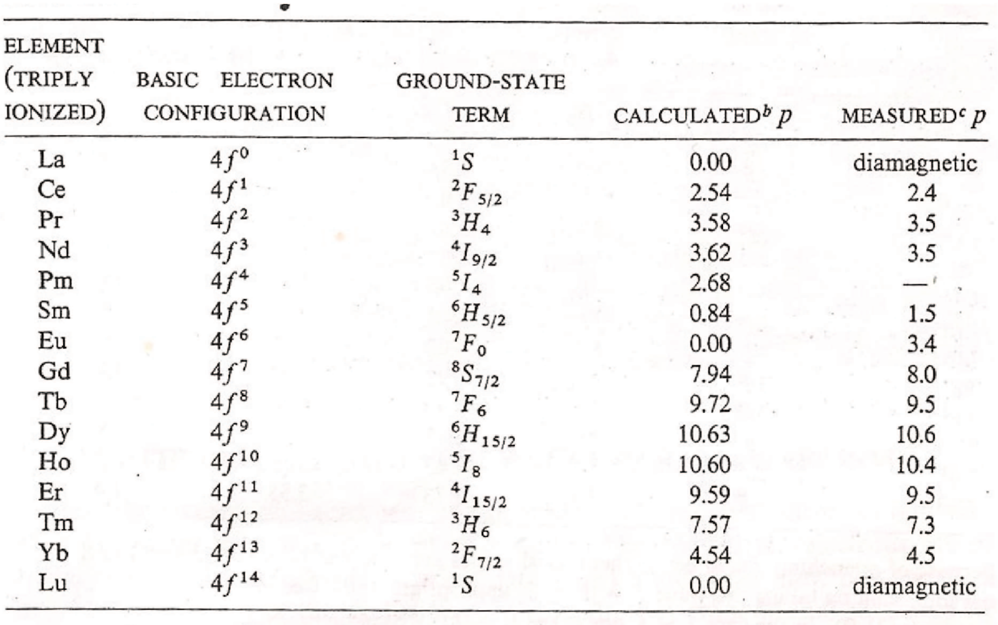

ELEMENT (TRIPLY IONIZED)	BASIC ELECTRON CONFIGURATION	GROUND-STATE TERM	CALCULATED[b] p	MEASURED[c] p
La	$4f^0$	^1S	0.00	diamagnetic
Ce	$4f^1$	$^2F_{5/2}$	2.54	2.4
Pr	$4f^2$	$^3H_4$	3.58	3.5
Nd	$4f^3$	$^4I_{9/2}$	3.62	3.5
Pm	$4f^4$	$^5I_4$	2.68	—
Sm	$4f^5$	$^6H_{5/2}$	0.84	1.5
Eu	$4f^6$	$^7F_0$	0.00	3.4
Gd	$4f^7$	$^8S_{7/2}$	7.94	8.0
Tb	$4f^8$	$^7F_6$	9.72	9.5
Dy	$4f^9$	$^6H_{15/2}$	10.63	10.6
Ho	$4f^{10}$	$^5I_8$	10.60	10.4
Er	$4f^{11}$	$^4I_{15/2}$	9.59	9.5
Tm	$4f^{12}$	$^3H_6$	7.57	7.3
Yb	$4f^{13}$	$^2F_{7/2}$	4.54	4.5
Lu	$4f^{14}$	^1S	0.00	diamagnetic

Table 2.1: The value of the effective moment p determined by the coefficient of $1/T$ (eq. 2.8) in the measured susceptibility compared with that given by $p_{eff} = g(JLS)[J(J+1)]^{1/2}$.

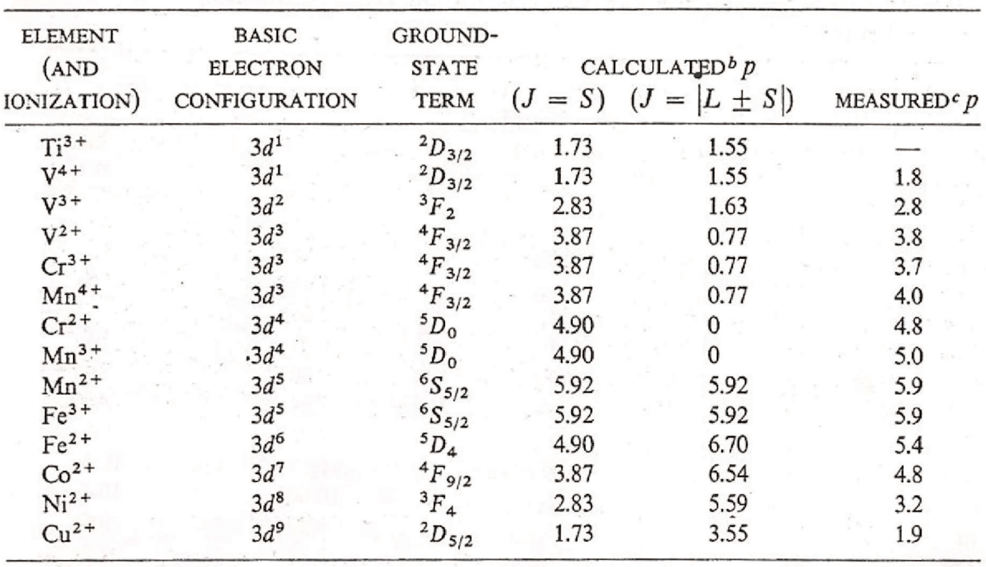

ELEMENT (AND IONIZATION)	BASIC ELECTRON CONFIGURATION	GROUND-STATE TERM	CALCULATED[b] p $(J = S)$	$(J = \lvert L \pm S \rvert)$	MEASURED[c] p
Ti^{3+}	$3d^1$	$^2D_{3/2}$	1.73	1.55	—
V^{4+}	$3d^1$	$^2D_{3/2}$	1.73	1.55	1.8
V^{3+}	$3d^2$	$^3F_2$	2.83	1.63	2.8
V^{2+}	$3d^3$	$^4F_{3/2}$	3.87	0.77	3.8
Cr^{3+}	$3d^3$	$^4F_{3/2}$	3.87	0.77	3.7
Mn^{4+}	$3d^3$	$^4F_{3/2}$	3.87	0.77	4.0
Cr^{2+}	$3d^4$	$^5D_0$	4.90	0	4.8
Mn^{3+}	$3d^4$	$^5D_0$	4.90	0	5.0
Mn^{2+}	$3d^5$	$^6S_{5/2}$	5.92	5.92	5.9
Fe^{3+}	$3d^5$	$^6S_{5/2}$	5.92	5.92	5.9
Fe^{2+}	$3d^6$	$^5D_4$	4.90	6.70	5.4
Co^{2+}	$3d^7$	$^4F_{9/2}$	3.87	6.54	4.8
Ni^{2+}	$3d^8$	$^3F_4$	2.83	5.59	3.2
Cu^{2+}	$3d^9$	$^2D_{5/2}$	1.73	3.55	1.9

Table 2.2: Calculated and measured effective magneton numbers p for the iron $3d$ group ions.

$$\chi = \frac{\partial M}{\partial H} = \frac{\partial M_0}{\partial H_{eff}} \frac{\partial H_e f f}{\partial H} = \chi_C (1 + \lambda \chi). \tag{2.11}$$

Rearranging the terms, we obtain a modified Curie's law known as Curie-Weiss' law:

$$\chi = \frac{\chi_c}{1 - (\theta_{CW}/T)} = \frac{C}{T - \theta_{CW}}, \tag{2.12}$$

where $\theta_{CW} = \lambda C = 2zJC$ (with z the coordination number) gives an important estimate of the exchange interaction J. Thus, the sign of θ_{CW} determines if the interaction is ferromagnetic ($\theta > 0$) or antiferromagnetic ($\theta < 0$) and it can be determined experimentally by a linear fit to the inverse susceptibility χ^{-1} typically for $T > 10\theta_{CW}$, as shown in Fig. 2.1.

Pauli Paramagnetism

The above considerations were made for an insulating material. However, in this thesis, we will study intermetallic systems and thus we have to take into account the contribution of the conduction electron spins to the magnetic susceptibility. Within the independent electron approximation and neglecting the orbital response to the applied magnetic field, we find a temperature independent positive magnetic susceptibility:

$$\chi_e = 2\mu_B^2 \eta(E_F), \tag{2.13}$$

where $\eta(E_F)$ is the "*bare*" density of states (DOS) for one spin direction at the Fermi surface (FS). This is known as Pauli paramagnetic susceptibility and its order of magnitude is comparable to the diamagnetic one, in huge constrast to the larger paramagnetic susceptibility. This is because the exclusion principle is far more effective than thermal disorder in suppressing the tendency of the spin magnetic moments to align with the field.

If we now consider electron-electron exchange interaction, the magnetic susceptibility is, in general, enhanced:

$$\chi_e = 2\mu_B^2 \frac{\eta(E_F)}{1 - \alpha}, \tag{2.14}$$

where $(1 - \alpha)^{-1}$ is the Stoner enhancement factor [48, 63, 34].

2.1.2 Magnetic interactions

When deriving Curie's law (eq. 2.8) for paramagnetism we assumed that the paramagnetic ions are independent magnetic moments. However, there are different types of magnetic interactions

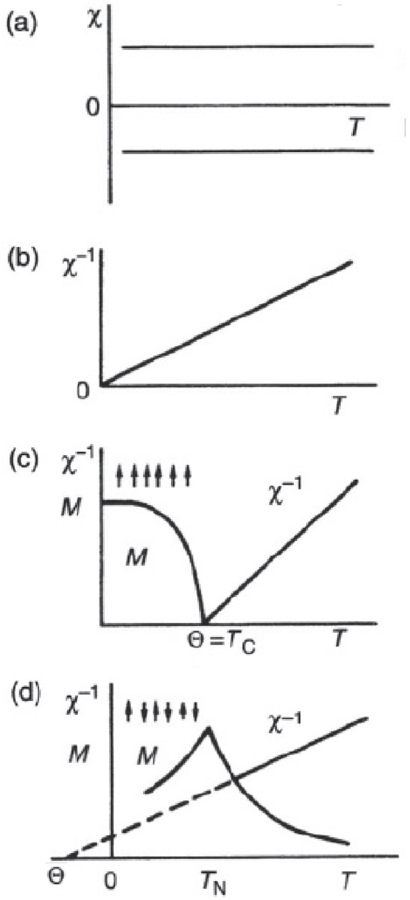

Figure 2.1: Summary of the magnetic susceptibility temperature dependence presented in this section. a) Pauli paramagnetism and diamagnetism; b) Curie paramagnetism; (c) ferromagnetism; (d) antiferromagnetism. Figure extracted from ref. [34].

that can allow the magnetic moments in a solid to communicate with each other and to potentially realize long range order.

Magnetic dipolar interaction

The first expected interaction is the direct dipolar interaction energy of two magnetic dipoles $\mathbf{m_1}$ and $\mathbf{m_2}$ separated by a distance $\mathbf{r}$:

$$E = \frac{1}{r^3}\left[\mathbf{m_1}\cdot\mathbf{m_2} - 3(\mathbf{m_1}\cdot\hat{\mathbf{r}})(\mathbf{m_2}\cdot\hat{\mathbf{r}})\right]. \tag{2.15}$$

We can estimate the order of magnitude of this effect in a magnetic solid, where moments are typically $\approx g\mu_B$ and are separated by ≈ 2 Å. Thus, $E \sim 10^{-4}$ eV (equivalent to only 1 K) and hence magnetic dipolar interaction is too weak to account for ordering in most magnetic materials that order at much higher temperatures.

Exchange interaction

On the other hand, if we turn our attention to electrostatic energy differences between atomic states, we notice that they are typically a fraction of an electron-volt and they could play an important role. In fact, due to Pauli exclusion principle, the electrostatic energy of a pair of magnetic ions depends on the relative orientation of their moments so that an effective magnetic exchange interaction between them arises. We can write the spin Hamiltonian for the simple case of two electrons as:

$$\mathcal{H}^{spin} = -J\mathbf{S}_1 \cdot \mathbf{S}_2, J = E_{singlet} - E_{triplet}. \tag{2.16}$$

Here, J is the exchange coupling constant. We note that $\mathcal{H}^{spin}$ will favor parallel spins (triplet state $S = 1$) if $J > 0$ and antiparallel spins if $J < 0$ (singlet state $S = 0$).

There are a large variety of exchange interactions that can occur in a solid, namely:

- *Direct exchange* occurs when the interaction arises directly from the Coulomb interaction with no need for an intermediary;
- *Superexchange* is an indirect exchange in ionic solids mediated by a nonmagnetic ion;
- *Ruderman-Kittel-Kasuya-Yosida (RKKY)*, which is also an indirect exchange but mediated by the conduction electron in metals;
- *Double exchange*, which is a ferromagnetic exchange due to the mixed valency of a magnetic ion;
- *Anisotropic exchange (or Dzyaloshinski-Moriya interaction)* is possible when the spin-orbit coupling produces an excited state in one magnetic ion that can interact with the ground state of another ion;
- *Itinerant exchange* is the exchange interaction in metals among the conduction electrons themselves.

Very often direct exchange can not control the magnetic properties since there is insufficient direct overlap between neighbouring magnetic orbitals. For example, the mean radius of an f-shell in rare earth series is typically one tenth of the interionic spacing, as shown in Fig. 2.2. Thus they generally overlap very little and the direct exchange is weak. Even in transition metals, such as Fe, Co and Ni, where the $3d$ orbitals extend further from the nucleus, it is extremely difficult to have direct exchange playing a role in the observed magnetic properties.

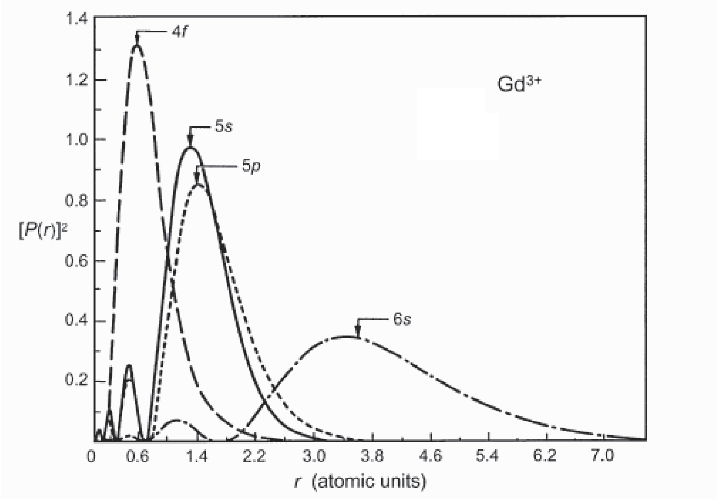

Figure 2.2: The Hartree-Fock radial densities of Gd^{3+} (similar to Eu^{2+}). Figure extracted from ref. [47]

As pointed out in the first chapter, in this thesis we will study the EuFe$_2$As$_2$ member, which has two antiferromagnetic ground states: a localized one due to the RKKY exchange interaction between Eu^{2+} ions and an itinerant SDW one due to the itinerant exchange between Fe $3d$ electrons. Therefore, we will concentrate our analysis on these two interactions.

Rare-earth $4f$ local moments are embedded in a sea of conduction electrons that can be spin polarized and subsequently interact with neighbouring local moments, resulting in an indirect long-range oscillatory coupling. In order to understand this phenomenon, one can write the Hamiltonian of the exchange interaction between a conduction electron with spin $\mathbf{s}$ at $\mathbf{r}$ and an ionic spin $\mathbf{S}$ at position $\mathbf{R}$:

$$\mathcal{H}_{sf} = -J_{fs}(\mathbf{r}-\mathbf{R})\mathbf{s}\cdot\mathbf{S}. \tag{2.17}$$

As $\mathcal{H}_{sf}$ is spin dependent, conduction electrons with different spin orientation respond differently to the perturbation. Hence, if $J_{fs}(\mathbf{r}) < 0$, conduction electrons with the same spin orientation as the ionic spin prefer to be near $\mathbf{S}$, while those of spin antiparallel do not. This polarization produced by one ionic spin will interact with another spin at a distance $\mathbf{r}$ through $\mathcal{H}_{sf}$. In order to work with Bloch waves for the conduction electron it is convenient to work in the reciprocal space. Then, using second-order perturbation theory, we obtain the effective exchange interaction between the two spins:

$$\mathcal{H}_{ij} = -J_{RKKY}\mathbf{S}_i \cdot S_j, \qquad J_{RKKY} = \sum_{\mathbf{q}} J_{fs}^2(\mathbf{q})\chi(\mathbf{q})e^{i\mathbf{q}\cdot\mathbf{r}}, \tag{2.18}$$

where $\chi(\mathbf{q})$ is the wave vector ($\mathbf{q} = \mathbf{k} - \mathbf{k}'$) dependent susceptibility of the conduction electron system which yields the response of the electron gas to the exchange field of localized spin. Finally, using the RKKY approximation, $J_{fs}(\mathbf{q}) = J_{fs}$, we find the familiar RKKY exchange interaction:

$$J_{RKKY} = \frac{9\pi}{2\epsilon_F}\frac{J_{fs}^2\eta^2(E_F)}{r^3}\left(\frac{sin(2k_F r)}{r} - 2k_F cos(2k_F r)\right). \tag{2.19}$$

Here, E_F is the Fermi energy, k_F is the radius of the conduction-electron Fermi surface, and $\eta^2(E_F)$ is the conduction-electron density of state at E_F. The RKKY interaction can be ferro or antiferromagnetic, depending on the distance between the two moments, as shown in Fig. 2.3.

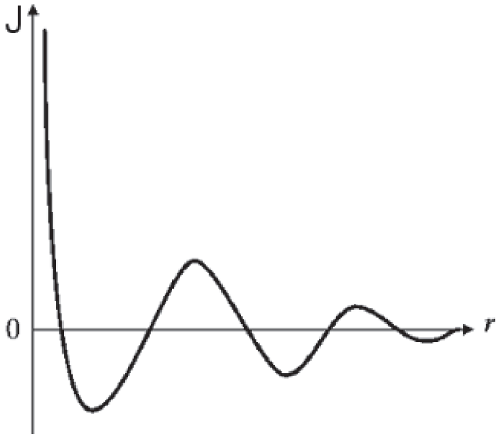

Figure 2.3: Indirect J$_{RKKY}$ exchange interaction of a free electron gas.

In general, the electron gas by itself also contains a rich spectrum of excitations that can be treated by calculating $\chi(\mathbf{q},\omega)$ via perturbation theory. In particular, the $\mathbf{q}$-dependent susceptibility without Coulomb interactions can be written as:

$$\chi_{\mathbf{q}}^0 = \chi_e f(q/2k_F), \tag{2.20}$$

where $f(x) = \frac{1}{2}\left(1 + \frac{1-x^2}{2x}log|\frac{x+1}{x-1}|\right)$.

As mentioned before, this susceptibility is enhanced in the presence of Coulomb interactions and becomes:

$$\chi_{\mathbf{q}} = \frac{\chi_e f(q/2k_F)}{1 - U\eta(E_F) f(q/2k_F)} = \frac{\chi^0_{\mathbf{q}}}{1 - \alpha\chi^0_{\mathbf{q}}}, \tag{2.21}$$

where $\alpha = U/\mu_B^2$, $U = \mu_B^2\lambda$ is a measure of the Coulomb energy, and λ is the molecular field. It may occur that $\chi^0_{\mathbf{q}}$ has a maximum at $\mathbf{q} \neq 0$. In this case, the interactions can cause a divergence in the susceptibility at this vector $\mathbf{q}$ if $1 - \alpha\chi^0_{\mathbf{q}} = 0$. Hence, the electron gas would become unstable, and an oscillatory static magnetization could spontaneously develop in the sample. If $\mathbf{q} = 0$ this would correspond to a ferromagnetic order; if $|\mathbf{q}| = \pi/a$ then antiferromagnetic order could develop. Indeed, spin-density wave (SDW) structures with wave vector $\mathbf{q}$ occur in the iron pnictides. In three dimensions, a SDW cannot produce an energy gap at all points on the Fermi surface (FS). Sometimes the FS is such that a translation by a vector $\mathbf{q}$ places a part of it on top of another part. This phenomenon is known as nesting. A SDW with wave vector $\mathbf{q}$ can produce energy gaps along the region of the FS for which nesting is possible. In real metals, it very often happens that two pieces of the Fermi surface are approximately translated from one another in k-space by a fixed wave vector $\mathbf{q}$. This can give rise to a peak in the susceptibility and resulting instability. The formation of the SDW is said to nest the Fermi surface. If the nesting wave vector $\mathbf{q}$ turns out to be π/a where a is the spacing between atoms, the SDW is commensurate with the lattice and antiferromagnetic order results, Fig. 2.4a. However, if $\mathbf{q}$, which is equal to $2k_F$, is not a simple multiple of π/a the SDW becomes incommensurate, as shown in Fig. 2.4b.

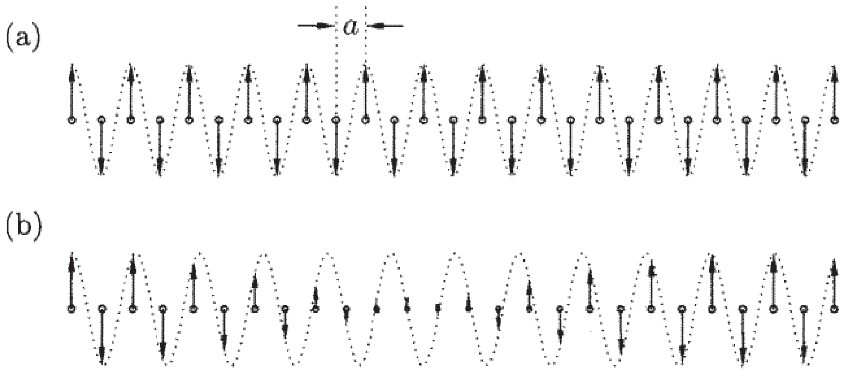

Figure 2.4: (a) Commensurate spin-density wave with wave vector $q = \pi/a$. (b) Incommensurate spin-density wave. Figure extracted from ref. [63].

2.2 Superconductivity

In addition to magnetic ordering, another failure of the independent electron approximation is the phenomenon of superconductivity. In 1911, the dutch physicist H. K. Onnes discovered that mercury (Hg) suddenly exhibited zero resistance below the liquifying helium temperature [64], as shown in Fig. 2.5a. Although infinite conductivity is the most obvious characteristic, another key property of the superconducting state was established in experiments first performed by Meissner and Ochsenfeld: the magnetic flux density **B** is expelled from the interior of a superconductor (perfect diamagnetism) below the superconducting transition temperature T_c, Fig. 2.5b. This is the so called Meissner effect, as the magnetic field H is turned on, a certain amount of energy is spent to establish the magnetic field of the screening currents which cancels the field in the interior of the superconductor. If the applied field is large enough it will become energetically unfavorable for the sample to revert back to the normal state, allowing the field to penetrate. This field is the critical field $H_c(T)$.

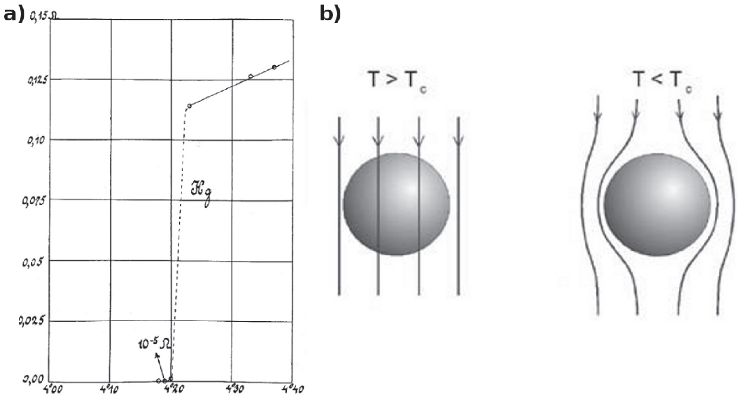

Figure 2.5: a) The resistivity of a capillary of mercury as a function of temperature. b) Magnetic flux expulsion from the interior of a superconductor (Meissner effect). Figure extracted from ref. [64].

2.2.1 Conventional Superconductivity

Based on this experimental fact, the London brothers proposed a phenomenological model based on the fundamental assumption that the equation

$$\nabla \times \mathbf{J} = -\frac{n_s e^2}{mc}\mathbf{B}, \tag{2.22}$$

correctly describes a superconductor under all circunstances. Here, n_s is the electron superconducting density, $-e$ is the charge of an electron, and $\mathbf{J}$ is the supercurrent. Since $\mathbf{B} = \nabla \times \mathbf{A}$, where $\mathbf{A}$ is the magnetic vector potential, the assumption above becomes the London equation:

$$\mathbf{J} = \frac{n_s e^2}{mc}\mathbf{A}. \tag{2.23}$$

The Coulomb gauge ($\nabla \cdot \mathbf{A} = 0$) was chosen in order to satisfy the continuity equation $\nabla \cdot \mathbf{J} = 0$.

A combination of Equation 2.22 and the Ampere's law for static fields gives the following differential equation that, in the simple case of a superconducting slab of width $z = 2d$ with applied field $\mathbf{H}_0 = H_0 \hat{x}$, has a clarifying solution:

$$\nabla^2 \mathbf{B} = \lambda^{-2} \mathbf{B}, \quad \Rightarrow \quad B_z = H_0 e^{-z/\lambda}, \tag{2.24}$$

where

$$\lambda = \sqrt{\frac{mc}{4\pi_s e^2}} \tag{2.25}$$

is known as the London penetration depth. Thus, the magnetic field is confined to a surface layer of thickness $\approx \lambda$. For the element tin (Sn), for example, the experimental penetration depth is $\lambda = 510$ Å.

One can ask why the London equation is valid. Phenomenologically, it follows from the rigidity of a wave-function in the superconducting state. According to Bloch theorem, the total momentum of the system in its ground state has a zero average value $\langle \Psi | \mathbf{p} | \Psi \rangle = 0$. Now, assuming that the wave-function Ψ is rigid, i.e., that this average holds even in the presence of an external field, we have $\langle \mathbf{p} \rangle = m \langle \mathbf{v} \rangle$ - $e \langle \mathbf{A} \rangle / c = 0$, which recovers London equation!

But still one may wonder about the microscopic origin of this rigidity. Moreover, other experimental facts must be taken into account. The specific heat at low temperatures decays exponentially (i. e., $C_s \propto exp(-\Delta_0 / k_B T)$) indicating the existence of a gap in the energy spectrum, separating the excited states from the ground state, as shown in Fig. 2.6. Also, a distinctive property of superconductors is the isotope effect, which shows that the transition temperature typically varies with the ionic mass M of the isotope as $T_c \propto M^{-1/2}$, suggesting that the lattice must play an important role in the supercoducting state formation.

The answer to the above questions only appeared in 1957 (46 years after Onnes' discovery) with the model introduced by Bardeen, Cooper, and Schrieffer (BCS) based on the attractive interaction between electrons in the neighborhood of the Fermi surface mediated by phonons. Although the

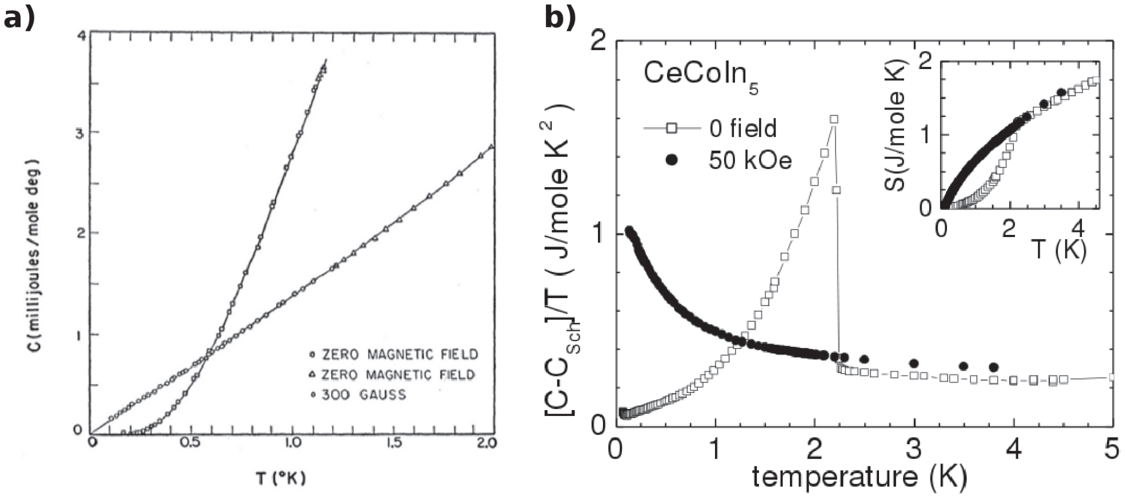

Figure 2.6: a) Specific heat of a conventional type-I superconductor: aluminum (Al). Figure extracted from ref. [65]. b) Specific heat of an unconventional superconductor: CeCoIn$_5$. Figure extracted from ref. [66].

direct electrostatic interaction is repulsive, it is possible for the retarded ionic motion to screen the Coulomb interaction, leading to a net attraction.

Bardeen, Cooper, and Schrieffer constructed a new ground state from the following effective Hamiltonian, written in the second quantized form:

$$H = \sum_{\mathbf{k},\sigma} \varepsilon_{\mathbf{k}} c^{\dagger}_{\mathbf{k},\sigma} c_{\mathbf{k},\sigma} + \frac{1}{N} \sum_{\mathbf{k},\mathbf{k}'} V_{\mathbf{k},\mathbf{k}'} c^{\dagger}_{\mathbf{k}\uparrow} c^{\dagger}_{-\mathbf{k}\downarrow} c_{-\mathbf{k}'\downarrow} c_{\mathbf{k}'\uparrow}. \tag{2.26}$$

Here, $c^{\dagger}_{\mathbf{k}\sigma}$ creates an electron with momentum $\mathbf{k}$ and spin σ, and the chemical potential μ is included in the definition $\varepsilon_{\mathbf{k}} = \epsilon_{\mathbf{k}} - \mu$. Therefore, the term $c_{-\mathbf{k}'\downarrow} c_{\mathbf{k}'\uparrow}$ describes the destruction of a Cooper pair, i.e., two electrons with opposite momenta and spin. The subsequent term $c^{\dagger}_{\mathbf{k}\uparrow} c^{\dagger}_{-\mathbf{k}\downarrow}$ describes the creation of another Cooper pair. In real space, these correlations extend out to a distance known as the BCS coherence length ($\xi = \hbar v_F / \pi \Delta_0 \sim 10^3 - 10^4$ Å) which is a typically much larger than the inter-particle separation.

For many systems, the physics becomes clearer in a direct approach where we simplify the original second-quantized hamiltonian with a canonical transformation and obtain an approximate problem that is exactly solvable. In this manner, we perform the usual mean-field decoupling of the quartic term and then employ the Bogoliubov transformation. The effective Hamiltonian can be diagonalized:

$$H = \sum_{\mathbf{k},\sigma} E_{\mathbf{k}} \gamma^{\dagger}_{\mathbf{k},\sigma} \gamma_{\mathbf{k},\sigma} + E_0, \tag{2.27}$$

where $\gamma_{\mathbf{k}\sigma}$ is the new fermionic operator, E_0 is the ground state energy:

$$E_0 = \sum_{\mathbf{k}} \left(\varepsilon_{\mathbf{k}} - E_{\mathbf{k}} + \Delta_{\mathbf{k}} \langle c^{\dagger}_{\mathbf{k}\uparrow} c^{\dagger}_{-\mathbf{k}\downarrow} \rangle \right), \tag{2.28}$$

and $E_{\mathbf{k}}$ is the excitation energy:

$$E_{\mathbf{k}} = \sqrt{\varepsilon^2_{\mathbf{k}} + |\Delta_{\mathbf{k}}|^2}. \tag{2.29}$$

Here, $\Delta_{\mathbf{k}}$ is the gap function. At the Fermi level ($\varepsilon_{\mathbf{k}} = 0$) the energy spectrum of the superconductor has a gap of size $|\Delta_{\mathbf{k}}|$ determined self-consistently by:

$$\Delta_{\mathbf{k}} = -\frac{1}{N} \sum_{\mathbf{k}'} \frac{V_{\mathbf{k}\mathbf{k}'} \Delta_{\mathbf{k}'}}{2E'_{\mathbf{k}}} tanh(\frac{E'_{\mathbf{k}}}{2k_B T}) \tag{2.30}$$

For a phonon-mediated electronic interaction, we consider a constant attractive potential $V_{\mathbf{k}\mathbf{k}'} = -V_0$ for a shell of thickness $\hbar\omega_D$ around the Fermi energy. We then look for a gap function Δ that is also $\mathbf{k}$-independent and real, the so called $s - wave$ gap. Since $\hbar\omega_D \ll \mu$, we assume that the density of states per spin is approximately equal to the density of states at the Fermi level $\eta(E) = \eta(E_F)$ and as a consequence we obtain a self-consistent equation for the gap function at an arbitrary temperature:

$$1 = V_0 \eta(E_F) \int_0^{\hbar\omega_D} \frac{dE}{\sqrt{E^2 + \Delta^2}} \tanh(\frac{\sqrt{E^2 + \Delta^2}}{2k_B T}). \tag{2.31}$$

For $T = 0$ we have a finite gap Δ_0 for an arbitrarily small atractive interacion V_0:

$$\Delta_0 = 2\hbar\omega_D e^{-\frac{1}{V_0 \eta(E_F)}}. \tag{2.32}$$

This fact shows that the Fermi liquid state is unstable towards the formation of the BCS superconducting state. Moreover, for $\Delta \to 0$ we can obtain the superconducting transition temperature:

$$T_c = \frac{2e^{\gamma_E}}{\pi} \frac{\hbar\omega_D}{k_B} e^{-\frac{1}{V_0 \eta(E_F)}}, \tag{2.33}$$

which again is non-zero for any arbitrarily small V_0. Combining the last two equations we obtain the familiar universal ratio between the zero-temperature gap and the critical temperature:

$$\frac{\Delta_0}{k_B T_c} \approx 1.76. \tag{2.34}$$

The verification of the above relashionship in most of the known superconductors at that time was one of the early sucesses of the BCS theory. In addition, the theory explains the isotope effect since $T_c \propto \omega_D \propto M^{-1/2}$. It also predicts a universal ratio between the specific heat jump and its value in the normal state:

$$\frac{\Delta c}{c_n}\Big|_{T=T_c} \approx 1.43. \tag{2.35}$$

The agreement of this prediction with experiments is good to about 10 percent, except for the strong-coupling superconductors (e.g., mercury and lead). Besides the low-temperature electronic specific heat can be cast in a parameter independent form:

$$\frac{c_s}{\gamma T_c} = 1.34 \left(\frac{\Delta_0}{T}\right)^{3/2} e^{-\Delta_0/T}, \tag{2.36}$$

where γ is the coefficient of the linear term in the specific heat of the metal in the normal state. It is worth noting that the corrected γ value due to the electron-phonon coupling λ is $\gamma = (2/3)\pi^2 k_B^2 \eta(E_F)(1+\lambda)$.

Finally, the BCS theory determines the critical field:

$$H_c(T) = 1.74 H_c(0)(1 - \frac{T}{T_c}), \tag{2.37}$$

where $H_c(0) = [4\pi\eta(E_F)\Delta_0]^{1/2}$ is the critical field at $T = 0$.

There are two distinguishable types of behavior for the magnetic field to penetrate the sample that depends on the Ginzburg-Landau parameter $\kappa = \lambda/\xi$, i.e., the ratio between the coherence length, $\xi = \frac{\hbar}{\sqrt{2m^*\alpha}}$, and the penetration depth λ:

- **Type I -** $\kappa < 1/\sqrt{2}$: Above the critical field $H_c(T)$ the entire sample enters the normal state and the field penetrates perfectly. In this type $H_c(T) \approx 10^2 G$;
- **Type II -** $\kappa > 1/\sqrt{2}$: Above a lower critical field $H_{c1}(T)$ we have a mixed state, where there is partial penetration of flux in the form of non superconducting thin filaments. Circulating around each filament is a vortex of screening current and the rest of the sample is superconducting. When the applied field exceeds $H_{c2}(T)$ (up to $\approx 10^5 G$), the entire sample enters the normal state.

The BCS theory is a weak coupling mean field theory that can not explain type II conventional superconductors. For intermediate and mixed states, in which the magnetic field enters in a nonperturbative manner, one have to make use of the phenomenological theory of Ginzburg-Landau (GL) [5]. In fact, Gor'kov showed that the GL equations follow from the BCS theory when T is near T_c and the magnetic field varies slowly in space over a coherence length [49]. Furthermore, based on the fact that a controlled perturbation expansion existed for the electron-ion interaction, Nambu and Eliashberg generalized the BCS theory [51, 52]. The resulting strong coupling theory was developed by Schrieffer and colleagues and gave a good description of $\mathrm{MgB_2}$, the conventional superconductor with the highest T_c so far, 40 K [53].

Apart from the successful theoretical development, the retarded net attraction due to phonons is essentially small, resulting in a limitation to T_c. In addition, none of the existing theories could predict new superconductors and/or superconductivity in related materials.

Shortly after the BCS theory was published, Anderson realized that the state should survive even in the presence of disorder, since one can always define time reversed states even if the momentum states are smeared out due to impurity scattering [50]. However, magnetic impurities act differently in that they flip the spin and thus break the singlets. The decrease of the transition temperature, ΔT_c, with increasing magnetic impurity concentration, Δc, is described by Abrikosov-Gorkov theory [36]:

$$\left|\frac{\Delta T_c}{\Delta c}\right| = \frac{\pi^2}{8k_B}\langle J^2(q)\rangle_{E_F}\eta(E_F)(g_J-1)^2J(J+1), \tag{2.38}$$

where $\langle J^2\rangle_{E_F}$ is the average of the exchange parameter J over the Fermi surface and $\eta(E_F)$ is the density of states at the Fermi level.

2.2.2 Unconventional Superconductivity

Therefore, in 1967 it came as a surprise the fact that superconductivity was observed in ferromagnetic or antiferromagnetic uranium-based intermetallic compounds U_6X (X =Mn, Fe, Co, and Ni) with T_c ranging from 0.4 to 3.9 K. After that, superconductivity was discovered in $\mathrm{U_2PtC_2}$ at 1.47 K (1969) and in $\mathrm{UBe_{13}}$ at 0.9 K [54, 55]. Despite all these discoveries, because elemental α-U was suspected of being a conventional superconductor, these results triggered less curiosity than they should have. It took the discovery of superconductivity in $\mathrm{CeCu_2Si_2}$ by F. Steglich in 1979 to realize that a new class of superconductors had been unveiled [56]. By that time, it had been discovered that a number of rare-earth and actinide intermetallics exhibited a linear specific heat coefficient at low temperatures, typical of a Fermi liquid. The difference, though, was that its magnitude was huge, up to 1000 times that of copper. This indicated that the quasiparticles in such materials were strongly interacting, with the f electrons being both nearly localized and nearly magnetic. Neutron scattering measurements in UPt_3 indicated the presence of antiferromagnetic spin fluctuations, not ferromagnetic spin fluctuations as in He^3 superfluid state, where the pairing was p-wave. Hence, one could expect that this difference would lead to d-wave singlet pairing. In fact, nodes in the superconducting gap of UPt_3 were confirmed in 1986 from the polarization dependence of the ultrasound attenuation [57].

---

[5] for a more detailed discussion see, for example, ref. [35]

However, the highest T_c since 1973 was only 23 K in Nb_3Ge until the discovery in 1986 of the first high-temperature singlet d-wave superconductor: the cuprates. J.G. Bednorz and K.A. Müller observed that the lanthanum-based cuprate perovskite material $LaBaCuO_4$ develops superconductivity at $T_c = 35$ K [58]. The impact of this discovery can be seen in the fact that Bednorz and Müller received the Nobel prize in Physics for this discovery one year later. Remarkably, the highest-temperature superconductor at ambient pressure, $HgBa_2Ca_2Cu_3O_{9+\delta}$, reaches a T_c of 138 K and 164 K under a pressure of ~ 30 GPa!

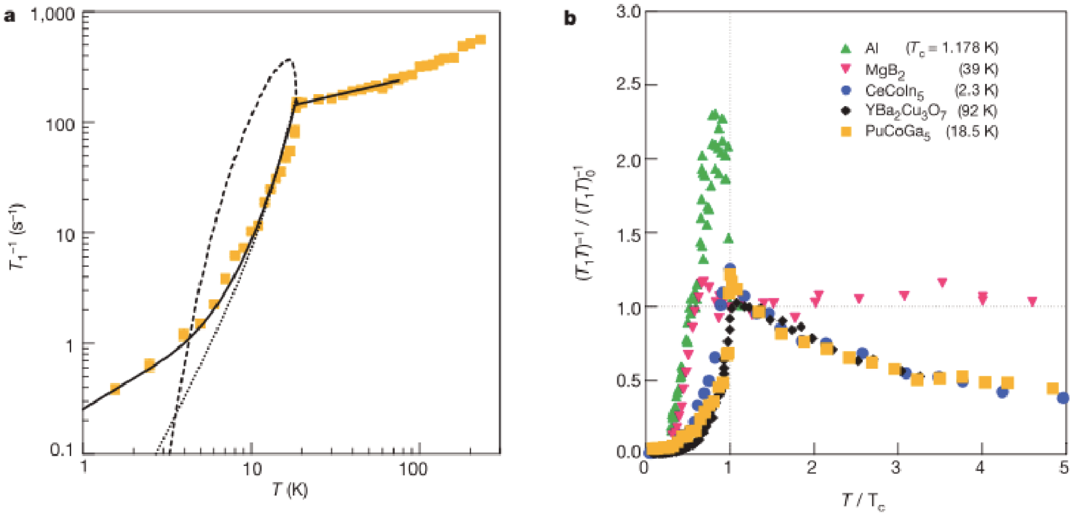

Figure 2.7: The spin-lattice relaxation rate in the normal and superconducting states. a) $1/T_1$ data for $^{69}Ga(1)$, as well as calculations for BCS isotropic s-wave (dashed), pure (dotted) and dirty (solid) d-wave gap functions. The solid line in the normal state shows $T^{0.35}$. b) $(T_1T)/(T_1T)_0^{-1}$ versus T/T_c for $PuCoGa_5$, as well as for the unconvenctionl cuprate superconductor $YBa_2Cu_3O_7$ ($T_c = 92$ K) and $CeCoIn_5$ ($T_c = 2.3$ K) and s-wave superconductors Al and MgB_2. Figure extracted from ref. [67].

The discovery of the new class of heavy-fermion superconductors CeMIn$_5$ and PuMGa$_5$ ($M =$ Co,Rh,Ir), with T$_c$ = 2.3 K and 18.5 K for the M = Co members, where the interplay between magnetism and superconductivity resembles the phase diagram of the cuprates, provided an opportunity to bridge the understanding of unconventional superconductivity in these two classes of presumably magnetic-mediated superconductors [5, 37]. The anisotropic nature of the pairing is readily observed from the power-law dependence of the nuclear magnetic resonance (NMR) relaxation rate and from the specific heat capacity dependence on the temperature, as shown in Figures 2.6b and 2.7. Moreover, the normalized relaxation rates of PuCoGa$_5$, high-Tc YBa$_2$Cu$_3$O$_7$ and CeCoIn$_5$ in the normal state scale onto a common curve as a function of the dimensionless parameter T/T_c and suggest that they have similar antiferromagnetic spin fluctuations which dominate the relaxation rate.

In recent years other unconventional superconductors not based on the cuprate structure have been discovered, such as the iron-based superconductors. By *unconventional* we mean a pair state that is not an isotropic nodeless s-wave state, and where the interaction is other than the conventional electron-phonon interaction. Interestingly, these materials often have a magnetic phase that can be suppressed toward a superconducting state, as discussed in Chapter 1. Based in this experimental fact, many theoretical models have been proposed taking into account magnetic fluctuations due to the proximity of the magnetic ordered phase. Some of these theories are based on the magnetic instabilities in the Fermi surface [38, 39, 71]; others consider the role of orbital fluctuations [17, 68], and more sophisticated ones even include the Kondo effect as a possible pairing mechanism [40, 41]. In the particular case of FeAs compounds, the spin fluctuation theories can generate the s_{+-} pairing state which is believed to be the case in BaFe$_2$As$_2$.

Contrary to the BCS case, the similarities between the high-temperature superconductors could allow one to predict new superconductors and/or superconductivity in related materials. In particular, besides the proximity to a magnetic phase, it is striking that many unconventional superconductors have a 2D layered crystal structure. In fact, CeCu$_2$Si$_2$, URu$_2$Si$_2$ and BaFe$_2$As$_2$ all have the ThCr$_2$Si$_2$ structure, suggesting that the crystal field effects can play a crucial role in the interplay between magnetism and superconductivity. In the next section, we will see how this is possible.

2.3 Crystal Field Effects

An ion confined within a crystalline solid is subjected to a static crystalline electric field (CEF) whose sources are the surrounding point charges (ions) arranged in the symmetry given by the periodic lattice. By adding this interaction to the hamiltonian of the free ion, the initially spherical wavefunction (charge density) is modified and the degeneracy in the electronic orbital states is lifted. CEF effects are usually important for d and f orbitals, i.e., transition metals and rare-earth/actinide metals.

As discussed in section 2.1.2, the rare-earth $4f$ electrons lie fairly deep whithin the ion and are well shielded by the $5s^2 5p^6$ shells. In this case, the CEF is weaker than the spin-orbit interaction ($\lambda \mathbf{L} \cdot \mathbf{S}$) and acts as a perturbation in the $2J + 1$ ($J = L + S$ being a good quantum number) multiplet levels, partially lifting its degeneracy by introducing a CEF splitting. In particular, we study the Eu^{2+} ($J = 7/2$) rare-earth ion in this thesis where the CEF effect is a higher order effect due to the fact that $L = 0$. In fact, one can observe from the magnetic susceptibility measurements that the Eu^{2+} ion behaves as a free-ion and it is clear that the CEF splittings are much smaller than the multiplet separations, so that the mixing of different multiplets can be neglected.

On the other hand, d-electrons in transition metals are not shielded and the crystal field perturbation is greater than for the f electrons. In particular, for light transition elements, such as the $3d$ elements, the CEF pertubation is greater than the spin-orbit coupling (the so called intermediate ligand field case). Hence the crystal field problem is solved first, and the spin orbit interaction is treated as a perturbation. As mentioned in the introduction, the main contribution to the Fermi surface in the iron pnictides is from the Fe $3d$ electrons, so for now on, we will discuss in detail the effect of a (distorted) tetrahedral CEF in the Fe $3d^6$ ground state.

In the case of a regular tetrahedron, the Fe ion has four As ligands located at the corners of a cube (see Fig. 1.5 in Chapter 1). In this tetrahedral ligand field, the Fe $3d$ orbitals directed toward the As ligands feel a greater electrostatic repulsion. This leads to an alteration of the energies of the formely degenerate d orbitals and causes $d_{x^2-y^2}$ and d_{z^2} to become smaller in energy, forming what is called in group theory the e_g set. On the other hand, the t_{2g} set, formed by d_{xy}, d_{xz} and d_{yz} orbitals become higher in energy. The crystal field splitting, Δ, is shown in Fig. 2.8. If Δ is larger than the Coulomb repulsion between two electrons with opposite spins in the same orbital, then we will obtain the low spin configuration $S = 0$ (not shown). On the other hand, if the energy required to pair two electrons is greater than the energy cost of placing an electron in a t_{2g} state, high spin configuration $S = 2$ occurs as shown in Fig. 2.8.

However, in the real tetragonal material the FeAs_4 tetrahedra is distorted (see Fig. 1.5b). In this case, the states d_{xz} and d_{yz} are still almost degenerate (with a small splitting Δ^* (not shown) but there is a further CEF splitting Δ_t between them and the d_{xy} state. Moreover, there is a splitting Δ_e between $d_{x^2-y^2}$ and d_{z^2}. Thus, by changing the FeAs bond distance, d_{FeAs}, we can control these crystal-field splittings and in turn determine the weigth of each orbital character in the Fermi surface. This is crucial for the spin-density wave (SDW) phase formation, which occurs in close connection with a structural transition from tetragonal to orthorrombic structure (Z^2 symmetry breaking) due to the symmetry break between xz and yz bands [73]. In addition,

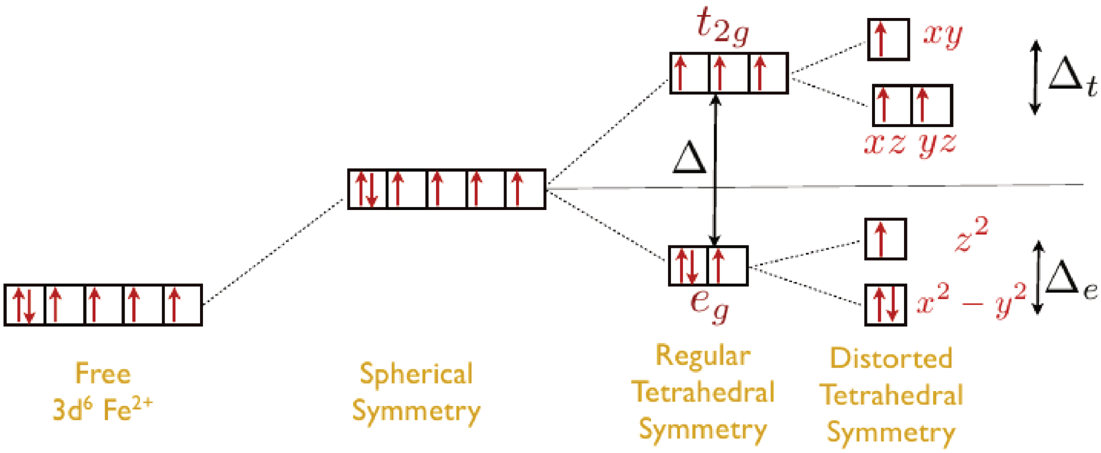

Figure 2.8: Crystal field scheme for a $3d^6$ Fe^{2+} ion in spherical, tetrahedral and distorted tetrahedral symmetry.

the orbital content is also crucial for the emergence of superconductivity (SC) when this SDW phase is suppressed, as we will discuss in Chapter 5 enlightened by our results.

It is clear the crucial influence of the surroundings in lifting the corresponding degeneracy of the Fe $3d^6$ ion. Van Vleck has shown that the absence of orbital degeneracy is a sufficient condition for the quenching of the orbital momentum ($\mathbf{L} = 0$). The proof is straighforward and can be found in ref. [74].

Now we will finish this chapter by introducing the phenomenon of electron spin resonance and discuss how it can provide valuable information about magnetism, superconductivity and crystal field effects.

2.4 Electron Spin Resonance

Section 2.1.1 discussed the paramagnetic response of substances with unpaired electrons to a static applied field H_0. In this section we will present the response of a system of paramagnets to an additional oscillating magnetic field H_1 perpendicular to H_0, that induces dipole transitions between the Zeeman energy levels. This spectroscopic technique is called Paramagnetic Resonance and in this thesis we will be restricted to Electron Spin Resonance (ESR) which is concerned with the study of intrinsic magnetic moments of electronic origin. This study is usually done at microwave-frequencies ($\sim$ GHz) due to the Zeeman splitting of $\sim$ meV between energy levels.

The total Hamiltonian for the electrons of a paramagnetic ion in a crystal with an applied static magnetic field is [59]:

$$\mathcal{H} = \mathcal{H}_0 + \mathcal{H}_{SO} + \mathcal{H}_{hf} + \mathcal{H}_{CF} + \mathcal{H}_Z + \mathcal{H}_d + \mathcal{H}_{ex}, \tag{2.39}$$

where $\mathcal{H}_0$ is the unperturbed hamiltonian; $\mathcal{H}_{SO} = \sum \lambda_{ij}\mathcal{L} \cdot \mathcal{S}$ is the spin-orbit coupling; $\mathcal{H}_{hf} = \sum A_i \mathbf{J_i} \cdot \mathbf{I}$ is the hyperfine coupling between the electron moment and the nuclear spin; $\mathcal{H}_{CF} = \sum -e_i \Phi_{CEF}(\mathbf{r_i})$ gives the crystal field splittings; $\mathcal{H}_Z = \sum_j g\mu_B H_0 S_{zj}$ is the Zeeman term; $\mathcal{H}_d = \sum_{k>j} g^2 \mu_B^2 r_{jk}^{-3}[\mathbf{S}_j \cdot \mathbf{S}_k - 3(\mathbf{S}_j \cdot \hat{\mathbf{r}}_{jk})(\mathbf{S}_k \cdot \hat{\mathbf{r}}_{jk})]$ is the dipolar interaction between paramagnetic ions; $\mathcal{H}_{ex} = -\sum 2J_{ij}\mathbf{S}_i \cdot \mathbf{S}_j - \sum Jij\mathbf{S} \cdot \mathbf{s}$ is the exchange interaction between neighboring local moments and between local moments and conduction electrons, respectively.

Thus, the ESR transitions can provide important information about all the terms in the Hamiltonian of eq. 2.39. However, in order to illustrate the ESR phenomenon, we first consider the simplest case of a large organic molecule, known as DPPH ($\alpha\alpha' - diphenyl - \beta - picrylhydrazyl$), which has a single unpaired electron with $L = 0$. In a typical ESR experiment, a static magnetic field is slowly varied in the range $0 < H < 2$ T while a microwave is kept fixed at $\nu = 9.5$ GHz (Fig. 2.9). If the system is at thermal equilibrium, the lower energy level is more heavily populated and there is a net absorption of energy from the oscillating field when the resonance condition is reached:

$$h\nu = g\mu_B H_{RES} \tag{2.40}$$

The selection rule for this transition is $\delta m = \pm 1$. Hence the first information one can get from this experiment is the magnetic field at which the resonance occurs H_{RES} (or, equivalently, the g-factor) which provides information about the magnetic moment, the local magnetic fields, and any nonmagnetic energy splittings. For X-Band frequencies, this condition for DPPH (and most paramagnets) occurs for fields near 3500 G which yields $g = 2$.

In the steady state, the rate at which energy is absorbed from the perturbation H_1 is equal to the rate at which energy leaves paramagnetic degrees of freedom (spin system) and enters other degrees of freedom, i.e., the relaxation rate. ESR has two important relaxation processes: the spin-lattice relaxation rate ($1/T_1$) and the spin-spin relaxation rate ($1/T_2$). In the simplest phenomenological description, it is assumed that the average magnetization $\mathbf{M} = (1/N)\sum_i \vec{\mu}_i$ decays exponentially and obeys the following equation in the presence of an applied field:

$$\frac{d}{dt}\mathbf{M} = \gamma[\mathbf{M} \times \mathbf{H}] - \frac{1}{T}[\mathbf{M} - \chi\mathbf{H}(t)] \tag{2.41}$$

where γ is the magnetogyric ratio, T is the characteristic decay or relaxation time, and the susceptibility χ is defined for a static field as we already discussed $\mathbf{M} = \chi\mathbf{H}$. Writing $\mathbf{H}(t) =$

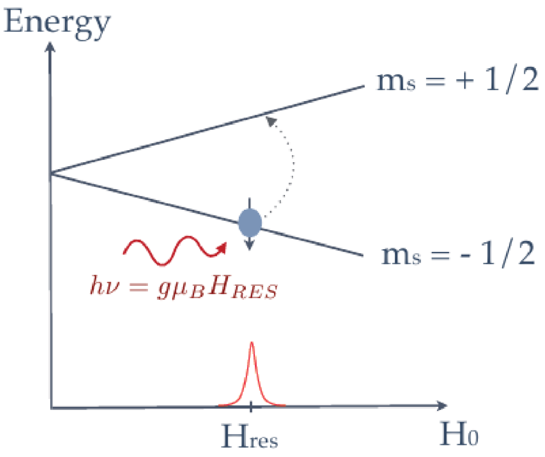

Figure 2.9: Zeeman splitting as a function of the static applied field H_0 for a single unpaired electron with $L = 0$. In an electron spin resonance measurement, a transverse oscillating magnetic field H_1 is applied and an absorption occcurs when $h\nu = g\mu_B H_{RES}$.

$H_0\hat{z} + \mathbf{H}_1(t)$, where $H_1(t)$ is a microwave field rotating in the $x - y$ plane[6] and linearizing equation 2.41 results in:

$$\frac{d}{dt}\mathbf{M}^+ = \left[-i\omega_s - \frac{1}{T}\right](\mathbf{M}^+ - \chi\mathbf{H_1}), \tag{2.42}$$

where M^+ is defined by $M^+ = M_x + iM_y$ and $\omega_s = -\gamma H_0$.

Hence, we have two characteristic equations for the relaxation processes:

$$\mu_z = |\mu|(1 - e^{-t/T_1}), \tag{2.43}$$

which provides the longitudinal relaxation time T_1 related to the equilibrium between different S_z states. It is related to the thermal equilibrium between the resonating spins and the crystalline lattice system (phonons) or the electronic spin system (conduction electrons).

On the other hand, the spin-spin relaxation time T_2 is given by:

$$\mu_{xy} = |\mu|e^{-t/T_2}, \tag{2.44}$$

---

[6] If $\mathbf{H}_1(t)$ is in z direction, the transition probability between states $|\psi_{-1/2}\rangle$ and $|\psi_{+1/2}\rangle$ due to the perturbation hamiltonian $\mathcal{H}_p = g\mu_B\mathbf{S}\cdot\mathbf{H_1}$ is $|\langle\psi_{+1/2}|H_p|\psi_{-1/2}\rangle|^2 = (g\mu_B)^2 H_{1z}^2 |\langle\psi_{+1/2}|S_z|\psi_{-1/2}\rangle|^2 = 0$. Hence, there is no transition between the states.

which provides the transverse relaxation between a phase coherent state due to the in-plane pulse H_1 and a phase incoherent equilibrium state.

Performing a Fourier transform and defining the transverse dynamic susceptibility as $M^+ = \chi^+(\omega)H_1$ we obtain:

$$\chi^+(\omega) \equiv \chi' + i\chi''(\omega) = \chi + \left[\frac{\chi\omega}{\omega_s - i(1/T) - \omega}\right], \tag{2.45}$$

which is the experimentally observed quantity, Figure 2.10a.

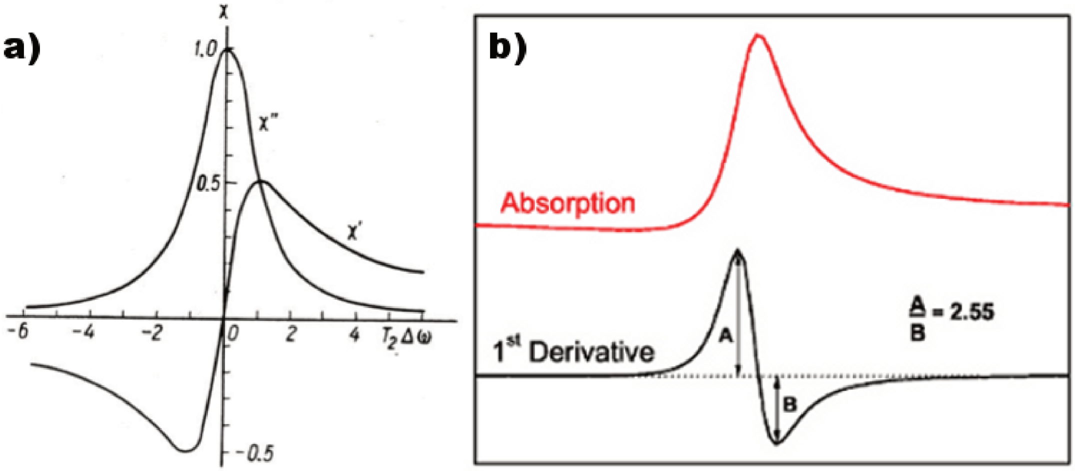

Figure 2.10: a) Real (dispersion) $\chi'(\omega)$ and imaginary (absorption) $\chi''(\omega)$ components of the spin susceptibility. b) Typical absorption line in a metal (Dysonian) and its observed first derivative.

Attemps to determine $\chi^+(\omega)$ involve the fact that the small transmited fraction ($\sim 10^{-4}$) of the microwave field incident upon a metal is rapidly screened by conduction currents and penetrate no more than the *skin depth* δ given by:

$$\delta = \frac{c^2}{2\pi\sigma\omega}, \tag{2.46}$$

where σ is the electrical conductivity.

There are two other important effects: (i) the surface impedance of a metal is complex so that the actual absorption of microwave power is not given simply by the imaginary (absorptive) part $\chi''(\omega)$ of the complex susceptibility, but it is rather a linear combination of the absorptive $\chi''(\omega)$ and dispersive $\chi'(\omega)$ parts; see Figure 2.10b. Hence, the second information we obtain is whether the ion environment is insulating or metallic; (ii) the conduction electrons are mobile and the diffusion of the spins involved in the resonance modifies the position and width of the resonance and further modifies the admixture of dispersion and absorption. This problem was treated by Dyson in 1957 [75].

A more elaborate phenomenological approach allow us to obtain the relaxation rates by solving the Bloch-Hasegawa equations [79]:

$$\frac{d}{dt}\mathbf{M}_s = g_s\mu_B\mathbf{M}_s \times (\mathbf{H} + \lambda\mathbf{M}_e) - \left(\frac{1}{T_{se}} + \frac{1}{T_{sL}}\right)\delta\mathbf{M}_s + \frac{g_s}{g_e}\frac{1}{T_{es}}\delta\mathbf{M}_e, \tag{2.47}$$

$$\delta\mathbf{M}_s = [\mathbf{M}_s - \chi_s^0(\mathbf{H}_{ext} + \lambda\mathbf{M}_e + \alpha\mathbf{M}_s)], \tag{2.48}$$

$$\frac{d}{dt}\mathbf{M}_e = g_s\mu_B\mathbf{M}_e \times (\mathbf{H} + \lambda\mathbf{M}_s) - \left(\frac{1}{T_{es}} + \frac{1}{T_{eL}}\right)\delta\mathbf{M}_e + \frac{g_e}{g_s}\frac{1}{T_{se}}\delta\mathbf{M}_e, \tag{2.49}$$

$$\delta\mathbf{M}_e = [\mathbf{M}_e - \chi_e^0(\mathbf{H}_{ext} + \lambda\mathbf{M}_s + \lambda_e\mathbf{M}_e)], \tag{2.50}$$

where $\lambda = 2J/(g_e g_s \mu_B^2)$ is the molecular-field coefficient, $\frac{1}{T_{eL}}$ is the conduction electron-lattice relaxation rate, $\frac{1}{T_{se}}$ is the spin-conduction electron relaxation rate, $\frac{1}{T_{sL}}$ is is the spin-lattice relaxation via spin-orbit coupling[7]. Fig. 2.11 illustrates these relaxation paths.

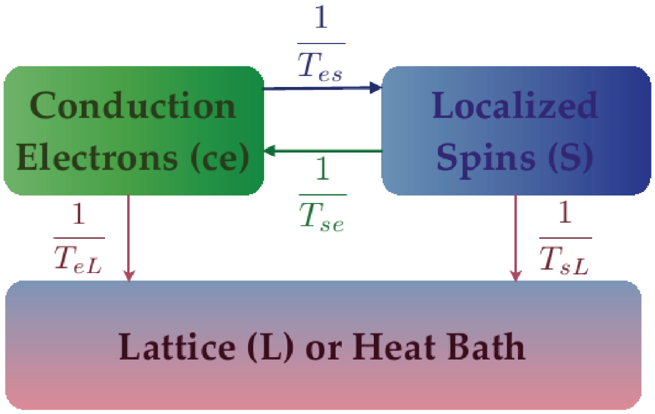

Figure 2.11: Relaxation paths involved in the ESR linewidth.

---

[7] This term can also be regarded as the residual ($T = 0$) linewidth encountered in practice.

If cross-relaxation is rapid, momentum transferred to the conduction electrons can be transferred back to the local moments before it has time to decay to the lattice. This phenomenom is known as *bottleneck* and it happens with greater probability when $g_e = g_s$. However, we will see in Chapter 4 that our system is non-bottleneck and we can disregard $\frac{1}{T_{es}}$. Non-bottlenecked Eu^{2+} and Mn^{2+} systems almost invariably correspond to the isothermal case where $\mathbf{M}_e$ reaches the equilibrium value corresponding to the instantaneous internal field (including the microwave field), i.e.,

$$\mathbf{M}_e = \chi_e^0(\mathbf{H} + \lambda\mathbf{M}_s(t)), \tag{2.51}$$

and there is a rapid conduction electron relaxation with a not too large difference in conduction electron and local moment g-factors. In this case, the equation of motion gives the first order, or "Knight"g-shift:

$$\frac{\Delta g_s}{g_s} = \lambda\chi_e^0 = \frac{g_e}{g_s}\eta(E_F)J, \tag{2.52}$$

which is due to the polarization of the conduction electrons by the local magnetic moment.

In addition, the paramagnetic probes studied in this thesis (Eu^{2+}, Mn^{2+} and Cu^{2+}) have $L = 0$ and we can also disregard $\frac{1}{T_{sL}}$. Moreover, as the relaxation via conduction electrons is the dominant term in metals we can consider $T_2 \approx T_1 = T_{se}$

We now have to treat the effects of the relaxation through the conduction electrons in the isothermal regime. The standard rate-equation approach provides the longitudinal relaxation time T_1 as given by:

$$\frac{1}{T_1} = W_{(+)\to(-)} + W_{(-)\to(+)}, \tag{2.53}$$

where $W_{(+)\to(-)}$ is the rate for a spin-flip $S_z = +\frac{1}{2}$ to $S_z = +\frac{1}{2}$, as illustrated in Fig. 2.12.

In order to calculate the transition rate W within the Fermi's Golden Rule approximation, the exchange interaction is expressed in terms of second-quantized operators:

$$H = -2J\mathbf{S}\cdot\mathbf{s}(\mathbf{R}) = -\frac{J}{N}\sum_{\mathbf{q}}\mathbf{S}\cdot\sigma_{\mathbf{q}}, \tag{2.54}$$

where

$$\sigma_{\mathbf{q}} = \sum_{\mathbf{k}\sigma\sigma'} c^{\dagger}_{\mathbf{k+q}\sigma}\sigma_{\sigma\sigma'}c_{\mathbf{k}\sigma'}, \tag{2.55}$$

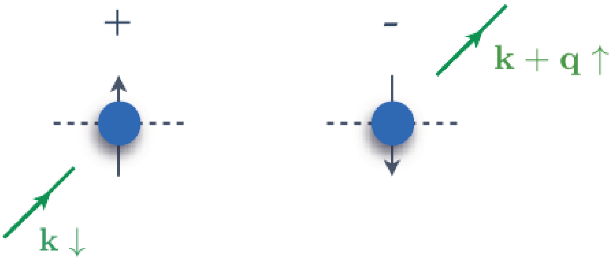

Figure 2.12: Scattering event which, in part, is responsible for the Korringa relaxation rate. The incoming conduction electron $\mathbf{k}\downarrow$ spin-flips against the impurity to terminate in the state $\mathbf{k}+\mathbf{q}\uparrow$.

and $\sigma_{\sigma\sigma'}$ are the Pauli matrices and we assume that the single impurity is at the origin.

Then, the corresponding rate is given by:

$$W_{(+)\to(-)} = \frac{2\pi}{\hbar}\sum_{kq}(\frac{J}{N})^2 n_{k\downarrow}(1-n_{\mathbf{k}+\mathbf{q}\uparrow})\delta(\epsilon_{\mathbf{k}+\mathbf{q}\uparrow}-\mathbf{k}\downarrow-\hbar\omega_s). \tag{2.56}$$

Since usually $k_BT \gg \hbar\omega_s$ this implies that only energy-conserving processes are allowed. Furthermore, the overlap of the vacancy and occupation factors in the last equation is proportional to k_BT. For a density of states $\eta(E_F)$ one thus finds:

$$\frac{1}{T_1} = \frac{1}{T_{se}} = \frac{4\pi}{\hbar}(\eta(E_F)J)^2 k_BT, \tag{2.57}$$

which is the famous *Korringa relaxation rate.* The equation of motion then gives:

$$\frac{d}{dt}M_s = g_s\mu_B(1+\lambda\chi_e^0)[\mathbf{M}_s\times\mathbf{H}] - \frac{1}{T_{se}}\left(1-\frac{\theta}{T}\right)[M_s-\chi_sH_1], \tag{2.58}$$

where $\theta/T = \lambda^2\chi_s^0\chi_e^0$ so that θ is the Curie-Weiss temperature which occurs in the formula for the static susceptibility.

Finally, the linewidth is determined by the effective relaxation rate:

$$\left(\frac{1}{T}\right)_{eff} \equiv \left(1-\frac{\theta}{T}\right)\frac{1}{T_{se}} = \frac{4\pi}{\hbar}[\eta(E_F)J]^2 k_B(T-\theta) = a+bT \tag{2.59}$$

where $a = -(4\pi/\hbar)(\eta(E_F)J)^2\theta$ is the residual linewidth. This modification to the relaxation rate is the slowing down of relaxation near to a magnetic phase transition.

Hence, the third information we obtain is the resonance linewidth (ΔH) which gives important information about the relaxation via conduction electrons and, consequently, information about the exchange interaction and the density of states at the Fermi level.

However, this is the simplest approach one can use. In condensed-matter materials, the exchange interaction can be anisotropic ($J(\mathbf{q})$), multiple bands can play a role at the Fermi level, the conduction electron susceptibility can be enhanced etc. If the g-shift calculated from eq. 2.52 yields a Korringa rate (eq. 2.59) larger than the experimental one, then we have to consider a $\mathbf{q}$-dependent exchange interaction $J(\mathbf{q})$. On the other hand, if the calculated g-shift leads to a smaller b, then we have to consider multiple bands.

In this thesis, we will observe the first behavior. Thus, in the presence of a $\mathbf{q}$-dependence of the exchange interaction, $J_{fs}(\mathbf{q})$, and also an $e-e$ exchange enhancement, the g-shift and the thermal broadening of the linewidth may be re-written as:

$$\Delta g = J_{fs}(\mathbf{0})\ \frac{\eta\,(E_F)}{1-\alpha}\ , \tag{2.60}$$

and

$$\frac{d\,(\Delta H)}{dT} = \frac{\pi k}{g\mu_B} < J^2_{fs}(\mathbf{q}) > \eta^2\,(E_F)\ \frac{K(\alpha)}{(1-\alpha)^2}\ , \tag{2.61}$$

where $K(\alpha)$ is the Korringa exchange enhancement factor [76, 77]. The Korringa rate is a measure of the average momentum transfer $q = |\mathbf{k}_F^{out} - \mathbf{k}_F^{in}| = k_F[2(1-\cos\theta)]^{1/2}$ in the Fermi surface ($0 < q < 2k_F$). It often happens that not all the paramagnetic ions feels the same local field and therefore there is a g-value distribution. In addition, the characteristic time T_{se} can also change slightly between the magnetic moments causing a resonant line broadening. There are two types of broadening in solids: homogeneous and inhomogeneous broadening. An homogeneous ESR linewidth is inversely proportional to the so-called $spin-spin$ relaxation time, T_2 [74]. It occurs when the magnetic resonance signal results from a transition between two levels of spins which are not sharply defined, but instead, are somewhat intrinsically broadened. The main contributions to homogeneous broadening are: (1) dipolar interaction between like spins, (2) spin-lattice interaction, (3) interaction with radiation field, (4) diffusion of excitation throughout the sample, and (5) motionally narrowing fluctuations of local fields [74, 78].

On the other hand, an inhomogeneously broadened resonant line is one which consists of a spectral distribution of individual lines merged into an overall line or envelope. For instance, a distribution of local fields caused by unresolved fine and/or hyperfine structure, g-value anisotropy, strain distribution and/or crystal irregularities that exceed the natural linewidth ($2/\gamma\mathrm{T}_2$, γ is the gyromagnetic factor) will cause the spins in various parts of the sample to feel different field strengths [74, 78].

In this way the resonance will be artificially broadened in an inhomogeneous manner. In the cases of inhomogeneous broadening caused by g-value anisotropy and related strain distribution and/or crystal irregularities, the ESR linewidths are expected to increase as a function of magnetic field.

For completeness, we discuss the case where $b_{\text{calculated}} < b_{\text{measured}}$ meaning that there are multiple electron contributions (d, p, and/or f) to the conduction bands that have not been considered. In this case, the g-shift and the Korringa rate can be re-written as:

$$\Delta g = \Delta g_{fs} + \Delta g_{fd} + \Delta g_{fp} + ... = Jfs\eta s + Jfd\eta d + Jfp\eta p + ..., \tag{2.62}$$

and

$$b = \frac{\pi k_B}{g\mu_B} J_{fs}^2 \eta_s^2 + \frac{\pi k_B}{g\mu_B} J_{fd}^2 \eta_d^2 + \frac{\pi k_B}{g\mu_B} J_{fp}^2 \eta_p^2 + ..., \tag{2.63}$$

where J_{fs}, J_{fp}, J_{fd} are the exchange interactions between the Eu^{2+} $4f$ spin and the s, p, and d bands, respectively, and η_s, η_p, η_d are the densities of states for the s, p, and d bands, respectively. Depending on the interaction, the sign of J can be positive (ferromagnetic) or negative (antiferromagnetic). Therefore, the sign of Δg provides information about the interaction between the local moment and the conduction electrons.

Now we return to the Hamiltonian of Eq. 2.39 to discuss the remaining interaction terms that are responsible for fine (crystal-field) and hyperfine structures in the ESR lines. The first one can be observed in S-state ions ($S \geq 1$) due to indirect effects of the crystal field when higher order corrections in S_x, S_y, and S_z are added to the spin Hamiltonian. In this case, the crystal-field splits the excited J multiplets and transitions between these levels are possible. For example, if a local moment is in a state $|S_z\rangle$ it can relax, via the mutual spin-flip with a conduction electron, only to either $|S_z - 1\rangle$ or $|S_z + 1\rangle$. This implies a direct transfer of the dynamics magnetization, associated with the $S_z - 1 \leftrightarrow S_z$ to and from only the adjacent transitions $S_z - 1 \leftrightarrow S_z$ and $S_z + 1 \leftrightarrow S_z + 2$ as shown in Figure 2.13a.

Since the exchange interaction conserves spins there must also be scattering out from each local moment transition to the conduction electrons in order to balance the scattering in from the conduction electrons. For non-S states the separation between the fundamental and the first excited state is usually greater and the fine structure is not observed. Moreover, the resolved fine structure is commonly observed only at low temperatures. At high temperatures there is a collapse of the lines centered at the $+1/2 \leftrightarrow -1/2$ line. This collapse occurs because the local moment can relax to the lattice with rate $1/T_{S_z e}$ or to a $S_z \pm 1$ state with rate:

$$\frac{1}{T_{S_z}^{Sz\pm1}} = 2\pi[S(S+1) - S_z(S_z+1)](\eta(E_F)J)^2 k_B T, \tag{2.64}$$

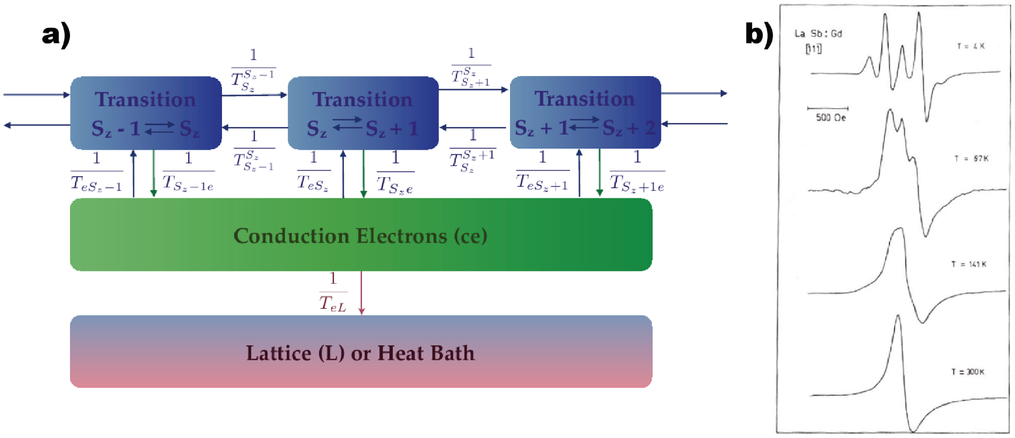
a)
b)
Transition $S_z - 1 \rightleftarrows S_z$
Transition $S_z \rightleftarrows S_z + 1$
Transition $S_z + 1 \rightleftarrows S_z + 2$
$\frac{1}{T^{S_z-1}_{S_z}}$
$\frac{1}{T^{S_z}_{S_z-1}}$
$\frac{1}{T^{S_z}_{S_z+1}}$
$\frac{1}{T^{S_z+1}_{S_z}}$
$\frac{1}{T_{eS_z-1}}$
$\frac{1}{T_{S_z-1e}}$
$\frac{1}{T_{eS_z}}$
$\frac{1}{T_{S_ze}}$
$\frac{1}{T_{eS_z+1}}$
$\frac{1}{T_{S_z+1e}}$
Conduction Electrons (ce)
$\frac{1}{T_{eL}}$
Lattice (L) or Heat Bath
La Sb : Gd
[111]
T = 4 K
500 Oe
T = 67 K
T = 141 K
T = 300 K

Figure 2.13: a) Cross-relaxation in the presence of fine-structure splitting. b) The spectrum of LaSb:Gd between 4 and 300 K. The low temperature resolved spectrum becomes progressively narrowed. Figure extracted from [79].

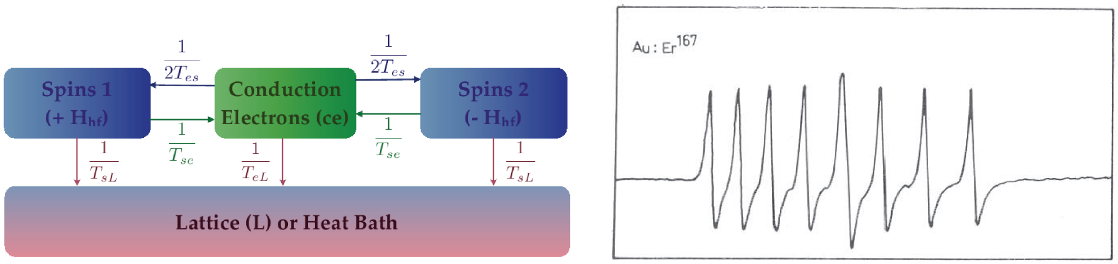
Spins 1
(+ H_{hf})
Conduction Electrons (ce)
Spins 2
(- H_{hf})
$\frac{1}{2T_{es}}$
$\frac{1}{T_{se}}$
$\frac{1}{2T_{es}}$
$\frac{1}{T_{se}}$
$\frac{1}{T_{sL}}$
$\frac{1}{T_{eL}}$
$\frac{1}{T_{sL}}$
Lattice (L) or Heat Bath
Au : Er^{167}

Figure 2.14: (left) Cross-relaxation in the presence of hyperfine splitting. (right) Spectrum of a powdered sample of 100 p.p.m. Er^{167} in Au at 1.4 K and X-Band. Figure extracted from [79].

which is proportional to the Korringa rate. As the temperature is raised the pair of transitions are narrowed. As the temperature is further raised the coupling between other lines becomes significant and the spectrum progressively narrows to a single line, as shown in Figure 2.13b).

Finally, the hyperfine coupling in the large field limit ($g\mu_B H_0 \gg A$) can be simplified to $H_{hf} \cong AS_zI_z$ and, assuming that the temperature is large compared to the nuclear Zeeman energy, the operator I_z can be replaced by one of its eigenvalues $I, I-1, ..., -I$. The cross-relaxation in the presence of hyperfine splitting is shown in Fig. 2.14a and typical ESR lines for $I = 7/2$ is shown in Fig. 2.14b.

It is worth noting that, although we have focused on electron spin resonance, the phenomena of nuclear magnetic resonance (NMR) can be understood in an analogous way. Basic NMR measurements in a metal involve the magnetic resonance field shift K (Knight shift) and the spin relaxation rate ($1/T_1$) of a given nucleus in the material:

$$K = A\chi(0,0)/\mu_B, \tag{2.65}$$

$$\frac{1}{T_1} = k_B T \left(\frac{\gamma}{mu_B}\right)^2 \sum_{\mathbf{q}} A^2(\mathbf{q})\chi''(\mathbf{q},\omega_0)/\omega 0, \tag{2.66}$$

where $A(\mathbf{q})$ is $\mathbf{q}$-dependent hyperfine coupling, $\chi''(\mathbf{q},\omega_0)$ is the imaginary part of the spin susceptibility. The latter is averaged over all wave vectors weighted by a form factor which depends on the position of the nucleus in the unit cell and may also include the effect of a transferred hyperfine interaction. In this thesis, we are going to show some of our NMR results in the ^{75}As nucleus and a systematic study will be presented elsewhere.

Chapter 3

Experimental Techniques

This chapter compiles the main experimental techniques that were employed during the course of this work: from the growth of the single crystals to the characterization by macroscopic and microscopic techniques.

3.1 Single Crystal Growth

In condensed-matter physics it is often the case that the sample quality is crucial for measuring accurate data. In fact, many macroscopic and (particularly) microscopic probes can only be effectively employed with single crystal materials. Fermi surface experiments, for example, using the de Haas-van Alphen effect (see Section 3.3.2 for more details), and many neutron and X-ray experiments are in this category. Ceramic or pressed powders, wherein the particles are randomly oriented, not only present a much higher surface to bulk ratio than do single crystals but they also present problems of intergranular composition and porosity, and prevent any meaningful measurements of anisotropy.

In this manner, our group has continuously made great efforts to synthesize high-quality single crystalline samples of intermetallic compounds. For this purpose, we employ a successful low-cost technique known as metallic-flux technique [80]. As the name indicates, the growth is performed in a metallic solvent medium (flux) that has a low melting point (such as Al, Ga, In, Sn, Pb, Sb, Bi and Zn). There are two main advantages in this technique: (1) materials can often be grown well below their melting points, and this often produces materials with fewer defects and much less thermal strain, and (2) molten metals offer a clean environment for growth, since the molten metal flux often gathers impurities which do not subsequently appear in the crystal.

On the other hand, there are also disadvantages in this technique: (1) metal flux from which the desirable compound will crystallize may not be found; (2) difficulties are encountered with some flux choices (for example, when the flux enters the crystal as an impurity). In fact, we have faced the second problem twice during this thesis: first, by choosing Sn-flux we observed a reasonable percentage of inclusions (varying from $0.1 - 1.0\,\mathrm{Atom}\,\%$) that changed the physical properties and introduced inhomogeneities; secondly, we have grown selected single crystals from self-(FeAs-) flux which does not introduce any new element in the melt but on the other hand presents stoichiometric variations from the 122 system due to the excess of FeAs in the melt. Particularly, the excess As used in a self-flux growth exposes the sample growers to an additional chemical hazard, given the need of handling a much larger amount of As during the process.

Consequently, we have focused on an innovating method to grow single crystalline samples of $\mathrm{Ba}_{1-x}\mathrm{Eu}_x\mathrm{Fe}_{2-y}\mathrm{TM}_y\mathrm{As}_2$ (TM = Mn, Co, Ni, Cu, Ru) using Indium (In) flux. Elemental (Ba, Eu), (Fe, TM) and As were added to In in the ratio (Ba, Eu):(Fe, TM):As:In= $1:2:2:25$. The materials were weighed in an argon-filled glove box, placed in alumina crucibles ($\mathrm{Al_2O_3}$) and then sealed in quartz tubes under vacuum. As $\mathrm{Al_2O_3}$ has a much larger thermal expansion than quartz, it can break the quartz upon heating. In order to avoid this, we insert quartz wool between the crucible and the tube. Moreover, quartz wool is also used on top of the crucible so it allows the melted flux to pass through it during centrifugation at the removal temperature, T_{rem}. In this manner, the resulting single crystals are kept inside the crucible while the flux is separated due to the spinning (see Fig. 3.1).

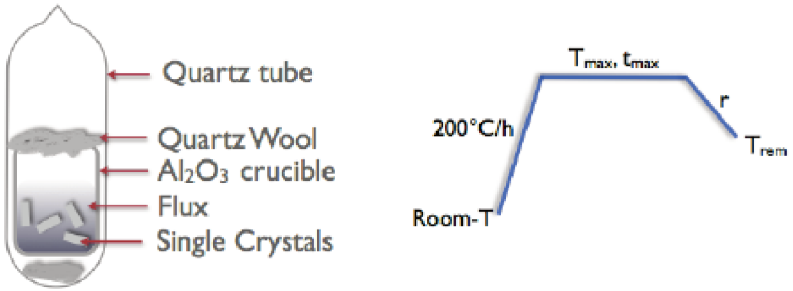

Figure 3.1: Illustration of the metallic-flux technique. (left) The elements are placed inside an alumina crucible with the flux on the top. The crucible is sealed in a quartz tube under vaccum and then (right) submitted to a thermal treatment.

We have developed different treatments for each substitution, so that inclusions were minimized. In conventional furnaces, the materials were heated up to the maximum temperature T_{max} for a time t_{max} then slowly cooled at a rate r down to the removal temperature T_{rem}. In the Eu compounds, there is a complicating factor since there are two competing phases: $\mathrm{EuFe_2As_2}$ and

$EuIn_2As_2$. As the $EuFe_2As_2$ compound is the high-temperature phase, we slowly cooled it at a rate r down to T^* where we turned off the furnace in order to lower its temperature as fast as possible until it reaches T_{rem}. The resultant crystals were shiny platelets with typical dimensions ranging from $0.5 \times 0.5 \times 0.05$ mm^3 to $3.0 \times 3.0 \times 0.05$ mm^3.

3.2 Specific Heat Measurement

The heat capacity, C, of a material is an extensive variable that measures the heat required to raise its temperature by one Kelvin. It depends on the variable which is held constant and here we concentrate in the heat capacity at constant pressure:

$$C_P = \left(\frac{đQ}{dT}\right)_P, \tag{3.1}$$

in units of J/K. In order to work with an intensive variable we compute the specific heat (in units of J/mol.K) of the material by dividing its heat capacity by the number os moles in the material.

In solids, the specific heat can provide important information about the lattice, electronic and magnetic properties. In particular, when the measurement is taken at temperatures well below the Debye temperature, c_P directly probes the electronic and magnetic energy levels of a material, and hence allows comparisons between theory and experiment.

Throughout this thesis, the heat capacity measurements were performed in a commercial Quantum Design PPMS (Physical Property Measurement System) small-mass calorimeter, shown in Fig. 3.2a. The calorimeter is a puck one inserts into the sample chamber which controls the heat added to, and removed from, a sample while monitoring the resulting change in temperature. During a measurement, a known amount of heat is applied at constant power for a fixed time, and then this heating period is followed by a cooling period of the same duration. A resistive platform heater and platform thermometer are attached to the bottom side of the calorimeter chip that works as the sample plataform, shown in Fig. 3.2b. The platform thermometer measures the temperature of the sample platform and thus the temperature of the sample. The puck thermometer is buried within the puck and it measures the temperature of the puck, which serves as the calorimeter's thermal bath. Eight delicate, thermally conducting small wires provide the electrical connection to the platform heater and platform thermometer and also provide the thermal connection and structural support for the platform. The sample is mounted to the platform by using a thin layer of N apiezon grease, which provides the required thermal contact to the platform.

A cryopump provides the necessary high-vaccum so that the thermal conductance between the sample platform and the thermal bath (puck) is totally dominated by the conductance of the wires. The basic puck configuration accommodates small, but not microscopic, samples with weight

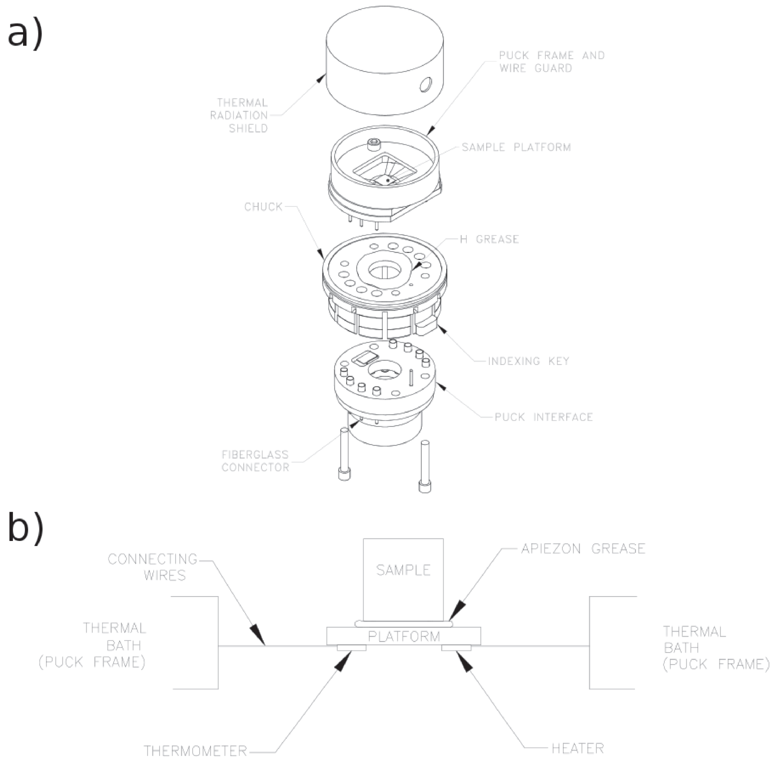
a)
PUCK FRAME AND WIRE GUARD
THERMAL RADIATION SHIELD
SAMPLE PLATFORM
CHUCK
H GREASE
INDEXING KEY
PUCK INTERFACE
FIBERGLASS CONNECTOR
b)
CONNECTING WIRES
SAMPLE
APIEZON GREASE
THERMAL BATH (PUCK FRAME)
PLATFORM
THERMAL BATH (PUCK FRAME)
THERMOMETER
HEATER

Figure 3.2: a) Calorimeter puck and b) thermal connections to sample and sample platform used in the heat capacity measurements. Figures extracted from ref. [81].

ranging from approximately 1 to 200 mg. Given the thermal characteristics of the calorimeter, this range of masses produces, for most solids, varying relaxation time constants that may be a fraction of a second at 2 K or many minutes at 300 K.

After the measurement, a quasiadiabatic thermal relaxation model is employed to convert the raw data into heat capacity estimatives by describing the temperature response of the sample platform as a function of time. As the thermal coupling between the sample and the platform is not perfect, the two-tau model simulates the effect of heat flowing between the sample platform and the sample, and the effect of heat flowing between the sample platform and puck using the following equations:

$$C_{platform}\frac{dT_p}{dt} = P(t) - K_w(T_p(t) - T_b) + K_g(T_s(t) - T_p(t)), \tag{3.2}$$

$$C_{sample}\frac{dT_s}{dt} = -K_g(T_s(t) - T_p(t)), \tag{3.3}$$

where $C_{platform}$ is the heat capacity of the sample platform, C_{sample} is the heat capacity of the sample, K_w is the thermal conductance of the supporting wires, K_g is the thermal conductance between the two due to the grease and $P(t)$ is the power applied to the heater, which is P_0 during the heating portion of the measurement and equal to zero during the cooling portion. The respective temperatures of the platform, sample and thermal bath (puck frame) are given by $T_p(t)$, $T_s(t)$ and T_s.

Using a nonlinear, least-squares fitting algorithm, the system compares the solution to the simple model to the actual measurement and the parameter values that dive the smallest fit deviation determine the heat capacity. The sensitivity of the fit deviation (χ^2) to small variations in the fitting parameters is used to estimate the standard errors for the heat capacity. A typical heat capacity measurement is shown in Fig. 3.3.

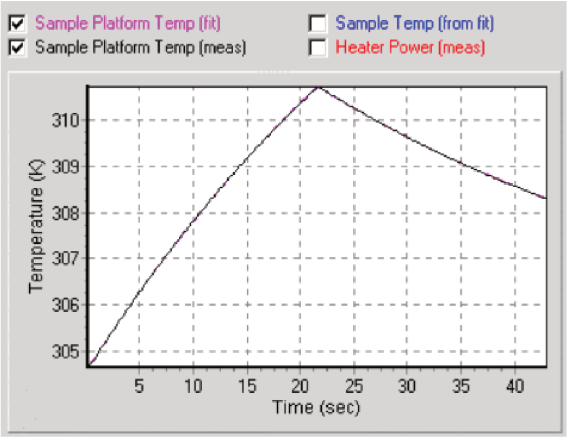

☑ Sample Platform Temp (fit)
☑ Sample Platform Temp (meas)
☐ Sample Temp (from fit)
☐ Heater Power (meas)

Figure 3.3: PPMS measurement status viewer displaying the fit plot and the measured temperature versus time.

In this thesis, heat capacity measurements were performed in both PPMS-9T and PPMS-14T systems at our laboratory in Campinas, and in a PPMS-9T at the laboratory of the University of California at Irvine in collaboration with Prof. Zachary Fisk. In the standard option, the PPMS-9T works in the temperature range $2 < T < 350$ K, and in a magnetic field range $-9 < H < 9$ T, while the PPMS-14T has a broader range of $-14 < H < 14$ T. We have also performed measurements at lower temperatures ($T = 0.3$ K) using a Helium-3 system coupled to the PPMS-9T and a diluted refrigerator coupled to the PPMS-14T.

3.3 Electrical Resistivity Measurement

Although the heat capacity measurements allow us to easily compare theory and experiments, a substantially more common measurement is the electronic transport, such as the resistivity of a material. As in the case of heat capacity, DC resistivity measurements were performed in a commercial Quantum Design PPMS (Physical Property Measurement System) puck shown in Fig. 3.4. Resistivity sample pucks have four contacts —one positive and one negative contact for current (I) and voltage (V). In this manner, current is passed through a sample via the two external current leads, and two separate voltage leads measure the potential difference across the sample. The voltmeter has a very high impedance, so the voltage leads draw very little current. Therefore, using the four-probe method to attach a sample to the puck greatly reduces the contribution of the leads and joints to the resistance (R) measurement. Furthermore, the method allows one to measure, to a high degree of certainty, both current and voltage drop across the sample, and thus calculate the resistance with Ohm's law ($R = V/I$). The current bridge has a resolution of 0.01 μA and maximum current of 5 mA. Fig. 3.4b shows four platinum wires attached to a small sample of $\mathrm{EuIn_2As_2}$ with an epoxy resin.

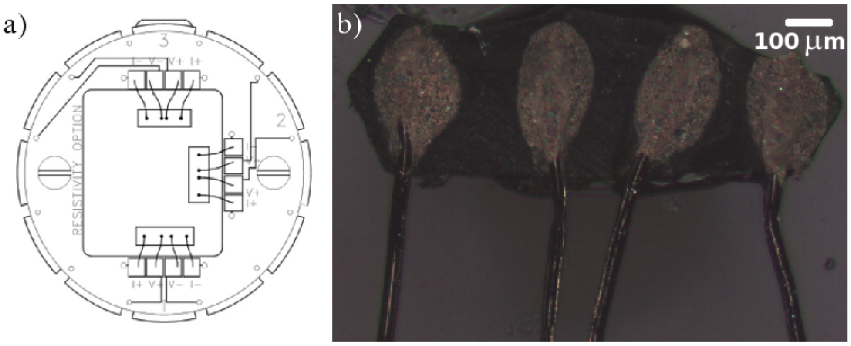

Figure 3.4: a) Resistivity sample puck with three samples mounted for four-wire resistance measurements. Figure extracted from ref. [82]. b) Photograph of a $\mathrm{EuIn_2As_2}$ single crystal with four platinum leads attached to it by an epoxy resin.

In order to remove the dependence on the geometry of the sample and to determine the resistivity of the material, we measured the distance l between the voltage leads and the cross section area A through which the current flows. In this manner, the resistivity is given by $\rho = R.(A/l)$

In this thesis, we also performed resistivity measurements using the Horizontal Rotator that allows the sample to be rotated around an axis perpendicular to the magnetic field of a longitudinal PPMS magnet.

3.3.1 Under Hydrostatic Pressure

Besides the valuable information given by resistivity measurements at ambient pressure, the pressure tuning in high quality single crystals can provide robust answers that are not affected by disorder. In this thesis, we use the standard AC four-probe method in a Quantum Design PPMS and a self-contained double-walled piston-cylinder type Be-Cu pressure cell, with a core of hardened NiCrAl alloy, that allows us to reach 30 kbar. Fig. 3.5 displays The samples and the Pb manometer were mounted on a feedthrough, which was inserted into a teflon capsule filled with Fluorinert FC-75. Pressure was generated at room temperature with an hydraulic press and then locked in.

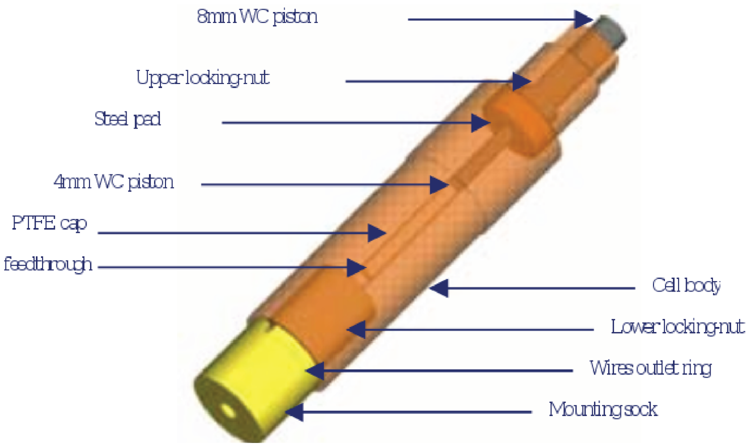

Figure 3.5: 3D modelling view of the pressure cell. Figure extracted from ref. [83].

3.3.2 At High Magnetic Fields: Quantum Oscillations

Quantum oscillation measurements are vital to characterize the electronic structure of metals, in particular complex intermetallic systems. In order to understand the origin of the quantum oscillations, let us consider a free electron gas, whose surface of constant energy is spherical, in the presence of an applied magnetic field H along the z direction. By solving the Schroedinger equation, we obtain, as in the harmonic oscillator, the quantization of energy levels that are highly degenerate:

$$E_n(k_z) = \frac{\hbar^2}{2m}k_z^2 + \left(n + \frac{1}{2}\right)\hbar\omega_c, \quad \omega_c = \frac{eB}{m}, \tag{3.4}$$

where n is a nonnegative integer, k_z takes the same values as in the absence of a magnetic field and ω_c is the angular frequency of an electron executing cyclotron motion.

Hence, the spherical surface is rearranged into a series of concentric cylinders known as Landau tubes, shown in Fig. 3.6a and electron motion is now confined to the surface of these tubes, resulting in quantized motion along cyclotron orbits:

$$\Delta E = \hbar\omega_c \quad , \quad \omega_c = \frac{eB}{m^*} = \frac{2\pi eB}{\hbar^2 \partial\Lambda/\partial\varepsilon} \tag{3.5}$$

where m^* is the effective mass, and Λ is the cross sectional area in reciprocal space of a constant energy Landau tube intersected by a plane normal to the magnetic field B. From equation 3.5, the condition for Landau tube area quantization is yielded as:

$$\Lambda_r = (r + \frac{1}{2})\frac{2\pi eB}{\hbar} \tag{3.6}$$

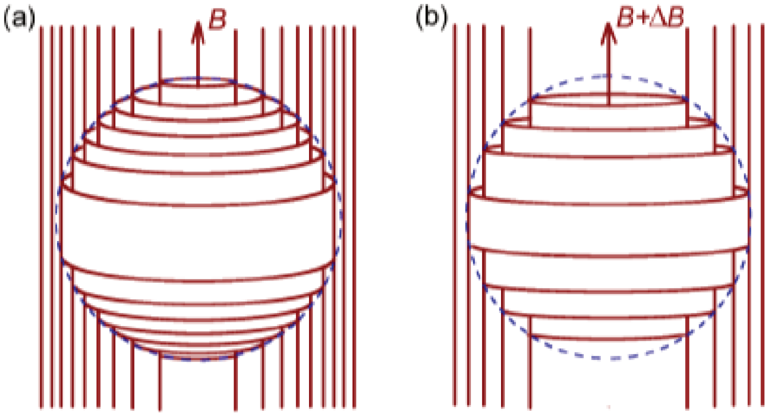

Figure 3.6: (a) Schematic of Landau levels for spherical Fermi surface as in a free electron has in a magnetic field H. (b) Schematic of Landau levels, when the applied magnetic field is increased to $H + \Delta H$. The Landau levels increase in area with an increase in magnetic field, causing fewer of them to be accomodated within the Fermi surface as the magnetic field is increased. Figure extracted from [84].

When the magnetic field is increased, each Landau tube expands in area, causing its height accommodated within the Fermi surface (FS) to shrink, until it spans the extremity of the Fermi surface (with extremal area $\Lambda = A$) just before it exits the FS entirely. As each Landau tube exits the FS, there is a sudden discontinuous change in the total energy of the occupied states, and the electronic properties related to the density of states oscillates with a frequency:

$$f = \frac{\phi_0 A}{2\pi^2} = 2\frac{A}{A_{BZ}}\frac{\phi_0}{ab}, \tag{3.7}$$

where $\phi_0 = h/e$ is the magnetic flux quantum, A_{BZ} is the area of the Brillouin zone in reciprocal space, and a and b are the unit cell dimensions in real space assuming a tetragonal lattice. The quantum oscillations in magnetization are referred to as *de Haas-van Alphen* oscillations, and the quantum oscillations in electrical transport are referred to as *Shubnikov de Haas* (SdH) oscillations.

In this thesis, we will discuss the SdH oscillations in $BaFe_2As_2$ and $EuFe_2As_2$ measured at the National High Magnetic Field Laboratory (NHMFL), in Tallahassee - USA. Measurements were performed in two resistive magnets: 35 T, 32 mm bore, top-loading He3 cryostat (Cell 12) and 45 T, 32 mm bore, top-loading He3 cryostat (Cell 15: Hydrid). As we will see, quantum oscillations can provide important information about the Fermi surface geometry and effective masses.

3.4 Magnetic Susceptibility Measurement

Magnetic measurements on our single crystals were performed either with a commercial MPMS magnetometer at Campinas (MPMS-7T, Quantum Design, Inc.), or with a commercial VSM-MPMS magnetometer at Irvine. The first one operates in the temperature range from 2 K to 400 K with external fields up to ±7 T, and the second one operates in the temperature range from 1.8 K to 400 K. Corrections for the sample holder and the core diamagnetism were applied to the data.

The MPMS sytems have a superconducting magnet to generate large magnetic fields, a superconducting detection coil which couples inductively to the sample, a Superconducting QUantum Interference Device (SQUID) connected to the detection coil with superconducting wires and a superconducting magnetic shield surrounding the SQUID (see Fig. 3.7).

Sample masses of about 1 mg to 10 mg were loaded into 16-cm transparent straws or quartz tubes. The MPMS magnetometer then allowed the sample to move through the system of superconducting coils (see Fig. 3.8) in order to change the induction field B ($B = H + 4\pi M$) within the pickup coils, and thereby changes the induced current flowing in the coils. Since a closed superconducting loop is formed by the detection coils, the connecting wires, and the SQUID input coil, any change of magnetic flux in the detection coils produces a proportional change in the persistent current in the detection circuit. Once the SQUID functions as a highly linear current-to-voltage converter, the current variations in the detection coils produce corresponding variations in the SQUID output voltage,s which are proportional to the magnetic moment of the sample. A small piece of palladium with known mass and magnetic susceptibility is used to fully calibrate the system. The units of magnetic moment are emu (in cgs units) and A.m^2 (in SI units). The MPMS

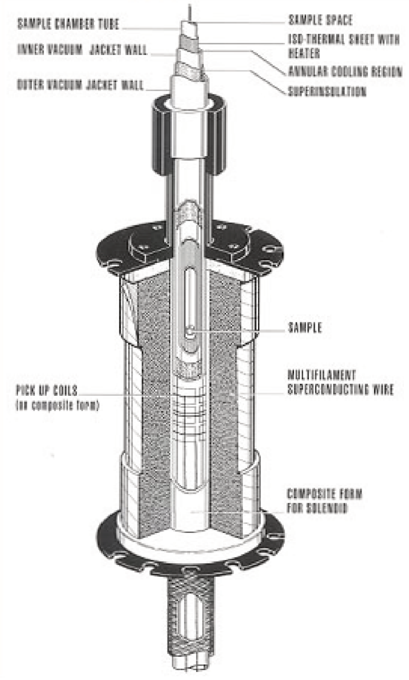
SAMPLE CHAMBER TUBE
INNER VACUUM JACKET WALL
OUTER VACUUM JACKET WALL
SAMPLE SPACE
ISO-THERMAL SHEET WITH HEATER
ANNULAR COOLING REGION
SUPERINSULATION
SAMPLE
PICK UP COILS (in composite form)
MULTIFILAMENT SUPERCONDUCTING WIRE
COMPOSITE FORM FOR SOLENOID

Figure 3.7: Schematics of the MPMS magnetometer. Figure extracted from [85].

reported value of the magnetic moment is divided by the number of moles in the sample and by the applied magnetic field (H) in order to obtain the magnetic susceptibility χ.

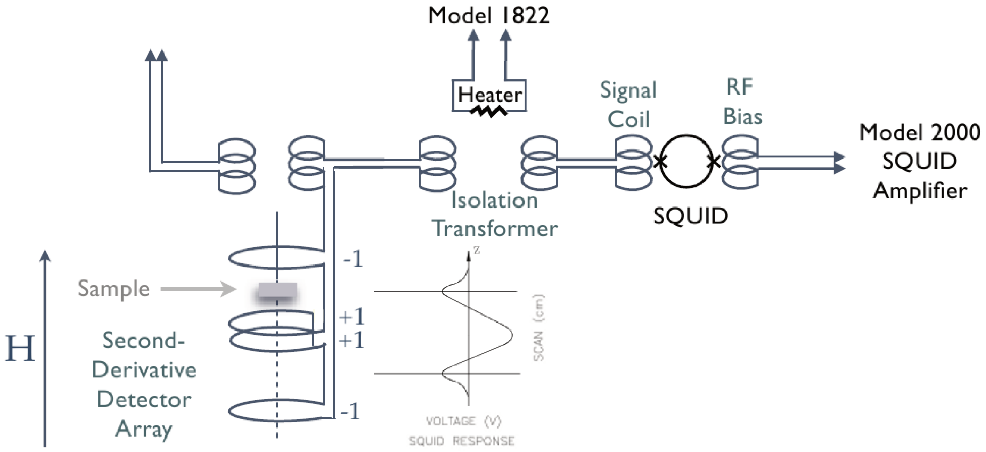
Model 1822
Heater
Signal Coil
RF Bias
Model 2000 SQUID Amplifier
Isolation Transformer
SQUID
Sample
H
Second-Derivative Detector Array
-1
+1
+1
-1
z
SCAN (cm)
VOLTAGE (V)
SQUID RESPONSE

Figure 3.8: Schematics of the MPMS magnetometer coils.

The VSM option also has a SQUID detection system, but the induced signal is generated by oscillating the sample in the magnetic field within the detection coils, as shown in Fig. 3.9. A

DC signal controls the sample position and an AC signal determines the vibration amplitude and frequency. The default vibration frequency is 414 Hz and the vibration amplitude is usually set to 2 mm. The VSM magnetometer can reach a sensibility of $\sim 10^{-8}$ emu.

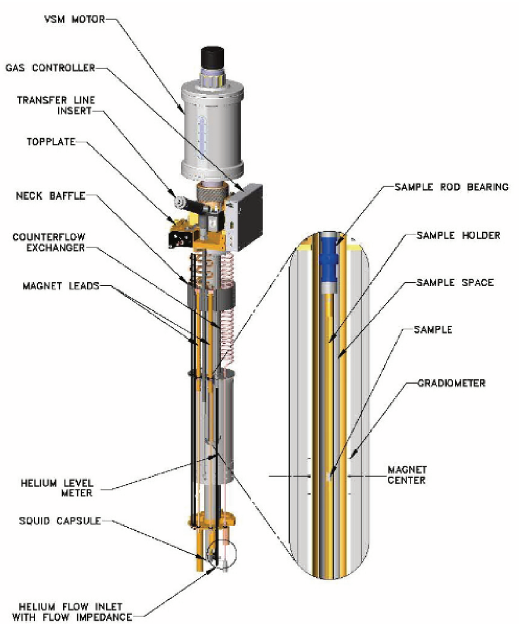
VSM MOTOR
GAS CONTROLLER
TRANSFER LINE INSERT
TOPPLATE
NECK BAFFLE
COUNTERFLOW EXCHANGER
MAGNET LEADS
HELIUM LEVEL METER
SQUID CAPSULE
HELIUM FLOW INLET WITH FLOW IMPEDANCE
SAMPLE ROD BEARING
SAMPLE HOLDER
SAMPLE SPACE
SAMPLE
GRADIOMETER
MAGNET CENTER

Figure 3.9: Schematics of the MPMS SQUID VSM probe.

3.5 X-Ray Absorption Fine Structure Spectroscopy: XANES and EXAFS

Extended x-ray absorption fine structure (EXAFS) and X-ray absorption near edge structure (XANES) spectroscopies can provide valuable element-specific structural information (such as bond lenghts, coordination number, species of the neighbors etc) and electronic ground state information (such as oxidation state, coordination chemistry, bond angles, etc), respectively [86]. In order to understand these phenomena, we note that X-ray absorption in the photon range up to 40 keV is dominated by photoelectron absorption in which the photon is completely absorbed, transferring its energy to excite an electron in a tightly bound quantum core level (such as the $1s$ or $2p$ level) and leaving a core hole in the atom. The absorption edge corresponds to an x-ray photon having enough energy to free a bound electron in the atom. We will treat the case in which the electron is in the most tightly bound $n = 1$ shell edge, called K-edge. After the absorption, the final-state photoelectron can be seen as an expanding spherical wave that is modified to first order by a single scattering (EXAFS) or by multiple scattering (XANES) from each surrounding atom. In this manner, the result is the superposition of the outgoing and scattering waves that create constructive or destructive interference depending on the distances and wavelength. Scanning the wavelength provides an interferogram of a distance distribution in the form of oscillations after the absorption edge shown in Fig. 3.10.

In the study of x-ray absorption, the basic physical quantity that is measured is the X-ray absorption coefficient ($\mu(E)$), which gives the probability that x-rays will be absorbed as a function of the photon energy E according to Beer's Law:

$$I = I_0 \exp^{-\mu(E)t}, \tag{3.8}$$

where I_0 is the x-ray intensity incident on our sample, t is the sample thickness and I is the intensity transmitted through the sample.

When the oscillations are well above the absorption edge we define the EXAFS fine-structure function $\chi(E)$:

$$\chi(E) = \frac{\mu(E) - \mu_0(E)}{\Delta\mu_0(E)}, \tag{3.9}$$

where $\mu_0(E)$ is a smooth background function representing the absorption of an isolated atom or any instrumental background, and $\Delta\mu_0(E)$ is the measured jump in the absorption at the threshold energy E_0. Usually, the EXAFS is analyzed as $\chi(k)$ in terms of the wave vector $k = \sqrt(2m(E - E_0)/\hbar^2)$. As the EXAFS decays quickly with k, in order to emphasize the oscillations $\chi(k)$ is often multiplied by a power of k, typically k^2. On the other hand, the normalized $\mu(E)$ is useful when the oscillations are near the absorption edge in XANES analysis.

The acessibility of EXAFS measurements was greatly enhanced by the availability of synchrotron radiation sources of x-rays due to its higher intensity in a continuum of energy. In this thesis, temperature-dependent EXAFS measurements at the As K edge ($E = 11865$ eV) in transmission mode were performed at ambient pressure in the XAFS-2 beamline at the Brazilian Synchrotron Laboratory (LNLS). The samples were placed into a closed-cycle Joule-Thompson He circuit, yielding a base temperature of ~ 1.7 K. The samples were mounted into a Be dome filled with He gas to account for proper heat exchange and temperature homogeneity. Temperature stability was better than 0.1 K. An Au foil was used for energy calibration. Pressure-dependent EXAFS measurements at ambient temperature were performed with dispersive optics in the DXAS beamline of LNLS using a diamond anvil cell. The samples were loaded into a hole of an iconel gasket with diameter of ~ 200 μm. Ruby spheres of ~ 40 μm diameter were also loaded into the cell. An admixture of methanol, ethanol, and water in the proportion $16 : 3 : 1$ was used as

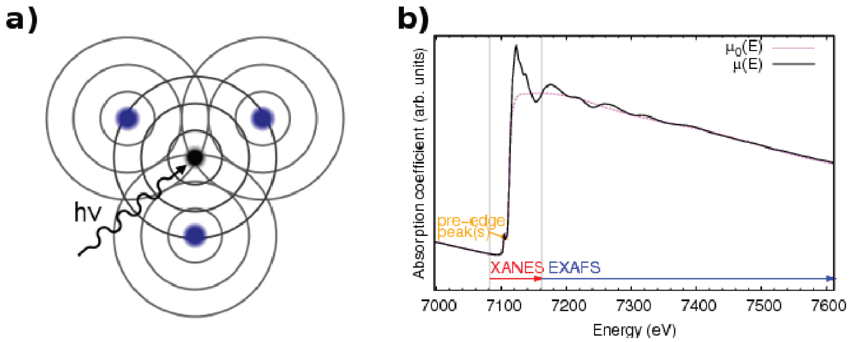

Figure 3.10: a) Pictorial view of the photoelectron interference effect. b) XAFS spectrum of a Fe_2O_3 model compound (crystalline powder) at the Fe K-edge ($E_0 = 7112$ eV).The XANES region is more sensitive to the electronic structure and the symmetry, while the EXAFS region gives more information on bond distances, coordination numbers and local disorder.

pressure-transmitting media. The applied pressures were optically measured offline by the position of the ruby fluorescence doublet. These lines present no observable broadening with increasing pressures over the whole investigated pressure interval.

The raw EXAFS measurements were preprocessed to obtain $\chi(k)$ by conventional methods using the software ATHENA [62]. Theoretical signals for atomic shells were derived using the FEFF8 code, taking the reported tetragonal crystal structure of $BaFe_2As_2$ at 175 K as the initial model. The fits were performed in real space by optimizing the Fourier transform of $k^2\chi(k)$ using the IFEFFIT program, running under the ARTEMIS graphical platform. For the temperature-dependent measurements at the As K edge, fits of the Fe-As distance were confined to the k range of $3 < k < 13$ Å and to R range of $1 < R < 3$ Å, while for the pressure-dependent data the useful k range was significantly shorter $2.5 < k < 6.5$ Å^{-1}, and the employed R range was $1.2 < R < 4.2$ Å.

Furthermore, room temperature XANES measurements were performed in the XAFS-2 beamline at LNLS. Crystals with thickness of a few microns along the c direction were selected. Spectra were measured with a 0.2 eV step width. At least two spectra were collected for each measured sample, in order to check for reproducibility of the spectral features and to improve the statistics. The edge-step normalization of the data was performed after a linear pre-edge subtraction and the regression of a quadratic polynomial beyond the edge, using the software ATHENA. The energy calibration was performed for each spectrum by simultaneously measuring and aligning the K absorption edge of a standard Fe metal foil. *Ab initio* calculations for the XANES spectra were obtained using the FEFF8 code taking the reported tetragonal crystal structure of $BaFe_2As_2$ at 297 K as the initial model. We adopted the Hedin-Lundqvist exchange potential with an imag-

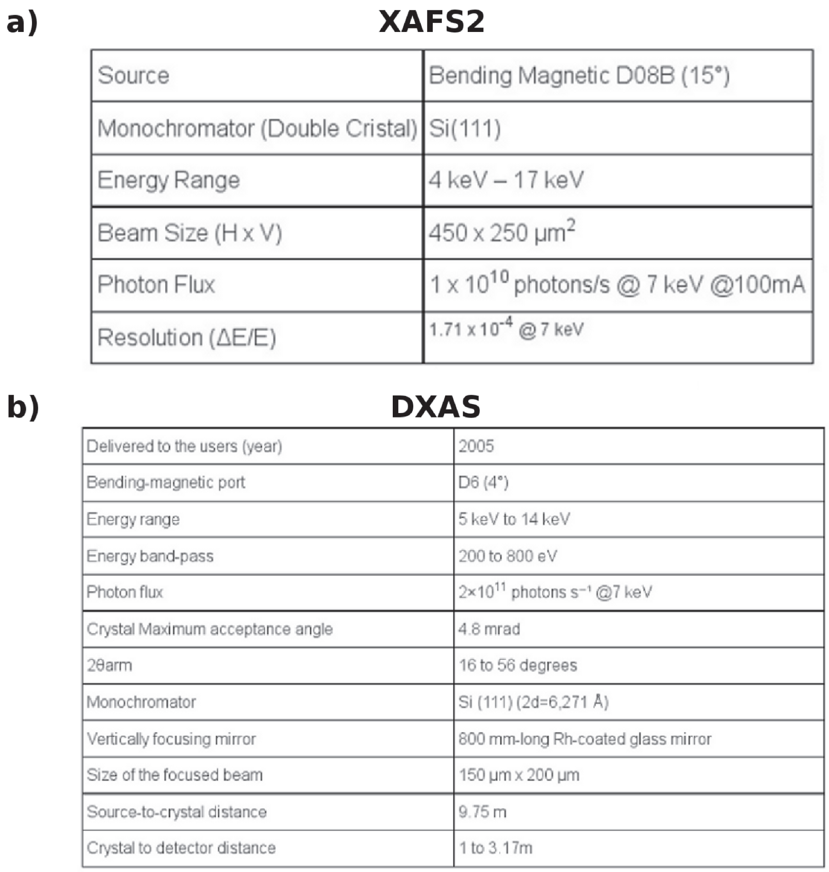

a) **XAFS2**

Source	Bending Magnetic D08B (15°)
Monochromator (Double Cristal)	Si(111)
Energy Range	4 keV – 17 keV
Beam Size (H x V)	450 x 250 μm^2
Photon Flux	1 x 10^{10} photons/s @ 7 keV @100mA
Resolution (ΔE/E)	1.71 x 10^{-4} @ 7 keV

b) **DXAS**

Delivered to the users (year)	2005
Bending-magnetic port	D6 (4°)
Energy range	5 keV to 14 keV
Energy band-pass	200 to 800 eV
Photon flux	2×10^{11} photons s^{-1} @7 keV
Crystal Maximum acceptance angle	4.8 mrad
2θarm	16 to 56 degrees
Monochromator	Si (111) (2d=6,271 Å)
Vertically focusing mirror	800 mm-long Rh-coated glass mirror
Size of the focused beam	150 μm x 200 μm
Source-to-crystal distance	9.75 m
Crystal to detector distance	1 to 3.17m

Figure 3.11: Beamline specification at the Brazilian Synchrotron Laboratory (LNLS) a) XAFS2 and b) DXAS.

inary part of 0.7 eV to account for the experimental broadening and a Debye-Waller factor of $\sigma^2 = 0.00465$ Å^2. The atomic potential was calculated self consistently using a cluster of up to 32 atoms within a radius 5.5 Å. The full multiple scattering XNES calculations converges for a cluster of 154 atoms within the radius 9.0 Å. A rigid shift of 2.8 eV to lower energies was applied to all calculated XANES spectra to match with the experimental data. This shift has no influence on the relative changes of calculated spectral features under the Co and K substitutions that guide our main conclusions.

3.6 Electron Spin Resonance Measurement

A typical experimental setup to observe electron spin resonance is shown in Fig. 3.12a. A microwave bridge (Fig. 3.12b) generates an electromagnetic wave of fixed frequency[1] that propagates through a waveguide to the metallic (retangular or cylindrical) resonant cavity which amplifies weak signals from the sample. A consequence of resonance is that there will be a standing wave inside the cavity with their electric and magnetic fields components exactly out of phase (see Fig. 3.12c). It is possible to couple the microwave in the waveguide with the microwave in the cavity via a coupling hole called iris, shown in Fig. 3.12d. If we place a thin copper sheet perpendicular to the waveguide axis and then cut a slot parallel to the short dimension, an inductive iris is formed. The slot width controls the voltage reflection coefficient Γ at the iris, defined as the ratio of the amplitude of the incident electric field (E_1) that enters the cavity and the amplitude of the reflected electric field (E_2) from the cavity. This control is accomplished by carefully matching or transforming the impedances of the cavity and the waveguide. There is also an iris screw in front of the iris that acts as a tuner device that reflects the microwaves, and thereby alter the impedance match.

Once the cavity is critically coupled, a magnet generates a static magnetic field in order to lift the Zeeman degeneracy. The magnetic field then sweeps in the range $0 \leq H_0 \leq 2$ T until the spin resonance condition is achieved and, consequently, the microwave is absorbed by the sample. Reflected microwaves are directed to the microwave bridge, where a Schottky barrier diode converts the microwave power into electric current. This type of spectrometer is called reflection spectrometer since it measures the amount of radiation reflected back from the cavity, and not the radiation transmitted through the sample.

When the sample absorbs the microwave energy, the coupling changes because the absorbing sample changes the impedance of the cavity and therefore microwave will be reflected back to the bridge, resulting in an ESR signal. In order to enhance the spectrometer sensibility, a technique known as phase sensitive (lock-in) detection is used. The d.c. magnetic field strength seen by the sample is modulated sinusoidally by a small amplitude field modulation usually at frequencies of 100 kHz. The resultant weak signal, contaminated by noise, is amplified and phase-detected relative to the modulating signal that rejects all frequencies but 100 kHz. The output signal from the lock-in detector is proportional to the change in the absorption between the modulation amplitude, and for sufficiently small amplitudes the output signal is proportional to the first derivative of the lineshape. The advantages of this detection scheme include less noise from the detection diode and the elimination of baseline instabilities due to the drift in d.c. electronics.

---

[1] There are five microwave bridges commonly available: L-Band ($\nu = 1.1$ GHz), S-Band ($\nu = 3.0$ GHz), X-Band ($\nu = 9.5$ GHz), Q-Band ($\nu = 34$ GHz), and W-Band ($\nu = 94$ GHz)

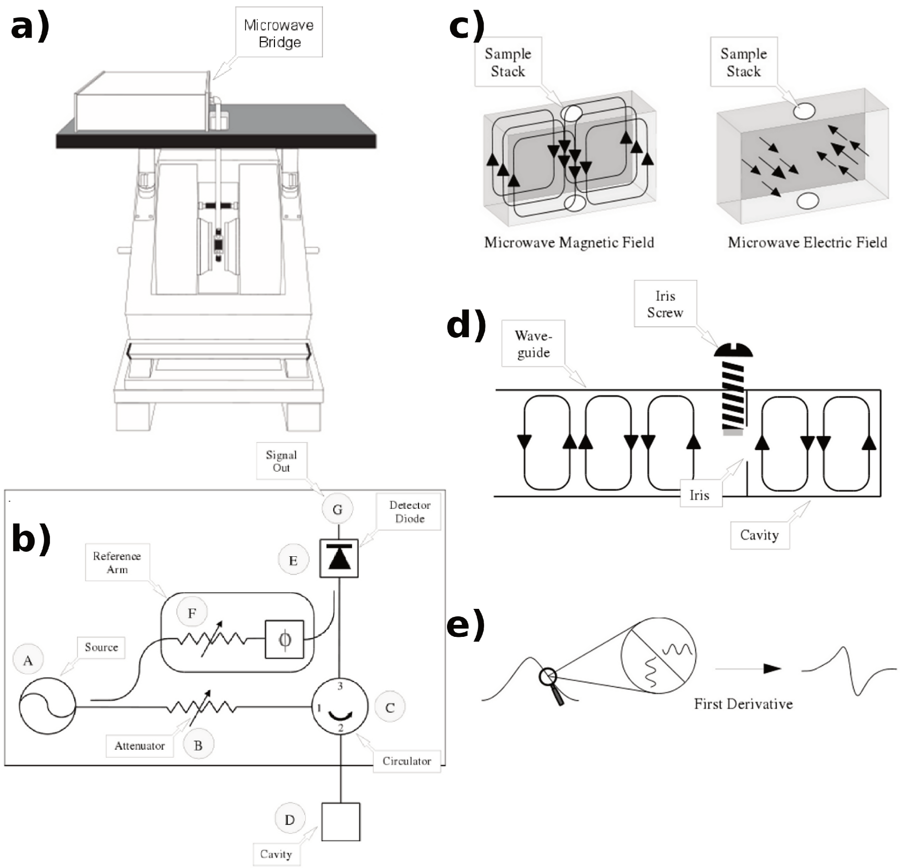
a)
Microwave Bridge
c)
Sample Stack
Sample Stack
Microwave Magnetic Field
Microwave Electric Field
d)
Iris Screw
Wave-guide
Iris
Cavity
b)
Signal Out
G
Detector Diode
E
Reference Arm
F
ϕ
Source
A
3
1
2
C
Attenuator
B
Circulator
D
Cavity
e)
First Derivative

Figure 3.12: a) The general outlay of an ESR spectrometer. b) Block diagram of a microwave bridge. c) Magnetic and electric field patterns in a standard ESR cavity. d) The matching of a microwave cavity to waveguide. e) Field modulation and phase sensitive detection. Figure extracted from ref. [87].

In this thesis, the ESR data were taken in a BRUKER ELEXSYS-500 spectrometer, as shown in Fig. 3.12, equipped with a rectangular cavity TE_{102}, a microwave bridge in the X-band region ($\nu \sim 9.4$ GHz) and a continuous He gas-flow cryostat that reaches temperatures from 300 K to 4.2 K.

Chapter 4

Synthesis and Macroscopic Properties of 122 single crystals

In this chapter the experimental results concerning the synthesis and characterization of our samples are presented. The efforts of our group in synthesizing samples using the In-flux method culminated in high-quality 122 single crystals revealed by macroscopic properties and nuclear magnetic resonance (NMR) measurements. Furthermore, we will discuss the data for optimally doped Ba122 compounds $\mathrm{BaFe}_{2-y}\mathrm{TM}_y\mathrm{As}_2$ (TM = Co, Cu, Ni) and also Eu-substituted compounds $\mathrm{Ba}_{1-x}\mathrm{Eu}_x\mathrm{Fe}_{2-y}\mathrm{Co}_y\mathrm{As}_2$ under hydrostatic pressure to investigate pair-breaking mechanisms.

4.1 Single Crystal Growth

We start our investigation with the pure $\mathrm{BaFe_2As_2}$ single crystal grown by the In-flux method. A photograph of one of the largest crystals obtained by this method is shown in Fig. 4.1a. The crystal structure was characterized by x-ray powder diffraction and submitted to elemental analysis using a commercial Energy Dispersive Spectroscopy (EDS) microprobe (Fig. 4.1b).

High resolution synchrotron X-ray diffraction measurements were performed at the XPD beamline of the Brazilian Synchrotron Light Laboratory (LNLS) with $\lambda = 1.23984$ Å. The sample was placed in the cold finger of a closed-cycle He cryostat, which was mounted in the Eurelian circle of a commercial $4+2$ circle diffractometer. A Ge(111) analyzer crystal was used in the 2θ arm to improve angular resolution of the diffracted beam. Figure 4.2a shows $\theta - 2\theta$ scans at the vicinity of the (2212) reflection of the tetragonal structure (space group $I4/mmm$). A splitting of this reflection on cooling below 139 K is observed, consistent with the emergence of the orthorrombic phase (space group $Fmmm$). A small ~ 4 K coexistence of tetragonal and orthorhombic reflec-

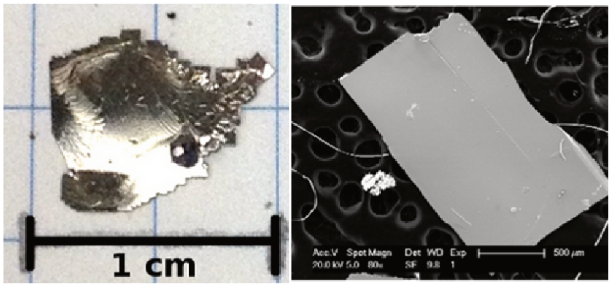

Figure 4.1: (left) Photograph of one of the largest pure single crystals grown by the In-flux technique. (right) EDS image of a Eu-substituted single crystal grown by the In-flux technique.

tions is observed. Interestingly, this coexistence is also observed by NMR experiments which reveal the appearance of a magnetic orthorhombic line below 139 K together with the decrease of the tetragonal paramagnetic line. At 134 K, no paramagnetic resonance is observed and long range SDW order is fully established.

Figure 4.2b shows the temperature evolution of the a, b and c lattice parameters, obtained from the analysis of the diffraction signal shown in Figure 4.2a, and also from the (006) reflection (not shown). Although small, one can observe a discontinuous jump in the cell volume along the transition, as shown in Figure 4.2c. Although this is suggestive of a first order transition, no latent heat was observed in the specific heat.

Figure 4.3 shows the temperature dependence of in-plane resistivity ρ_{ab} for pure $BaFe_2As_2$ crystals. The crystals grown by In-flux present a sharp feature at $T_0 \simeq 139$ K as determined by the peak in the derivative $d\rho_{ab}/dT$ and, contrarily to what happens to tin-flux grown (TFG) samples, the resistivity drops monotonically with decreasing temperature below T_0. It is worth mentioning that our In-flux samples displayed residual resistivity ratios (RRR $= (\rho_{300\,K} - \rho_{2\,K})/\rho_{2\,K}$) ranging from 6 to 8. This is in accordance with the behavior described by the samples grown by self-flux [88] as well as by the polycrystalline one [89]. Besides, the residual resistivity was found to be typically $\rho_0 \approx 0.1$ mΩ-cm for the In-flux grown (IFG) samples. This value is of the same order of those previously reported for self-flux grown (SFG) samples [90, 91, 92].

In Fig. 4.3, one can clearly see that the TFG crystal is an exception and does not follow this behavior. On decreasing temperature, the resistivity crosses 139 K with no special feature, and there is a broad increase rather than decrease in resistivity around 85 K. This is indicative of Sn incorporation as reported in Ref. [93]. The fact that the IFG samples show the same behavior as SFG indicates that In is not being incorporated in the sample. EDS experiments also show that there is no detectable In in our IFG single crystals (not shown).

Additionally, Nuclear Magnetic Resonance (NMR) and Nuclear Quadrupolar Resonance (NQR)

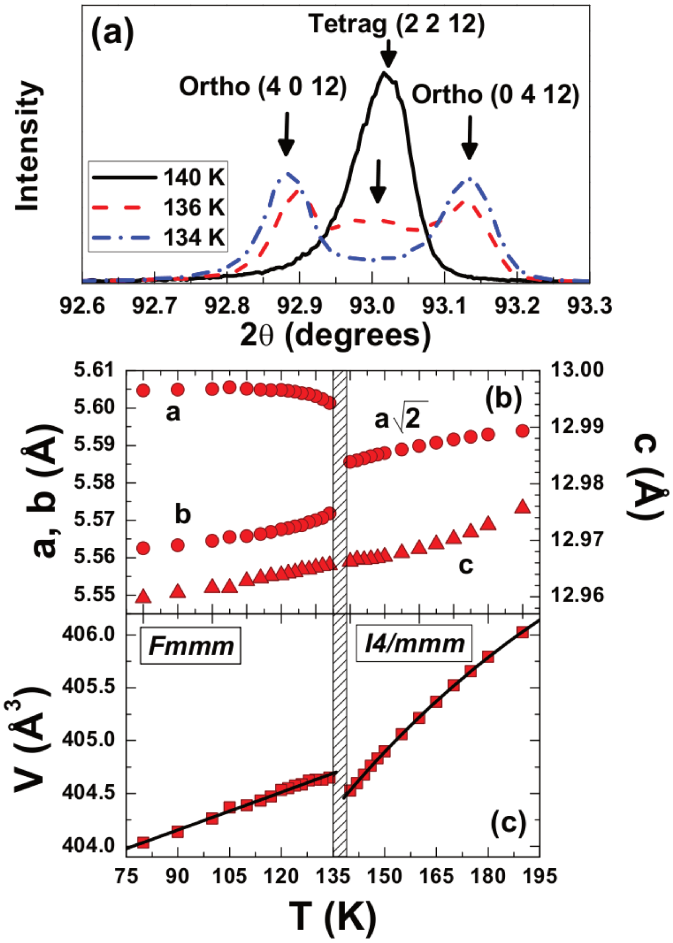

Figure 4.2: High resolution synchrotron X-ray diffraction of an IFG $BaFe_2As_2$ single crystal. (a) Radial $(\theta - 2\theta)$ scans around the (2212) tetragonal reflection. (b) Temperature dependence of a, b and c lattice parameters. (c) Temperature dependence of unit cell volume.

are powerful techniques to understand the local structural and electronic environment in a lattice [94, 95, 96, 97]. As such, ^{75}As NMR experiments were carried out in order to verify the doping effects and sample quality. NMR lineshapes are usually affected by disorder and inhomogeneity, and the linewidth is a great local probe of these effects. In other words, the structure of the spectra illustrates the local environment of the ^{75}As sites. Fig. 4.4 shows the ^{75}As NMR signal for single crystals grown by In and Sn fluxes at 150 K and $H \perp c$. The central line corresponds to the $(1/2 \leftrightarrow -1/2)$ transition, and the satellites are $(\pm 3/2 \leftrightarrow \pm 1/2)$ transitions split by quadrupolar effects [98, 97]. The IFG sample shows a very narrow (5 kHz) central linewidth with no other peaks than the two satellites, whereas the TFG sample displays a broad central line with multiple

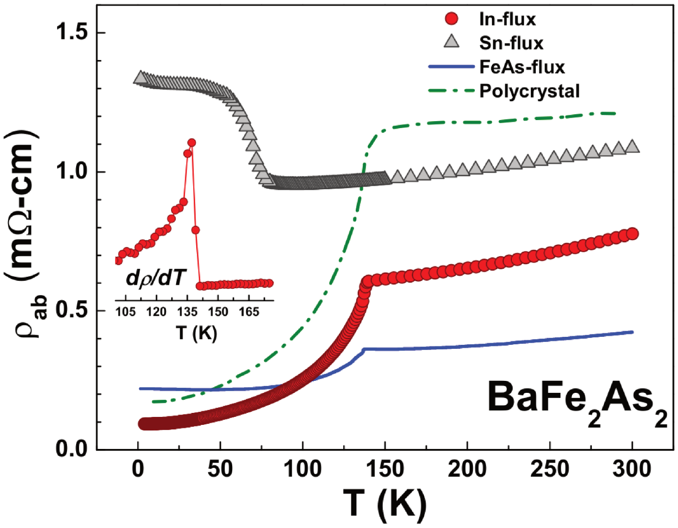

Figure 4.3: In-plane resistivity as a function of temperature for $BaFe_2As_2$ single crystals grown by In- and Sn-flux. For comparison, we also show the resistivity of the self-flux [88] and polycrystalline [89] samples.

peaks. Broad lines and multiple peaks are signatures of local internal magnetic field distribution on top of possible As site distribution, indicative of low crystallographic quality. Previously reported values of the NMR linewidth for SFG and TFG crystals were similar or even larger than ours [98, 99, 100]. Furthermore, the $BaFe_2As_2$ samples from references [99, 100] do display several peaks for the central transition. These results demonstrate microscopically that our IFG samples have equal or higher quality and homogeneity than SFG and TFG samples, and are examples of improvement for yielding Fe-arsenide compounds.

In order to evaluate the efficiency of the herein proposed In-flux method for growing Ba122 compounds, we have also explored the synthesis of doped $Ba(Fe_{1-x}M_x)_2As_2$ (M = Co, Cu, Ni and Ru) single crystals. Although we have produced a wide range of chemical substitutions for Co doping, in the following we will focus on the optimally doped samples, the superconducting ones with maximum T_c, and with the magnetic SDW state completely suppressed, for M = Cu, Ni and Ru.

Figure 4.5 shows the temperature dependence of the in-plane resistivity for different M-doped Ba122 compounds. Fig.4.5a) demonstrates that the alternative In-flux route also yields bulk superconducting samples for Co, Cu, Ni and Ru-doping, in accordance with other reports for samples grown by self- and Sn-flux techniques [101, 102, 103, 104, 105, 106, 107, 108, 109]. A noteworthy improvement over the SFG technique is the overall higher maximum T_c. Except for Ru, the IFG crystals showed greater maximum T_c than those found for the corresponding SFG samples.

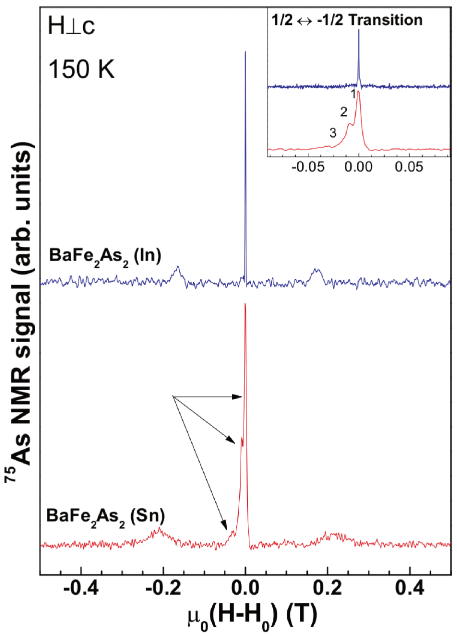

Figure 4.4: ^{75}As NMR signal for $BaFe_2As_2$ single crystals grown by In- and Sn-flux in the paramagnetic (tetragonal) phase.

Furthermore, the residual resistivity ρ_0 defined at T_c, ranges within 0.2–1.0 mΩ-cm, which are equal or smaller than those reported previously for similar samples [101, 102, 103, 104, 105]. We acknowledge that the recipe for growing Ru-substituted compounds is not yet fully optimized due to the reduced size of the obtained crystals.

Nonetheless, despite the case for Ru doping, it is plausible to assume that the IFG samples display higher critical temperatures because they present a reduced number of defects which are non-magnetic pair-breaking centers. Therefore, we strongly believe that the IFG samples are prone to less significant interference of defects and inhomogeneity effects on their intrinsic physical properties, thus being more suitable for microscopic investigations.

Let us now turn our attention to the particular case of Co-doped $BaFe_2As_2$, which generated the largest doped IFG single crystals so far. Based on thermodynamic data such as those in Fig. 4.5b), we constructed the phase diagram presented in Fig. 4.6.

Although the $T-x$ phase diagram presented in Fig. 4.6 for our Co-doped Ba122 is qualitatively similar to previous one [109] it is worth emphasizing that the maximum T_c= 26 K obtained is, to the best of our knowledge, the highest value reached up to now.

Table 4.1 shows the parameters for the pure compound and for different dopants (Co, Cu, Ni and Ru). We also show the parameters for Eu substituted samples that will be discussed in detail

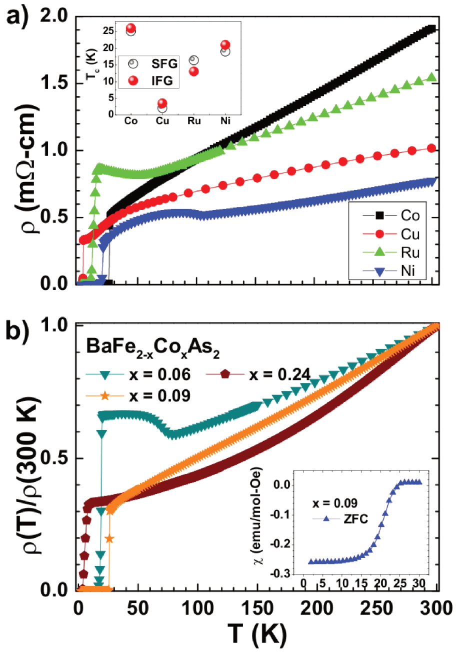

Figure 4.5: **a)** In-plane electrical resistivity as a function of temperature for $Ba(Fe_{1-x}M_x)_2As_2$ single crystals grown by In flux (M = Co, Cu, Ni and Ru). The chosen samples presented the highest T_c within the obtained batches. The inset shows the maximum T_c achieved for self and In-flux grown crystals for different dopants [109, 106, 107, 108]; **(b)** In-plane electrical resistivity as a function of temperature for $Ba(Fe_{1-x}Co_x)_2As_2$ IFG single crystals ($x = 0.03$, 0.045 and 0.12). The inset shows field cooled (FC) and zero-field cooled (ZFC) magnetic susceptibility measurements for the optimally doped sample ($x = 0.09$).

in sections 4.2.1.

4.2 Macroscopic characterization

4.2.1 Electrical Resistivity Measurements Under Hydrostatic Pressure

With high quality single crystals in hand, the study of pressure tuning in these samples can provide robust answers about the superconducting state which are not affected by disorder.

It is well known that hydrostatic pressure tends to decrease T_{SDW} in the undoped or slightly doped compound. Moreover, T_c increases with low pressure for underdoped FeAs-pnictides, remains approximately constant for optimal doping, and decreases in the overdoped range. Remarkably, there is a symmetry of the superconducting and magnetic phase diagram with respect to the

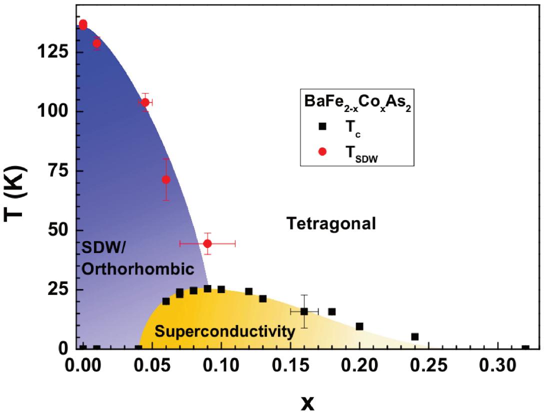

Figure 4.6: $T-x$ phase diagram for IFG Ba(Fe$_{1-x}$Co$_x$)$_2$As$_2$ single crystals. The error bars represent variations in the doping levels x and T_c amongst different batches of same nominal Co content.

substitution with K, Ru, Co, Ni, and Cu, consistent with the scenario in which these substitutions act as chemical pressure instead of acting like effective doping in the suppression of the SDW magnetic phase.

However, not only we must suppress the SDW magnetic phase, but also we have to weaken possible pair-breaking mechanisms. In this sense, the substitution of Fe by local moments (like Cu, Mn and Cr) would act as such mechanism, despite its effectiveness in suppressing the SDW magnetic phase. This scenario is perfectly consistent with the fact that SC does not emerge in BaFe$_2$As$_2$ with Mn and Cr substitutions and also that SC in BaFe$_{2-x}$Cu$_x$As$_2$ has a maximum reported T$_c$ of only $\sim$ 2 K in a narrow range of concentration [106]. In fact, inelastic neutron scattering measurements show that Cu substitution has enhanced impurity scattering and split-band behavior [110]. Surprisingly, an increase of T$_c$ with Cu substitution was found in the underdoped BaFe$_{2-x}$Co$_x$As$_2$ and theoretical calculations have shown that in the s$_{+-}$ state the impurity scattering affects T$_c$ non-monotonically as a function of substitution both directly, via pair-breaking, and indirectly, via the suppression of the SDW phase [111].

We shed new light on this fascinating problem by exploring the interplay between transition-metal (TM) substitution and applied hydrostatic pressure through in-plane electrical resistivity measurements in BaFe$_{1.9}$TM$_{0.1}$As$_2$ (TM = Co, Cu, and Ni) single crystals with applied pressures up to $P \lesssim 25$ kbar. All concentrations were choosen near the optimally doped region. For TM = Cu, we choose the data for a slightly underdoped sample in which $\rho_{ab}(T)$ does not go to zero at zero pressure in order to emphasize the striking enhancement of T$_c$ in this case along with the fact that $\rho_{ab}(T)$ does go to zero for $T \geq 2$ K with pressure.

Substitution	Flux	$\mathbf{T_{max}}$ (°C)	$\mathbf{t_{max}}$ (°C)	**r** (°C/h)	$\mathbf{T^*}$ (°C)	$\mathbf{T_{rem}}$ (°C)
Pure	In	1100	18	10	-	400
Co	In	1100	18	10	-	400
Cu	In	1100	21	3	-	550
Ni	In	1100	18.5	10	-	400
Ru	In	1150	12	2	-	550
Eu	In	1150	12	2	1000	550
Eu	Sn	900	2	2	-	400
*	In	900	1	2	-	400

Table 4.1: Parameters for the heat treatment, illustrated in Fig. 3.1, used in the growth of $BaFe_2As_2$ with different substituting atoms. The asterisk represents the compound $EuIn_2As_2$.

Fig. 4.7 displays the in-plane electrical resistivity of the studied single crystals at ambient pressure. The room-T value of $\rho_{ab}(T)$ varies in the range $0.7 - 1.1$ mΩ.cm. A linear metallic behavior is observed at high temperatures and the parent compound spin-density wave transition ($T_{SDW} \sim 139$ K) is suppressed for all studied compounds.

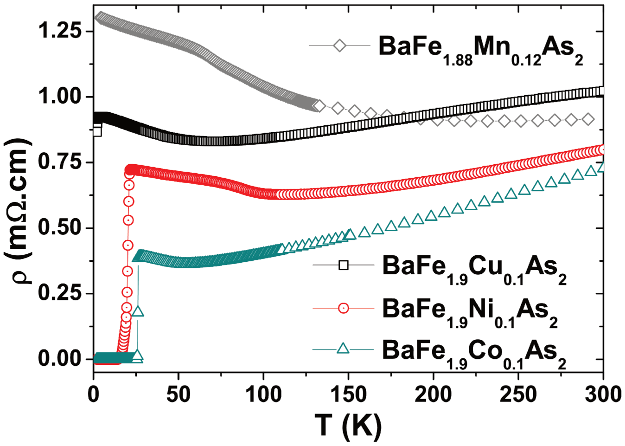

Figure 4.7: Temperature dependence of the in-plane electrical resistivity of $BaFe_{1.9}TM_{0.1}As_2$ (TM = Mn, Co, Ni, and Cu) single crystals at ambient pressure.

As we decrease the temperature, a slight upturn occurs at 55 K, 112 K, and 71 K for Co, Ni, and Cu substitutions, respectively, as typically found for substituted samples in the $BaFe_2As_2$ systems [4]. In the Co and Cu-substitution cases, the upturn may correspond to a vestige of the structural phase transition as we do not observe any transition in the magnetic susceptibility or heat capacity measurements (not shown). The higher upturn temperature of the Cu compound and the fact that $\rho_{ab}(T)$ does not go to zero may suggest that this sample is slightly underdoped. On the other hand, Ni-substituted samples have still SDW ordering at $T_{SDW} \sim 112$ K but already the highest superconducting transition temperatures (T_c) reported for this substitution so far. The onset of T_c occurs at 26.1 K, 22.2 K, and 3.8 K, respectively [1]. The higher upturn temperature of the Ni compound and the fact that $\rho_{ab}(T)$ does not go to zero for the Cu sample suggest that these samples are slightly underdoped.

The in-plane electrical resistivity under hydrostatic pressure ($\sim$ 4 –24 kbar) as a function of temperature for the Co and Ni-substituted compounds is shown in Fig. 4.8. We observe a small T_c increase of $\sim 2 - 3$ K, as expected for nearly optimally doped samples [4].

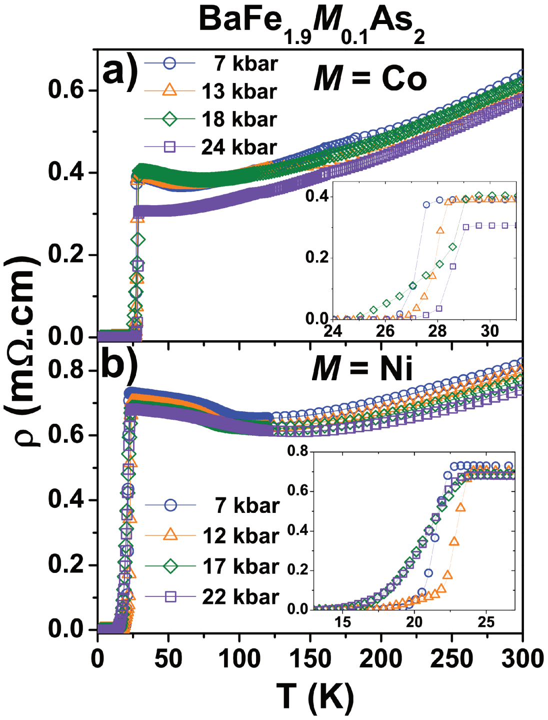

Figure 4.8: Temperature dependence of the in-plane electrical resistivity $\rho_{ab}(T)$ of $BaFe_{2-x}TM_xAs_2$ (TM = Co and Ni) single crystals at various pressures ($\sim$ 7 –24 kbar)

For TM = Co, T_c saturates at 28.6 K for $P \sim 18$ kbar. Interestingly, this is the same maximum T_c obtained for the pure compound $BaFe_2As_2$ under pressure ($P \sim 40$ kbar), indicating that Co-substitution and pressure have the same structural effect that suppresses the SDW phase and induces superconductivity [112]. In fact, EXAFS measurements showed that both Co and K substitution and also applied pressure lead to a slight compression of the As-(Fe,Co) bond ($\lesssim 0.01$ Å) with respect to the pure compound. On the other hand, for TM = Ni, T$_c$ saturates at 24.7 K for $P \sim 12$ kbar. Consistently, the SDW transition temperature of the Ni-sample, defined as the valley in the first derivative of $\rho(T)$ (not shown), decreases with pressure and it is not observed for $P \gtrsim 20$ kbar. One can speculate that the reason why the Ni-substituted sample does not achieve T$_c$ $\sim$ 29 K is because it introduces more disorder than cobalt. In fact, the residual resistivity is higher for TM = Ni. Moreover, the highest T$_c$'s found in the Fe-based superconductors (38 K for the 122-system $Ba_{0.6}K_{0.4}Fe_2As_2$ and 53 K for the oxides 1111 $Gd_{0.8}Th_{0.2}FeAsO$) are obtained through out-of-plane substitution, without introducing disorder in the FeAs plane [113, 114].

---

[1] We define the onset of T_c as the temperature at which $d\rho/dT = 0$.

Now we turn our attention to the striking behavior of the Cu-substituted compound, shown in Fig. 4.9. First, there is a drastic decrease in the room-T resistivity by a factor of three as we apply pressure (see Fig. 4.7 for comparison), indicating a large decrease in the impurity scattering potential.

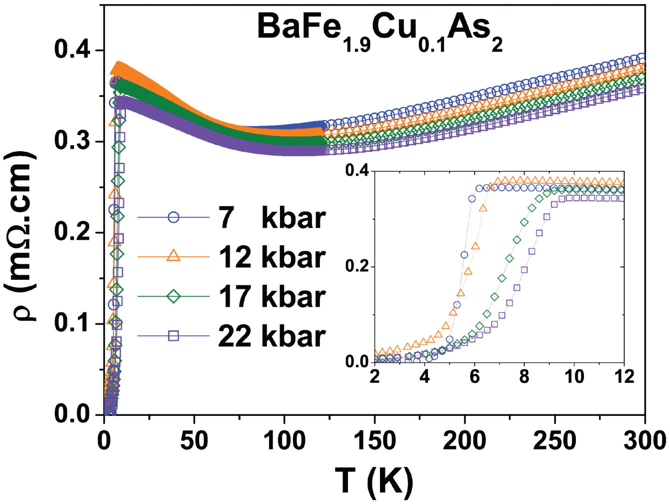

Figure 4.9: Temperature dependence of the in-plane electrical resistivity of $BaFe_{1.9}Cu_{0.1}As_2$ single crystals under hydrostatic pressure.

Moreover, we observe that $\rho_{ab}(T)$ goes to zero with applied pressure and that there is a huge unexpected T$_c$ enhancement by a factor of ~ 2.5 ($T_c = 10$ K at $P \sim 24$ kbar). All these results together are strong evidences that the hybridization between the Cu 3d bands and the Fe 3d bands increases and, consequently, the impurity scattering by the Cu local moments decreases. In this manner, the pair-breaking mechanism due to the inter-band scattering rate (Γ_π) is suppressed and

T$_c$ is, in principle, unconstrained to increase up to a maximum defined by the local distortions generated by the transition metal substitution. It remains to be seen whether applying higher pressures with Diamond Anvil Pressure (DAC) cells would further enhance or even suppress T$_c$.

Another strong evidence that the Cu ion enters as a local moment at the Fe site is the existence of an ESR line. Fig. 4.10 shows the X-Band ($\nu \sim 9.5$ GHz) ESR spectra at $T = 150$ K for the $BaFe_{1.9}Cu_{0.1}As_2$ powdered crystals. The ESR lines have a symmetric Lorentzian character (sample size smaller than the skin depth [75]) and from fitting to the resonances (solid lines), we obtained a linewidth of $\Delta H = 600$ G and a g-value of $g = 2.08$. It is worth noting that the observation of an ESR line also indicates that the Cu oxidation state is in fact Cu^{2+} and consequently there is no real doping in this material.

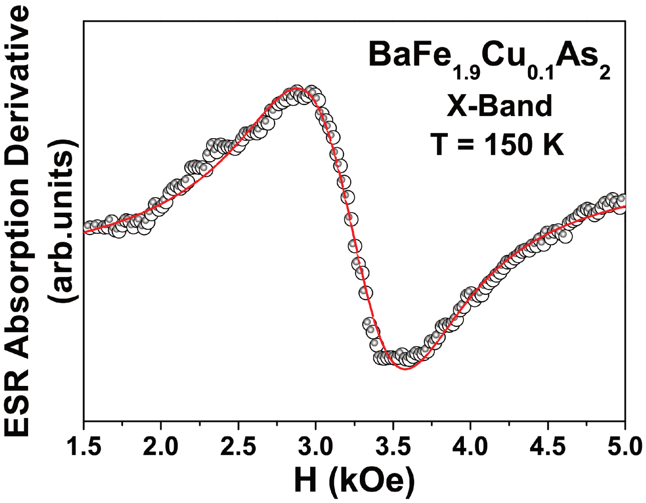

Figure 4.10: X-Band spectra at $T = 150$ K for powdered crystals of $BaFe_{1.9}Cu_{0.1}As_2$.

Finally, we summarize our data in the phase diagram T$_c$ *vs.* P, displayed in the inset of Fig. 4.11. For the Co and Ni substitutions the pressure coefficient is $dT_c/dP \sim 0.1$ K/kbar, as expected for nearly optimally doped samples in which the magnetic instability is completely suppressed and the application of pressure has little effect in T$_c$. However, $dT_c/dP \sim 0.3$ K/kbar is three times larger for the Cu-substituted sample, indicating that, although the magnetic instability has been suppressed, the pair-breaking mechanism has also been suppressed by the increase of hybridization between the Cu and the Fe 3d bands.

Thus, there is a constrasting behavior of hydrostatic pressure effects on nearly optimally doped $BaFe_{2-x}TM_xAs_2$ (TM = Co, Cu, and Ni) high quality single crystals grown using the In-flux method. For Co and Ni-substitution, T$_c$ increases only ~ 2 K at a rate $dT_c/dP \sim 0.1$ K/kbar,

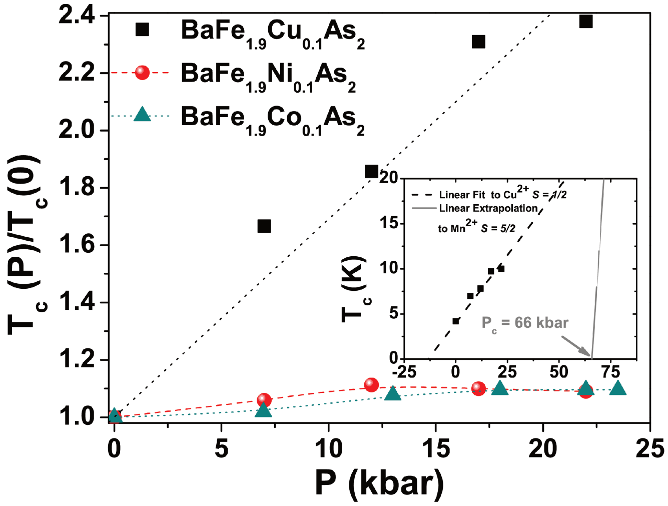

Figure 4.11: Phase Diagram for $BaFe_{2-x}TM_xAs_2$ (TM = Co, Cu, and Ni) single crystals as a function of pressure: $T_c(P)$ normalized by its zero pressure value $T_c(0)$ *vs.* pressure and T_c *vs.* pressure (P) (inset).

consistent with the nearly optimal doping region. On the other hand, in the Cu-substituted sample T_c increases $\sim$ 6 K at a rate $dT_c/dP \sim 0.3$ K/kbar. This huge T_c enhancement by a factor of $\sim$ 2.5 with pressure and the local Cu^{2+} ESR line provide strong evidence that the hybridization between the Cu 3*d* bands and the Fe 3*d* bands increases with pressure and, consequently, the impurity scattering by the Cu local moments decreases. It is worth noting that this is in agreement with the fact that the end-compound $BaCu_2As_2$ is a regular metal.

In order to further understand the spin effects on the pairing mechanism, we can now study Mn-substituted compounds. Although the Cu substitution induces a smaller T_c, in the Mn-substituted compound T_c has not been observed although the SDW phase is effectively suppressed.

Fig. 4.12 displays the in-plane electrical resistivity of $BaFe_{2-x}Mn_xAs_2$ single crystals at ambient pressure and under hydrostatic pressure (0 –25 kbar).

At low Mn concentration ($x = 0.007$), the SDW phase is slightly suppressed ($T_{SDW} = 130$ K) and we observe a kink in the resistivity at $\sim$ 20 K but the resistivity does not go to zero, indicating that the superconducting volume is small. In fact, we observe this kink at the same temperature even in the pure $BaFe_2As_2$ compound when the surface is altered (due to polishing or etching). At higher Mn concentration ($x = 0.12$), the SDW phase is further suppressed and only a slight upturn is observed at $T^* = 70$ K. However, superconductivity does not emerge for the studied pressure range, indicating a stronger pair-breaking mechanism. As in the case of Cu^{2+} ($S = 1/2$),

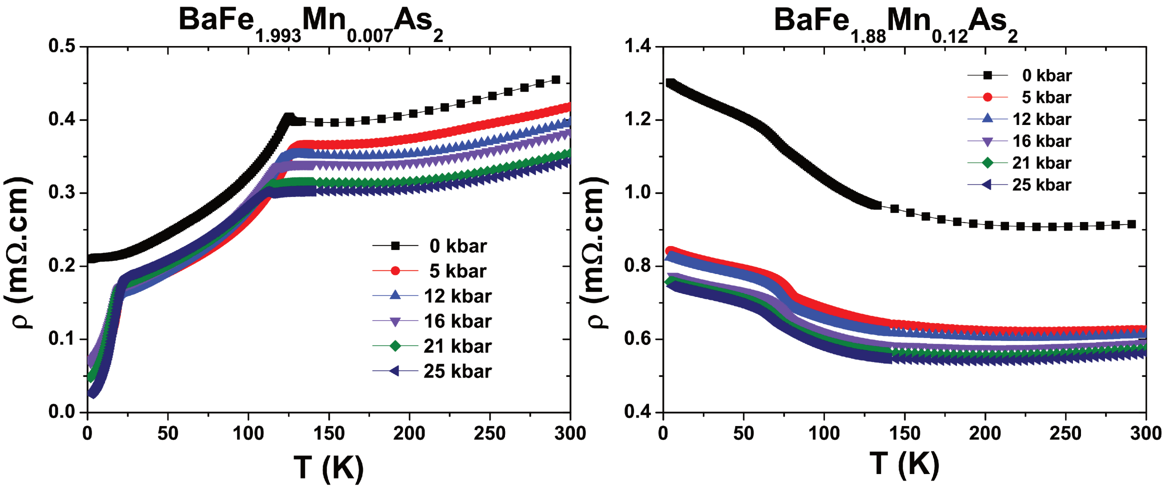

Figure 4.12: Temperature dependence of the in-plane electrical resistivity of $BaFe_{2-x}Mn_xAs_2$ ($x = 0.007, 0.12$) single crystals at ambient pressure and under hydrostatic pressure (0 –25 kbar).

we also observe a ESR line due to the Mn^{2+} ions (see Chapter 5 for a detailed study). However, Mn^{2+} has a much higher spin ($S = 5/2$) which suggests a stronger pair-breaking. Moreover, the end-compound $BaMn_2As_2$ has a high antiferromagnetic ordering temperature $T_N = 618$ K of the Mn ions, indicating that short-range Neel pair-breaking fluctuations can also play a role. In this manner, higher pressure is needed in order to induce superconductivity. In Section 5.2 we will provide an estimative of the critical pressure.

In order to further explore the Mn pair-breaking mechanism, we also studied the Co-substituted $BaFe_{1.805}Co_{0.190}Mn_{0.005}As_2$ compound. Fig. 4.13 displays the electrical resistivity as a function of temperature. One can still observe a slight upturn at $T^* \sim 80$ K indicating that the sample is slightly underdoped. For the Co-substituted compound without Mn this T^* corresponds to $T_c \sim 22$ K. However, the small amount of Mn substitution $x_{Mn} = 0.005$ is already effective in suppressing T_c to 16 K.

Now we turn our attention to the out-of-plane local moments which also act as a pair-breaking mechanism, although much weaker. Figures 4.14-4.15 display the in-plane electrical resistivity of $Ba_{1-x}Eu_xFe_{2-y}Co_yAs_2$ single crystals at ambient pressure and under hydrostatic pressure (0 –26 kbar). A linear metallic behavior is observed at high temperatures and again the parent compound spin-density wave transition ($T_{SDW} \sim 139$ K) is suppressed. As we decrease the temperature, a slight upturn occurs at 81 K and 106 K for $Ba_{0.99}Eu_{0.01}Fe_{1.9}Co_{0.1}As_2$ and $Ba_{0.8}Eu_{0.2}Fe_{1.9}Co_{0.1}As_2$, respectively, as typically found for substituted samples in the $BaFe_2As_2$ systems. However, the higher upturn temperature of $Ba_{0.8}Eu_{0.2}Fe_{1.9}Co_{0.1}As_2$ suggests that this sample is slightly underdoped as compared to $Ba_{0.99}Eu_{0.01}Fe_{1.9}Co_{0.1}As_2$. The onset of T_c at ambient pressure occurs at

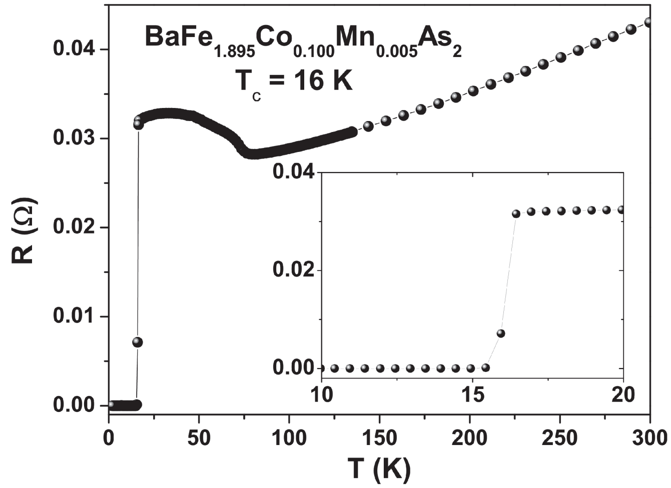

Figure 4.13: Temperature dependence of the in-plane electrical resistivity of $BaFe_{1.805}Co_{0.190}Mn_{0.005}As_2$ single crystals at ambient pressure.

24.2 K, and 22.1 K, for $Ba_{0.99}Eu_{0.01}Fe_{1.9}Co_{0.1}As_2$ and $Ba_{0.8}Eu_{0.2}Fe_{1.9}Co_{0.1}As_2$, respectively. The Eu ion has a huge local moment $S = 7/2$, hence the decrease in T_c. However, this decrease is much smaller than in the Mn case due to the fact that Eu ions are out of the FeAs plane. An analysis of these results considering the conventional Abrikosov-Gorkov formalism for the superconductivity suppression is performed in Section 5.2.

The phase diagram T_c vs. P is shown in Fig. 4.16. As one can see, there is a small T_c increase of ~ 1 K for $Ba_{0.8}Eu_{0.2}Fe_{1.9}Co_{0.1}As_2$ followed by a small decrease of the same order. This dome is expected for nearly optimally doped samples. At low pressure, the same behavior of T_c is found for the $Ba_{0.8}Eu_{0.2}Fe_{1.9}Co_{0.1}As_2$ sample. However, a striking behavior occurs above ~ 15 kbar and T_c starts to increase again. This can only happen if there is a pair breaking mechanism that is suppressed with applied pressure. As we are in the very diluted regime ($x_{Eu} = 0.01$) it is reasonable to speculate that the observed behavior is reminiscent of a Kondo single impurity regime and that the Eu local moment is screened by the conduction electrons as we applied pressure.

4.2.2 Electrical Resistivity Measurements at High Magnetic Fields

We have studied four In-grown single crystals by Shubunikov-de Hass oscillations, see Table 4.2. It is worth noting that our $EuFe_2As_2$ crystals have the highest RRR found in the literature. For Sn-flux grown crystals $RRR = 7$ and $T_{SDW} = 190$ K. For crystals grown by the Bridgman method

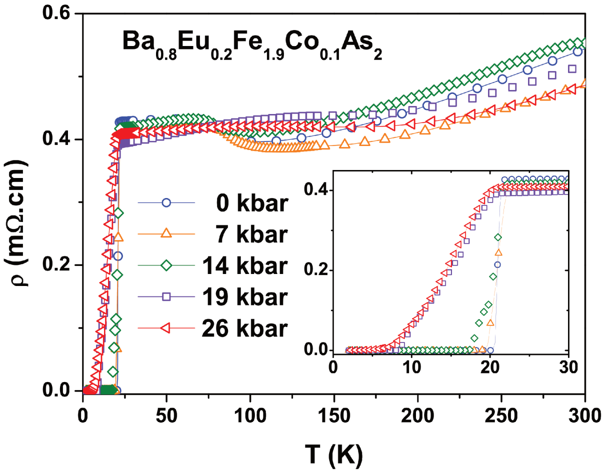

Figure 4.14: Temperature dependence of the in-plane electrical resistivity of $Ba_{0.8}Eu_{0.2}Fe_{1.9}Co_{0.1}As_2$ single crystals at ambient pressure and under hydrostatic pressure (0 –26 kbar).

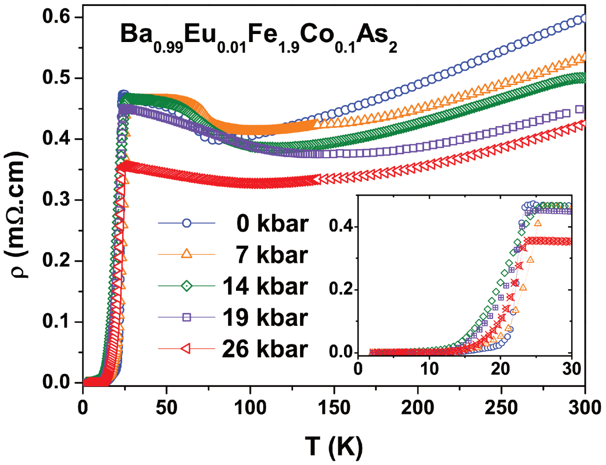

Figure 4.15: Temperature dependence of the in-plane electrical resistivity of $Ba_{0.99}Eu_{0.01}Fe_{1.9}Co_{0.1}As_2$ single crystals at ambient pressure and under hydrostatic pressure (0 –26 kbar).

RRR = 15 and T_{SDW} = 194 K. For In-flux grown single crystals we obtained RRR = 24 and T_{SDW} = 194 K. Interestingly, there is no report concerning the quantum oscillation in $EuFe_2As_2$,

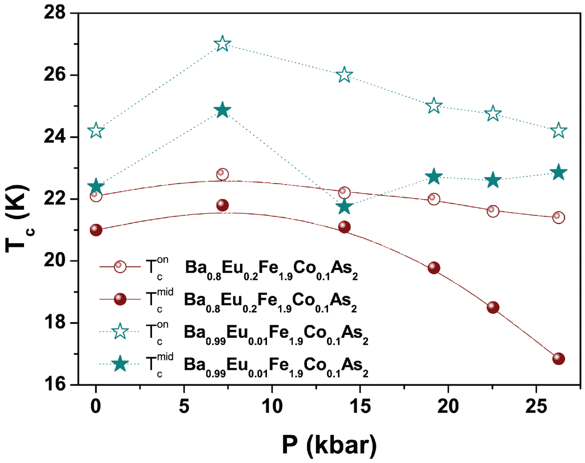

Figure 4.16: Phase diagram T_c vs. P for $Ba_{0.99}Eu_{0.01}Fe_{1.9}Co_{0.1}As_2$ and $Ba_{0.8}Eu_{0.2}Fe_{1.9}Co_{0.1}As_2$ single crystals.

despite the importance of understanding the Fermi surface topology and mass renormalization.

Sample	ρ_0	RRR	$\rho(H=45\,T)/\rho(H=0\,T)$
$BaFe_2As_2$ (1)	0.015	5	5.5
$EuFe_2As_2$ (2)	0.007	22	15.6
$BaFe_2As_2$ (3)	0.105	8	4.9
$EuFe_2As_2$ (4)	0.011	24	14.5

Table 4.2: Samples studied by Shubunikov-de Haas oscillations and their residual resistivity ρ_0, residual resistivity ratio (RRR), and magnetoresistance.

Figure 4.17 displays the physical properties of the selected crystals. One can clearly see the jumps in specific heat related to the Fe SDW ordering at T_{SDW} = 194 K and T_{SDW} = 139 K for the $EuFe_2As_2$ and $BaFe_2As_2$ compounds, respectively, and a clear kink in the electrical resistivity measurements.

By applying a magnetic field up to 45 T we were able to observe beautiful quantum oscillations for both compounds, Fig. 4.18. in the inset of Figure 4.18. We then take the Fourier transform of this subtracted data in order to find the frequencies at which extremal areas exist.

The Fourier content is shown in Fig. 4.19. Four resolved frequencies are observed at 0° for $BaFe_2As_2$ (Fig. 4.19a): F_1 = 96 T, F_2 = 187 T, F_3 = 427 T and F_4 = 511 T, in very good agreement with the data in the literature [115, 84]. On the other hand, the $EuFe_2As_2$ compound

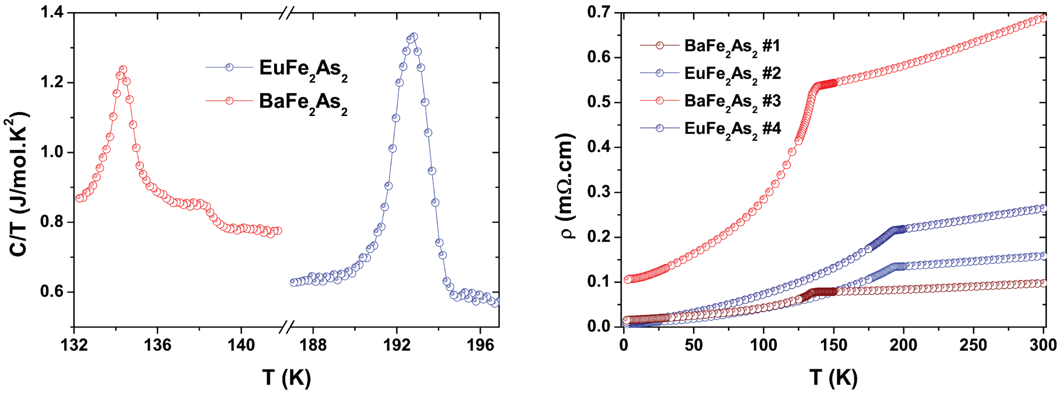

Figure 4.17: (left panel) Specific heat per mole versus temperature for $BaFe_2As_2$ and $EuFe_2As_2$ single crystals. (right panel) Temperature dependence of the in-plane electrical resistivity of $BaFe_2As_2$ and $EuFe_2As_2$ single crystals.

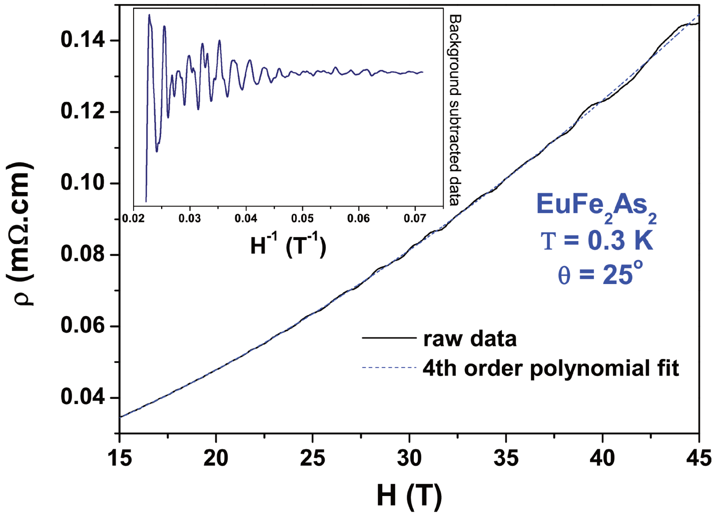

Figure 4.18: Raw-data resistivity and 4th order polynomial fit (background) as a function of the magnetic field for $EuFe_2As_2$. The inset shows the background subtracted data as a function of inverse magnetic field.

reveals only two frequencies at this angle $F_1 = 328$ T, $F_2 = 386$ T. In order to obtain the other frequencies we rotated the single crystals and, at $\theta = 25°$ (Fig. 4.19b), we clearly observe five frequencies for the $EuFe_2As_2$ compound at $F_1 = 350$ T, $F_2 = 394$ T, $F_3 = 846$ T, $F_4 = 938$ T and

$F_5 = 1038$ T.

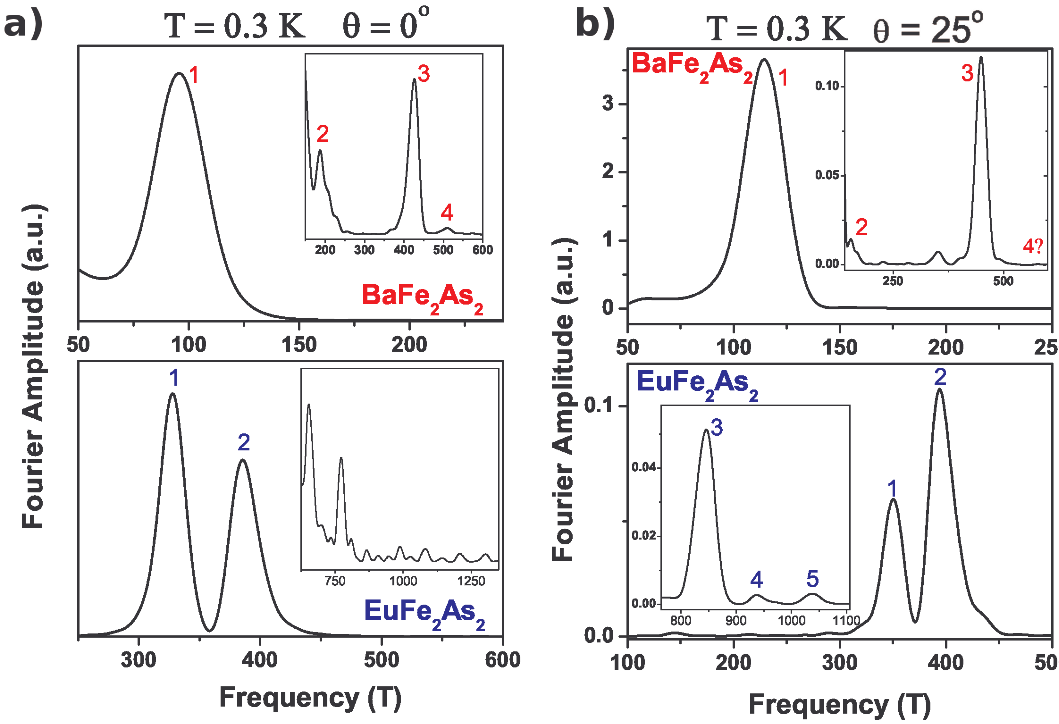

Figure 4.19: Fourier analysis of the quantum oscillations at two different angles $\theta = 0°$ and $\theta = 25°$ measured with respect to the *c*-axis.

Except for the $BaFe_2As_2$ frequency F_4, we were able to extract the effective masses by fitting the temperature dependence of the oscillation amplitude with the thermal damping term;

$$R_T = \frac{X}{sinh(X)}, \qquad X = 14.69\frac{m^*T}{B}, \tag{4.1}$$

of the Lifshitz-Kosevich (LK) formalism, where m^* is the effective mass and $1/B$ is the average inverse field of the Fourier window, taken between 12 T - 35 T or 14 T - 45 T. Figure 4.20a displays our effective masses for both $EuFe_2As_2$ and $BaFe_2As_2$ compounds and Figure 4.20c shows the data from the literature for comparison.

As mentioned in Section 3.3.2, the observed frequencies are proportional to the extremal areas at the Fermi surface. Thus, at this point we can draw our first conclusion: $EuFe_2As_2$ has larger pockets at the Fermi surface and at least two of them have heavier masses than the pockets in the Ba122 compound, suggesting that Eu122 is more correlated than Ba122.

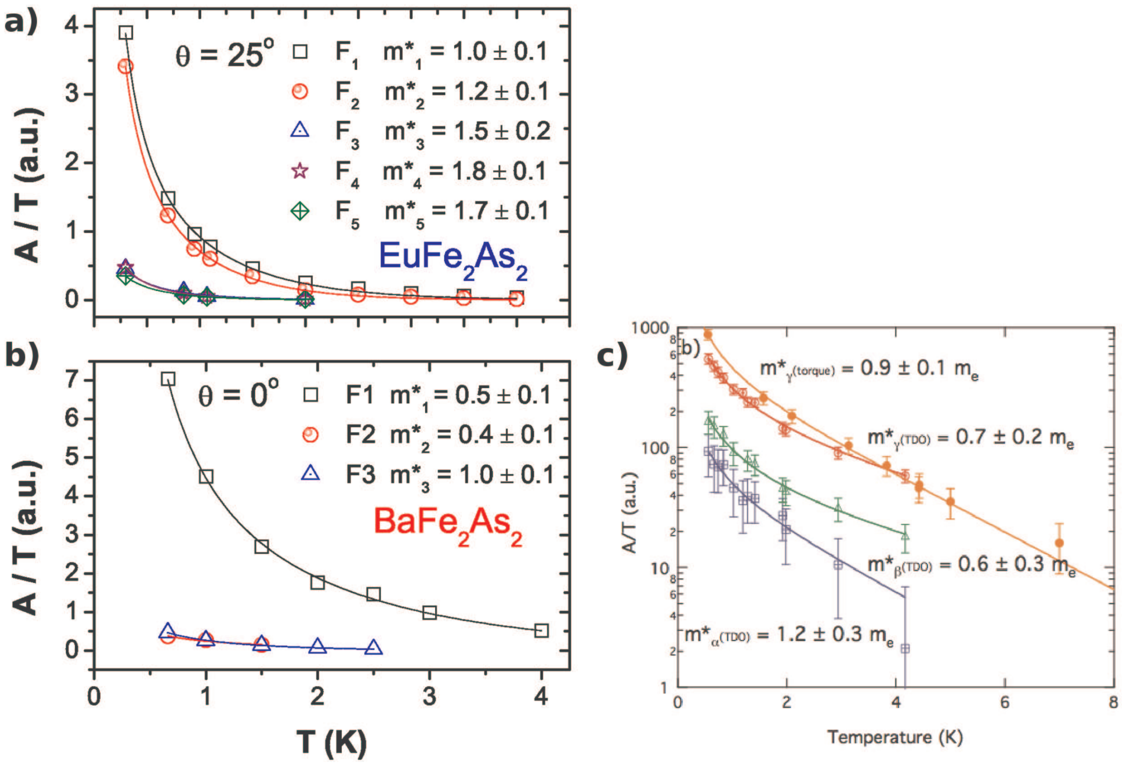

Figure 4.20: (a-b) Effective masses for both $EuFe_2As_2$ and $BaFe_2As_2$ compounds, respectively. (c) Data from the literature [115] for $BaFe_2As_2$.

In order to identify these frequencies with the hole/electron pockets in the Fermi surface, the analysis of the angle dependence and band structure calculations are in progress. In any case, for the conclusion of this thesis we only need the above statement.

Chapter 5

Microscopic Properties: The Role of Local Distortions

In this chapter the microscopic experimental results of this work are presented. In the first part, EXAFS measurements are presented for the parent compound $BaFe_2As_2$ under hydrostatic pressure and chemical substitution with Co (at first, though as an electron donor) and K (hole donor). It is shown an equivalence between substitution and pressure concerning the tuning in the relevant structural parameter: the Fe-As bond distance decreases. Furthermore, it is shown that Co-substitution has no effects on the Fe valence in the $BaFe_2As_2$ compound and thus does not change the electronic occupation of the Fe ions. In the second part, ESR measurements are discussed in detail for the series $Ba_{1-x}Eu_xFe_2As_2$ and then generalized for several compounds of the series $Ba_{1-x}Eu_xFe_{2-y}TM_yAs_2$. The data show strong evidences that by decreasing the Fe-As distance there is a localization of the Fe 3d orbitals at the FeAs plane. The xy orbital is more localized than the others (xz and yz) and, in turn, leads to a suppression of the itinerant SDW phase with the emergence of superconductivity.

5.1 EXAFS and XANES Measurements

Starting with the physical properties of the studied single crystals, Fig.5.1 presents the temperature dependence of the in-plane electrical resistivity. $BaFe_2As_2$ shows a sharp derivative change in $\rho(T)$ at $T_{SDW} = 139$ K, marking the antiferromagnetic transition. This indicates no In-incorporation into our $BaFe_2As_2$ sample, confirmed by the EDS technique. For $BaFe_{2-x}Co_xAs_2$ no antiferromagnetic transition was observed and a transition to a superconducting state was found at $T_c = 22$ K. Finally, the BKFA sample shows a superconducting transition at $T_c = 13$ K, and a change of concavity in ρ(T) at $T_0 \sim 108$ K. Previous nuclear magnetic resonance measurements on a similar sample suggest negligible Sn incorporation in BKFA [116].

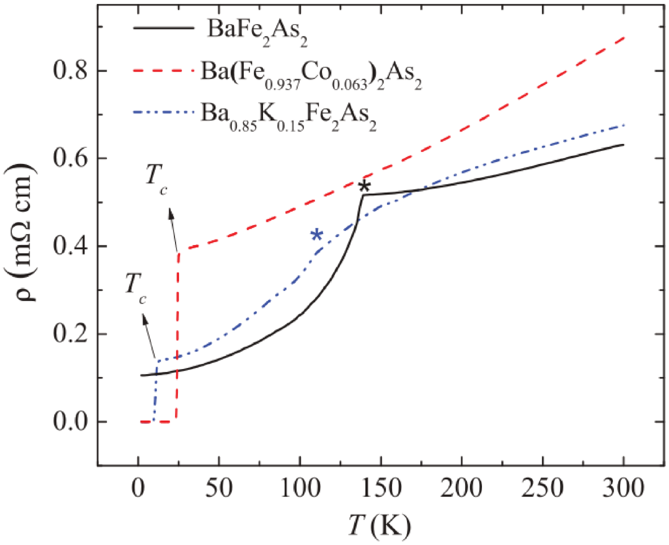

Figure 5.1: Temperature dependence of the in-plane resistivity of $BaFe_2As_2$, $Ba(Fe_{0.937}Co_{0.063})_2As_2$, $Ba_{0.85}K_{0.15}Fe_2As_2$. The arrows indicate the onset of superconductivity at T_c, and asterisks mark the antiferromagnetic transition temperatures.

The crystal thickness (d $\sim$ 40 Å) was appropriate to perform high-quality EXAFS measurements in transmission mode at the As K edge (E = 11865 eV) but the crystals were too thick for transmission EXAFS measurements at the Fe and Co K edges (E = 7116 and 7713 eV, respectively). According to the crystal structure of $BaFe_2As_2$, each As ion is surrounded by four Fe (or Co) nearest neighbours (see Chapter 1, Fig. 1.5), defining the first As coordination shell with $d_{As-Fe} \sim 2.4$ Å. In both tetragonal and orthorrombic phases a single As-Fe bond distance is defined. The As second nearest neighbours are the Ba ions with significantly large $d_{As-Ba} \sim 3.4$ Å. Finally, the third shell are the As-As distances $d_{As-As} \sim 3.8 - 4.0$ Å. Thus, the EXAFS signal arising from the As-(Fe,Co) first shell can be unambiguosly isolated and analysed, making EXAFS at the As K edge an ideally suited technique to study the As-(Fe,Co) bond in these materials.

Figures 5.2(a)-5.2(c) show the As K edge k^2-weighted raw EXAFS data $[k^2\chi(k)]$ at $T = 298$ K for $BaFe_2As_2$, $BaFe_{2-x}Co_xAs_2$, and BKFA, respectively. The magnitude of the Fourier transform of $k^2\chi(k)$ into the real space $[\chi(R)]$ is given in Fig. 5.3 for the three studied compounds at room temperature and at 2 K. These data show an amplitude peak in $\chi(R)$ centered at the non phase-corrected radial distances $R \sim 2.05$ Å, which is readily associated with the As-(Fe,Co) first shell. The regions $2.5 \lesssim R \lesssim 3.3$ Å, associated with the As-(Ba,K) coordination shell, are substantially

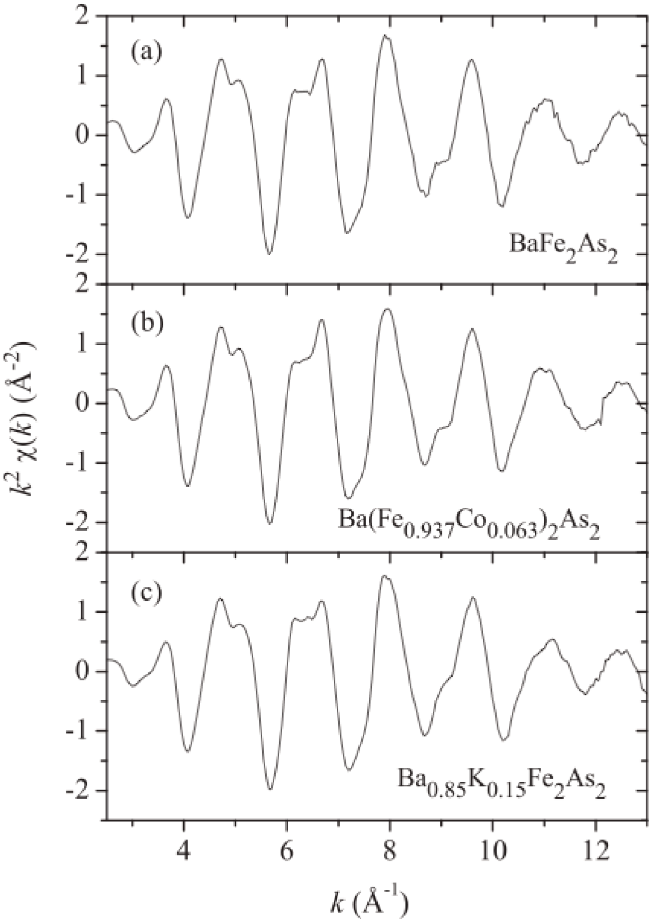

Figure 5.2: k^2-weighted As K edge extended x-ray absorption fine structure $[k^2\chi(k)]$ spectra of (a) $BaFe_2As_2$, (b) $Ba(Fe_{0.937}Co_{0.063})_2As_2$, and (c) $Ba_{0.85}K_{0.15}Fe_2As_2$ at $T = 298$ K.

altered for the $Ba_{1-x}K_xFe_2As_2$ sample with respect to $BaFe_2As_2$ and $BaFe_{2-x}Co_xAs_2$, due to the highly different scattering amplitudes of Ba and K. Finally, all studied compounds show similar features in $\chi(R)$ for $R > 3.3$ Å.

The envelope, real and imaginary components of $\chi(R)$ for $BaFe_2As_2$ at 298 K are shown in Fig.5.4(a). A fit of these data to a simple first-shell model in the region of interest is illustrated (solid lines). Fig.5.4(b) shows the nearly perfect fit to the backward Fourier transform data of $\chi(R)$ in the first shell interval $1.6 < R < 2.5$ Å$[\chi(q)]$.

Table 5.1 shows the refined As-(Fe,Co) bond distances and Debye-Waller factors (σ^2) for $BaFe_2As_2$, $BaFe_{2-x}Co_xAs_2$, and BKFA at 2, 30, and 298 K. For $BaFe_2As_2$ the As-Fe bond distance reported here at 2 K is consistent with that obtained by neutron powder diffraction at 5 K, within experimental errors. Both Co and K substitution lead to a slight compression of the

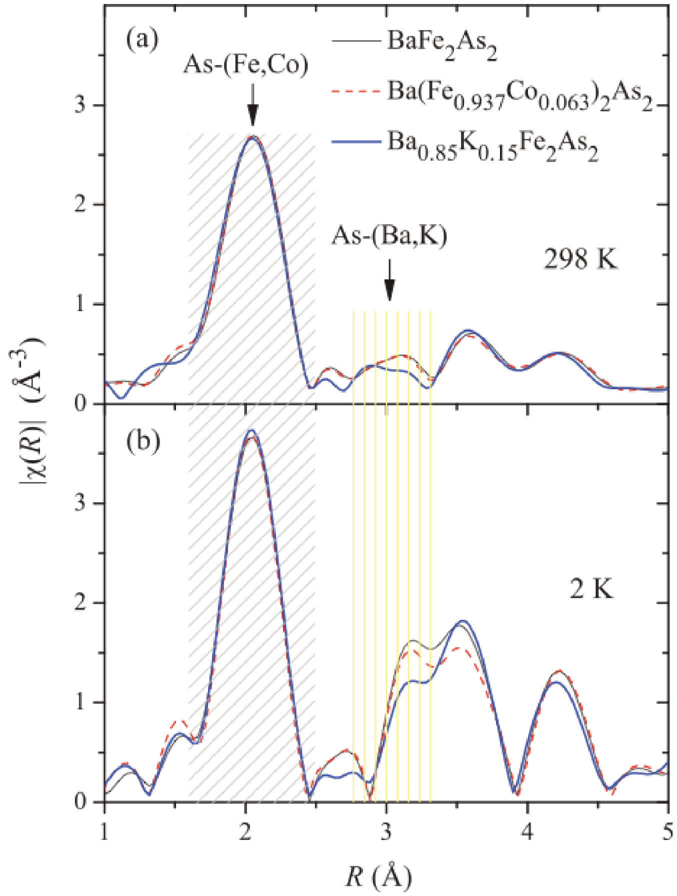

Figure 5.3: Magnitude of the Fourier transform of As K edge $k^2\chi(k)$ curves given in Figs. 5.2(a)-5.2(c) for $\mathrm{BaFe_2As_2}$, $\mathrm{Ba(Fe_{0.937}}Co_{0.063})_2\mathrm{As_2}$, and $\mathrm{Ba_{0.85}K_{0.15}Fe_2As_2}$ at (a) T = 298 K and (b) T = 2 K. The intervals corresponding approximately to the first [As-(Fe,Co)] and second [As-(Ba,K)] As coordination shells are indicated as dashed areas.

As-(Fe,Co) bond ($\lesssim$ 0.01 Å) with respect to the pure compound. Also, no systematic increase of the σ^2 for this bond may be noticed for the substituted compounds. The nearly identical σ^2 for all studied samples reveal no observable disorder in this bond length brought by K and, most remarkably, Co substitution. As expected, the As-(Fe,Co) bond distances decrease slightly on cooling from room temperature down to 2 K for all investigated samples. Also, σ^2 for this bond is sensibly reduced on cooling for all studied compounds and consistent with previously reported compounds, reaching values close to $\sigma^2 = 0.0025$ Å^2 at 2 K. No variations of As-(Fe,Co) distance or σ^2 between the superconducting and normal states at 2 and 30 K, respectively, were observed for $\mathrm{BaFe_{2-x}Co_xAs_2}$ within experimental errors. However, there is a tendency for slightly shorter

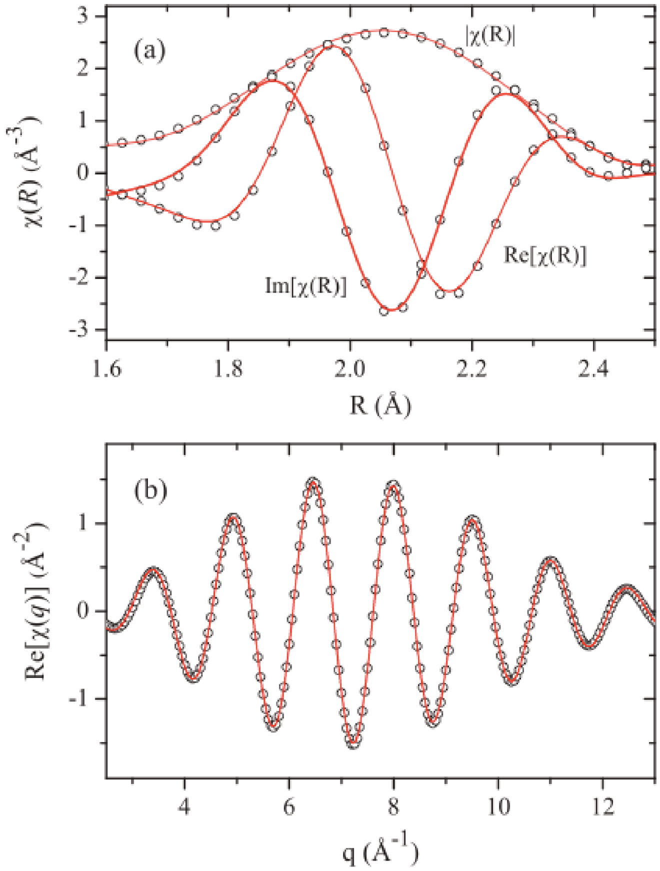

Figure 5.4: (a) Envelope, real and imaginary components $\chi(R)$ for $BaFe_2As_2$ at $T = 298$ K in the first shell interval. (b) Real component of the backward Fourier transform of $\chi(R)$ ($1.6 < R < 2.5$ Å), $\chi(q)$. Circles: experimental data; solid lines: calculated.

As-(Fe,Co) bonds for both substitutions with respect to the parent compound. For BKFA a possible As-(Fe,Co) bond elongation of 0.0035(19) Å^2 takes place between 2 and 30 K. Since this possible elongation was within two standard deviations and it was observed for only one sample, we do not ascribe statistical significance to it.

Now we turn our attention to the effects of applied hydrostatic pressure. Figure 5.5(a) shows $k^2\chi(k)$ for the pure compounds taken in dispersive geometry at the As K edge with the sample inside the diamond anvil cell, at room temperature and selected pressures. Within the acessible k range, the spectrum seen in Fig. 5.5(a) is consistent with the one shown in Fig. 5.2(a). The real part of the Fourier transform of $k^2\chi(k)$ into the real space is given in 5.5(b). Due to the limited k range the resolution in R space is degraded with respect to the data shown in Fig.5.3. However, since the As first shell is completely separated from the second shell, an analysis of the local As-Fe

	$T = 2$ K	$T = 30$ K	$T = 298$ K
$BaFe_2As_2$			
d(As-Fe) (Å)	2.3915(12)	2.3914(7)	2.3985(14)
σ^2 (Å^2)	0.00266(12)	0.00250 (7)	0.00465(11)
$Ba[Fe_{0.937}Co_{0.063}]_2As_2$			
d[As-(Fe,Co)] (Å)	2.3833(12)	2.3838(9)	2.3951(12)
σ^2 (Å^2)	0.00262(12)	0.00268(9)	0.00466(9)
$Ba_{0.85}K_{0.15}Fe_2As_2$			
d(As-Fe) (Å)	2.3865(15)	2.3900(12)	2.3955(9)
σ^2 (Å^2)	0.00242(15)	0.00248(12)	0.00466(7)

Table 5.1: Refined As-M (M = Fe, Co) distances and Debye-Waller factor obtained from the fits of x-ray absorption fine structure data at the As K edge at ambient pressure. Errors given in parentheses are statistical only, and are defined as the standard deviation of the results obtained from repeated measurements under identical conditions.

bond with pressure is still possible. Clearly, the application of pressure leads to a phase change of $k^2\chi(k)$, corresponding to a reduction of the Fe-As bond distance. These trends are reversible, at least for pressures up to 8.6 GPa, which is the maximum value reached in this study.

Figure 5.6 shows the pressure dependence of the refined As-Fe bond distance. From a linear fit to the data below 6.1 GPa, a compressibility $\kappa = 3.3(3) \times 10^{-3}$ GPa^{-1} was obtained for this bond. Therefore, Co and K substitutions, as well as application of pressure, produce at least one common qualitative structural trend, that is, a shortening of the As-(Fe,Co) bond. For the specific case of $BaFe_{2-x}Co_xAs_2$, the shortening of the As-(Fe,Co) bond of ~ 0.01 Å at low temperature with respect to $BaFe_2As_2$ could be, in principle, attributed to smaller As-Co bond lengths with respect to As-Fe. However, the small Co concentration and the negligible bond disorder introduced by Co substitution dismiss this hypothesis, and we conclude that a significant local contraction of the As-Fe bond is induced by Co substitution, such as in the case of K substitution and applied pressure.

Besides the important role of this structural parameter, there was an intense debate concerning the role of substitution in these materials, specifically whether it acts effectively as a charge carrier doping or as chemical pressure. A convenient approximation to investigate the effects of Co-substituion on the electronic structure under density funtional theory (DFT) has been the virtual crystal approach, in which the extra nuclear charge of Co in the Fe crystallographic site is averaged out without need of a supercell. Under this approximation, a shift in the chemical potential with increasing Co content is computed, similar to that predicted by electron doping. Angular resolved

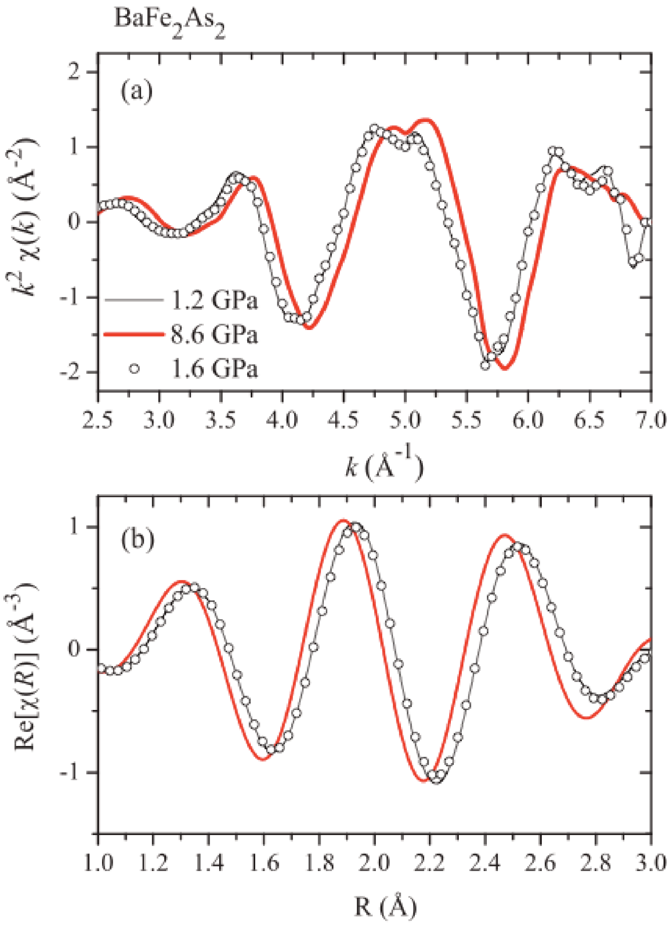

Figure 5.5: (a) k^2-weighted As K edge extended x-ray absorption fine structure $[k^2\chi(k)]$ spectra of $BaFe_2As_2$ at 298 K with the sample leaded into the diamond anvill cell with $P = 1.2$ GPa (thin line), and $P = 8.6$ GPa (thich line), and $P = 1.6$ GPa after release from $P = 8.6$ GPa (circles). (b) Real component of the Fourier transform of $k^2\chi(k)$ curves given in (a).

photoemission spectroscopy (ARPES) experiments show an evolution of the hole and electron pockets of the Fermi surface with Co-substitution that is consistent with this shift. However, this terminology brings an implicit assumption (not verified experimentally by an element-specific probe at that time) that Co substitution is able to tune the Fe electronic occupation and virtual crystal approximation cannot estimate the real space density distribution of the extra d electrons theoretically brought by cobalt. In this sense, a supercell approach to DFT with a distribution of 87.5% of Fe and 12.5% of Co has been applied, leading to a prediction that the excess d electrons from the impurity are actually concentrated at the substitute Co site with no effect on the charge density distribution of the rest of the material [10].

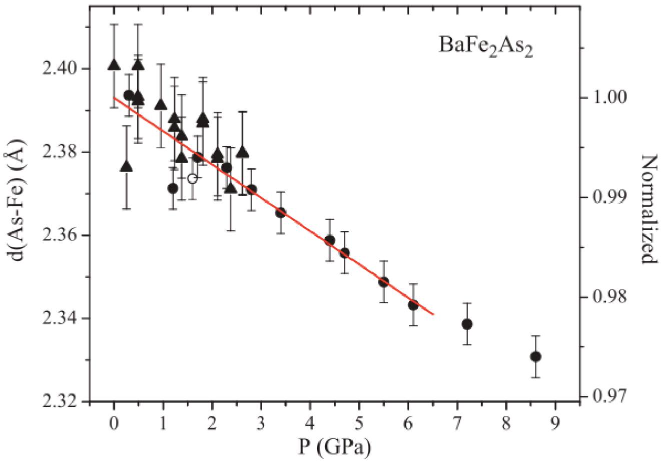

Figure 5.6: Pressure dependence of the As-Fe bond distance at 298 K for BaFe$_2$As$_2$ obtained from the fits to the As K edge x-ray absorption fine structure (see Fig. 5.5). Circles and triangles represent data taken in different runs. Data were taken for increasing pressures, except for the open circle at 1.6 GPa, which was obtained after releasing the cell from 8.6 GPa. Error bars are statistical only and were estimated from the standard deviation of the results obtained from repeated measurements under identical conditions. The solid line is a linear fit to the data below 6.1 GPa, representing a Fe-As bond compressibility of $\kappa = 3.3(3) \times 10^{-3}$ GPa^{-1}.

In order to understand whether Co substitution is able to charge dope the Fe ions in this system, we employed a classic probe to determine element-specific electronic ground states, namely, X-ray absorption near edge structure (XANES) spectroscopy. In the electric dipolar absorption process involved in the Fe K edge, for instance, a photon-induced electronic transition from the Fe $1s$ core level to Fe $4p$ unnocupied states takes place. The energy of the core level and end states are modified in distinct ways by local changes in the electronic occupation due to the characteristic Coulomb interactions of each level with the doped electron or hole, causing a shift of the threshold absorption energy.

Fig. 5.7 displays the in-plane electrical resistivity T-dependence of the five BaFe$_{2-x}$Co$_x$As$_2$ concentrations studied (x $= 0.00, 0.12, 0.17, 0.27$, and 0.38) synthesized by the In-flux technique. Co-substitution clearly suppresses the magnetic transition of the BaFe$_2$As$_2$ compound, and a superconducting state appears as reported in our phase diagram (see Fig. 4.6). The normalized Fe K edge XANES spectrum, μ_E, of BaFe$_2$As$_2$ is given in Fig. 5.8(a) and the first derivative spectrum, $d\mu(E)/dE$, in 5.8(b). Six distinct peaks or shoulders are noticed in the spectral region of interest and are labeled as A - F in Fig. 5.8(a). To each peak or shoulder in that figure a corresponding maximum and a minimim are identified in the first derivative spectrum of 5.8(b) as A'-F' and A''-F'', respec-

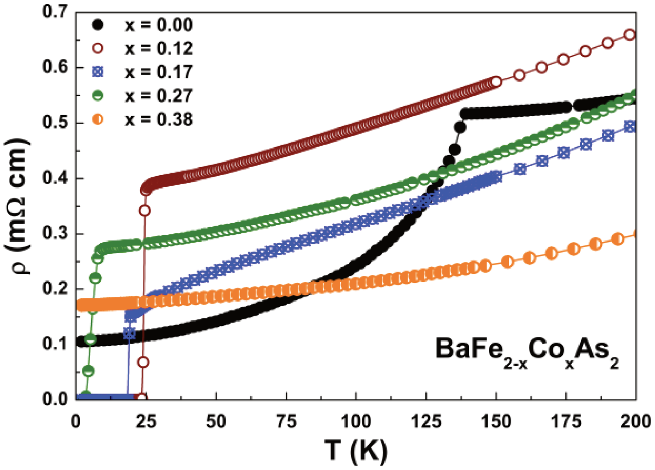

Figure 5.7: In-plane electrical resistivity of $BaFe_{2-x}Co_xAs_2$ as a function of temperature. The solid lines are guide to the eyes.

tively. The reference Fe metal XANES spectrum is shown for comparison. *Ab initio* calculations for XANES spectrum of $BaFe_2As_2$ and its energy dependence derivative are also shown in Fig. 5.8 (solid lines). The calculated spectrum captures fairly well the observed *B*-*F* features: *C*-*F* features above the edge are dipolar transitions to unoccupied Fe *p* projected states. An alternative simulation excluding $1s \to 3d$ quadrupolar transitions (not shown) shows a slightly weaker spectral weight for the *B* shoulder, demonstrating that it originates partly from such transitions and partly from dipolar transitions allowed by $4p$ - $3d$ mixing in the Fe site without inversion symmetry. The observed *A* preedge peak is completely absent in the simulation, possibly because charge-tranfer effects in the absorption process, not fully taken into account in the simulation, pull down the $3d$ states yielding a combination of a well-screened peak *B* and a poorly screened peak *A*, as described in detail in Refs. [60, 61].

Figures 5.8(a) and 5.8(b) show the experimental Fe *K* edge XANES spectra of $BaFe_{2-x}Co_xAs_2$ and the corresponding energy derivatives, respectively. The x dependence of the position A', B', C', D', and E' features of the spectra is shown in Figure 5.9. Remarkbly, these results indicate no observable change in the Fe *K* edge XANES spectra of $BaFe_2As_2$ under Co substitution, contrary to what is observed in *K* edge x-ray absorption spectroscopy studies on transition-metal compounds with controlled valence, such as $La_{1-x}Ca_xMnO_3$, that showed edge shifts of a few eV per valence unit. Also, electron and hole doped cuprate superconductors showed a Cu *K* edge shift as a funcion of carrier concentration. For the cuprates it is well established that charge carrier doping is fundamental for the appearance of superconductivity and XANES can indeed probe changes of the local electronic structure of the absorption atom. In general, red- (blue-) shifts are observed

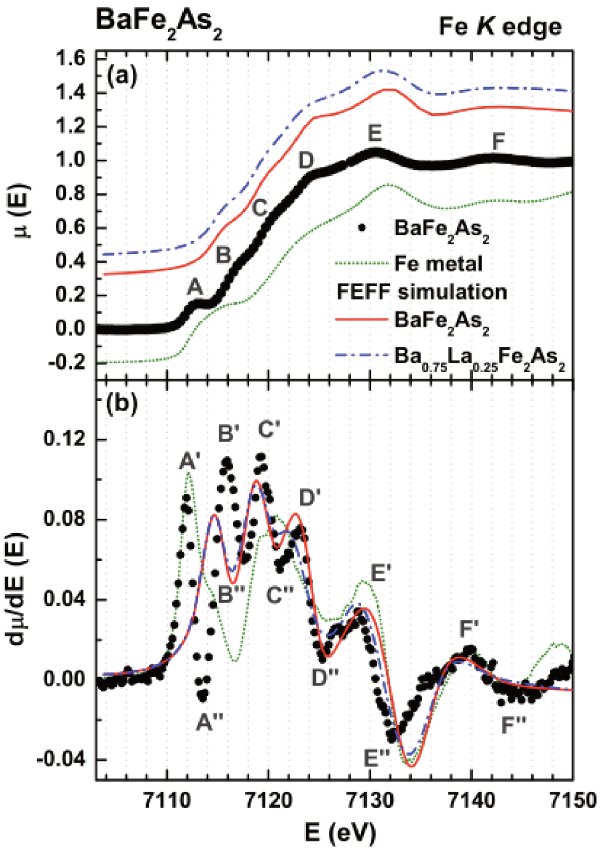

Figure 5.8: a) Observed and calculated Fe K edge XANES spectrum of pure $BaFe_2As_2$; calculated spectrum for the model compound $Ba_{0.75}La_{0.25}Fe_2As_2$ to simulate the effects of true electron doping. Prominent peaks and shoulders are indicated in $A-F$. The calculated spectra are shifted vertically for better visualization. (b) Energy first derivative of the spectra shown in (a). Derivative maxima and minima are represented as $A'-F'$ and $A''-F''$, respectively. The reference Fe metal XANES spectrum is also shown for comparison.

for electron- (hole-) doping. The lack of an Fe K edge absorption threshold energy shift in Co substituted $BaFe_2As_2$ implies that Co is not charge doping the Fe ions, which were thought to be somewhat responsible for the superconductivity.

In order to quantify the expected effects of the true Fe electron doping on the XANES spectrum of $BaFe_2As_2$, the relative shift of the simulated B' - E' features in Fig.5.8(b) were computed for the model system $Ba_{1-x}La_xFe_2As_2$. To account for the La substitution within the cluster of atoms in FEFF, Ba ions were randomly replaced by La while keeping the desired stoichiometry in each neighboring layer. The same atomic positions of the pure compounds were employed. The simulated spectrum for $x = 0.25$ is given in Figures 5.8(a) and 5.8(b). The calculated energy shift of these features as a function of x is displayed in Fig. 5.10 as empty symbols and solid spline lines.

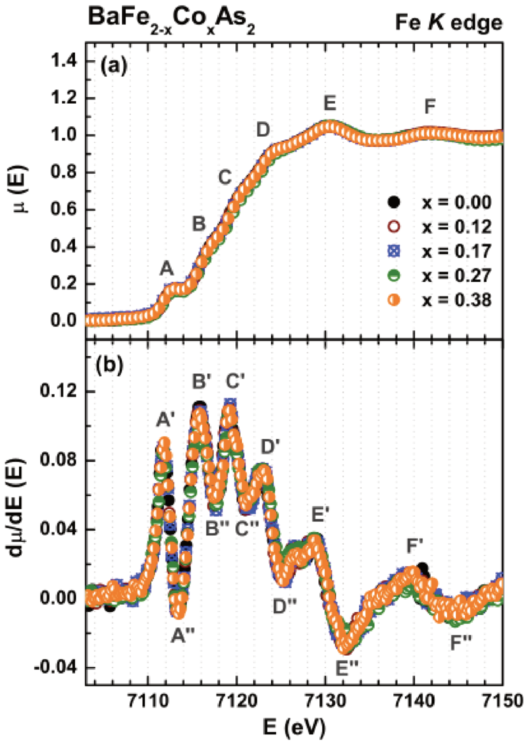

Figure 5.9: (a) Normalized Fe K edge XANES spectra of $BaFe_{2-x}Co_xAs_2$ at room T. Prominent peaks and shoulders are indicated $A - F$. (b) First derivative of the XANES spectra in (a). Derivative maxima and minima are represented as $A' - F'$ and $A'' - F''$, respectively.

These shifts are obtained relative to the Fe K edge XANES simulations for pure $BaFe_2As_2$. It is clear that a redshift of some of the features is computed under electron doping, most notably the D' and E' features. As already mentioned, such red shifts under electron doping are largely expected based on previous K edge XANES experiments on other transition-metal compounds. It is worth mentioning that the calculated positions B' and C' show much less influence of electron doping, indicating a non rigid shift of the Fe K edge under doping. In any case, the contrast between the observed constant positions of the D' and E' features under Co substitution and the calculated redshifts of up to ~ 1 eV for $x = 0.50$ electron doping (see Fig. 5.10) unambiguosly demonstrates that Co substitution does not induce Fe valence changes in $BaFe_2As_2$. We also performed FEFF calculations for $BaFe_{2-x}Co_xAs_2$ ($x = 0.5$) and they showed that the extra Co electron stays entirely within the muffin-tin sphere of the substitute atom, consistent with Ref.

[10]. The closed symbols and dashed lines in Fig. 5.10 show the computed shift for $x = 0.5$ and a linear extrapolation for $0 < x < 0.5$, respectively. No significant shifts of the Fe K edge features are calculated, in agreement with our experimental results.

Co substitution has an important impact on the Fermi surface, consistent with a shift of the chemical potential by Co substitution in a first approximation. This fact is complementary, rather than contradictory, with the constant Fe electronic occupation predicted in Ref. [10] and demonstrated here. As the electronic states close to the Fermi level show mixed Fe and Co 3d character, even if a tuning of the chemical potential may occur, this does not change the total electronic occupation of the Fe ion.

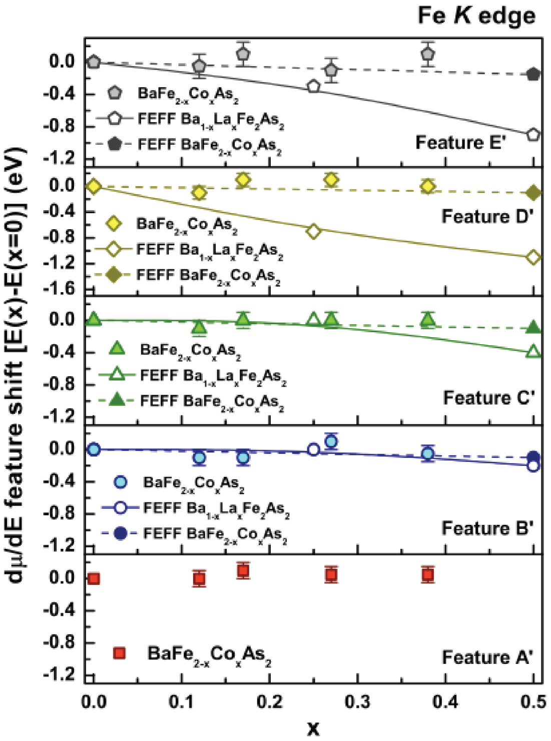

Figure 5.10: Fe K edge XANES spectra first derivative A', B', C', D' and E' feature (see Fig. 5.9) positions as a function of Co substitution in $BaFe_{2-x}Co_xAs_2$. The solid spline lines are the expected redshifts by true electron doping, obtained by simulated XANES spectra $Ba_{1-x}La_xFe_2As_2$ ($x = 0.00, 0.25,$ and 0.50) model compounds. The dashed lines are the expected shifts obtained by a linear extrapolation using calculated XANES spectrum of $BaFe_{1.5}Co_{0.5}As_2$.

In fact, Electron Spin Resonance (ESR) results, discussed in the next section, suggest that chemical substitution changes the occupation of the different Fe 3d orbitals by changing the Fe local structure. This modification alters the Fermi surface and destabilizes the SDW phase.

5.2 ESR Measurements

Electron spin resonance (ESR) is a powerful spin probe (see Cap. 2, for details) that has been used to study the spin dynamics in these compounds. However, up to date, the ESR experiments have been focused on Eu-based samples far from diluted regime. For instance, Eu^{2+} ESR data in $EuFe_2As_2$ single crystals indicate a spatial confinement of the conduction electrons (*ce*) to the FeAs layers below T_{SDW} due to the change in the ESR linewidth from a typical metallic behavior (i.e., a linear Korringa-type increase above T_{SDW} to a magnetic insulating behavior, where dipolar and crystalline electrical field effects dominate [42]. In hole doped $Eu_{0.5}K_{0.5}Fe_2As_2$, where the SDW phase is completely suppressed and SC arises for $T \leq 32\,K$, a Korringa increase also occurs for $T > T_c$ [43]. For the electron doped $EuFe_{2-x}Co_xAs_2$, the Korringa rate (KR), T_{SDW} and T_c all scale with x [44]. More recently, a report on polycrystalline $EuFe_{2-x}Co_xAs_2$ also shows that the Korringa rate decreases with Co-doping [45]. However, in the Eu-concentrated compounds, the Eu^{2+}-Eu^{2+} spin interaction always represents an important contribution to the ESR data and to the global properties of the compounds. Therefore, it is crucial to extrapolate such studies to a Eu^{2+} diluted regime in a host compound of great interest. $BaFe_2As_2$ is an obvious choice since it presents $T_{SDW} = 139$ K and, as reported in the last section, SC can be tuned by pressure and doping. In fact, the highest SC T_c within the AFe_2As_2 series is found in $(Ba,K)Fe_2As_2$ (38 K) [113].

Motivated by this scenario, we started studying flux grown $Ba_{1-x}Eu_xFe_2As_2$ ($x_{nominal} = 0.01, 0.1, 0.2, 0.3, 0.5, 0.7, 0.9, 1.0$) by means of magnetic susceptibility, heat capacity, resistivity and ESR experiments. To increase the signal to noise ratio, mainly larger Sn-flux crystals were used in the ESR experiments. Selected concentrations were also grown from In- and self (FeAs)-fluxes [118, 119]. The crystals were checked by x-ray powder diffraction and submitted to elemental analysis using a commercial Energy Dispersive Spectroscopy (EDS) microprobe. As previously reported, the Sn-flux crystals were found to have a small amount of Sn-incorporation varying from $0.1 - 1.0$ Atom % along the series [120]. No In-incorporation was detected in the In-flux crystals. From the EDS analysis we also extracted the actual Eu-x that are used throughout the text.

To better illustrate the evolution of the physical properties along the series, we present the data of four representative Eu concentrations. Fig.5.11a displays the T-dependence of the specific heat per mole divided by temperature. For $x = 0.95$, two sharp peaks indicate both SDW and AFM transitions at 187 K and 18 K, respectively, which are slightly down-shifted when compared to 189 K and 19 K in $EuFe_2As_2$. As x decreases, T_N is further suppressed and the lowest detectable $T_N = 0.5\,K$ is obtained for x= 0.55 (inset). Interestingly, even for $x < 0.5$, where AFM is no longer present, we observed a rise in C/T at low-T which is not found for $x = 0$, indicating that the Eu^{2+} ions are responsible for it.

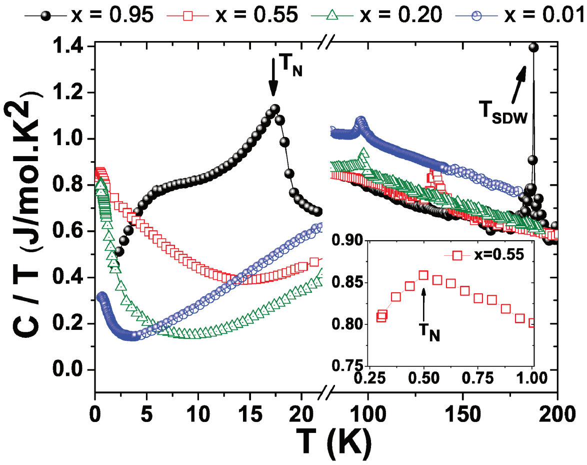

Figure 5.11: Specific heat per mole versus temperature of the $Ba_{1-x}Eu_xFe_2As_2$ series. The inset shows low-T data for $x = 0.55$

Fig.5.12b shows the magnetic susceptibility as a function of temperature for $H = 1\,\mathrm{kOe}$ parallel to the ab-plane. For all samples, $\chi(T)$ can be fitted to a Curie-Weiss law plus a T-independent Pauli term, $\chi(T) = \chi_0 + \mathrm{C}/(T\text{-}\theta_{CW})$ (solid lines). We obtained $\chi_0 = 2(1) \times 10^{-3}$ emu/mol.Oe (upper inset of Fig. 5.12) and an effective moment $\mu_{eff} \approx 8\mu_B$ for Eu^{2+} ions for all x values. The SDW transition is nearly indistinguishable in the Eu-rich samples due to the Eu^{2+} large magnetic contribution but it can be seen as a kink in $\chi(T)$ for samples in the Eu-diluted regime (bottom inset of Fig. 5.12).

The T-dependence of the normalized electrical resistivity is shown in Fig.5.13. The room-T value of $\rho(T)$ and RRR ratio vary in the range $0.2 - 0.8$ mΩ.cm and $0.02 - 2.8$, respectively. For $x > 0.5$, a metallic behavior is observed down to T_{SDW} where a sudden drop can be identified in the curves. For $x \lesssim 0.5$, $\rho(T)$ increases at T_{SDW} as typically found for doped samples in the $BaFe_2As_2$ systems [4].

Fig. 5.14 shows the X-Band ESR spectra at T$=$ 300 K and H$||ab$ for $Ba_{1-x}Eu_xFe_2As_2$ single crystals. A single Eu^{2+} ESR resonance is observed for all x values. The ESR lines for $x \geq 0.2$ have an asymmetric Dysonian character (skin depth smaller than the sample size [75]). However, for $x < 0.2$, the spectra clearly become more symmetric, consistent with the fact that $BaFe_2As_2$ has smaller conductivity than $EuFe_2As_2$. In addition, it is evident that the ESR linewidth (ΔH) is much smaller in the Eu-diluted regime, consistent with the decreasing of Eu^{2+}- Eu^{2+} spin interaction contribution to the ESR ΔH.

From fitting to the resonances using the appropriate admixture of absorption and dispersion (solid lines), we obtained both ΔH and g-value T-dependence, shown in Fig. 5.15. In the Eu-rich

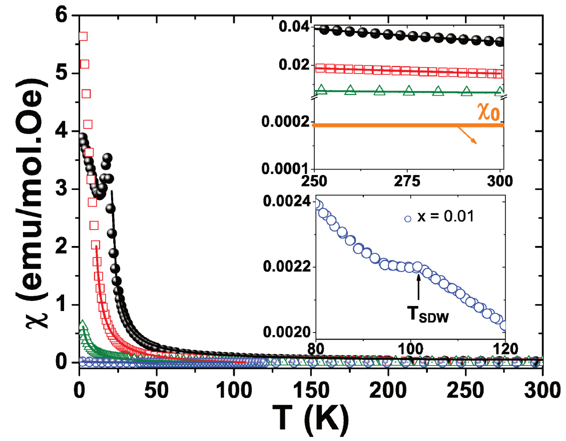

Figure 5.12: Magnetic susceptibility as a function of temperature of the $Ba_{1-x}Eu_xFe_2As_2$ series. The insets show the high-T data and T_{SDW} for $x = 0.01$, respectively.

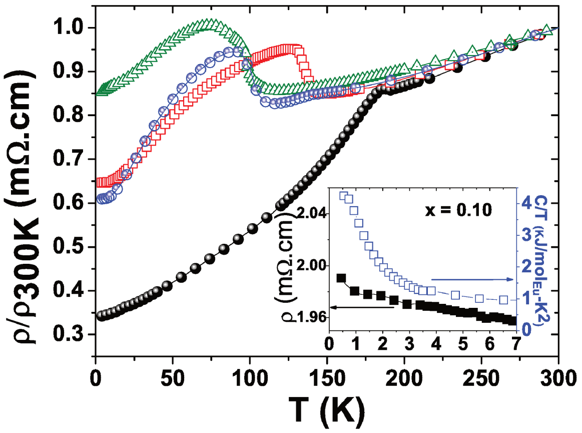

Figure 5.13: Normalized electrical resistivity versus temperature of the $Ba_{1-x}Eu_xFe_2As_2$ series. The inset shows the low-T data upturn for $x = 0.10$.

extreme, we observe an isotropic linear (Korringa-type) increase of ΔH with increasing-T for T > T_{SDW}. From linear fits to $\Delta H(T)$ for T > T_{SDW} and $x \geqslant 0.2$, we extracted the values of the Korringa rate $b = \Delta H/\Delta T$. It is evident that b systematically decreases with decreasing x along the series for $x \geqslant 0.2$. Consistently, the $b = 6.3(5)$ Oe/K found for the $x = 0.95$ sample is slightly smaller than the reported $b = 6.5 - 8.0$ Oe/K values for $EuFe_2As_2$ [42, 44].

However, for $x < 0.2$ we observe no Korringa behavior. Instead, $\Delta H(T)$ decreases with

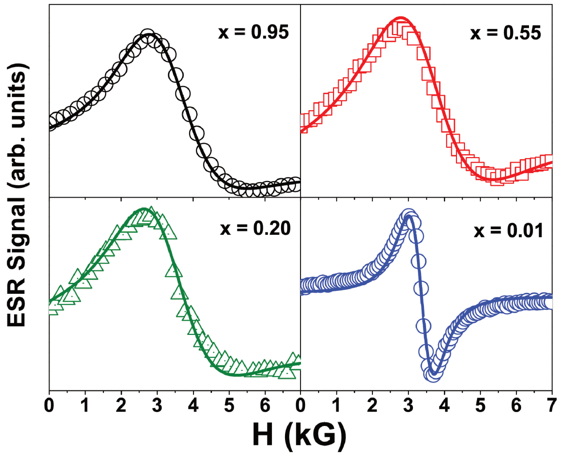

Figure 5.14: X-Band spectra at T= 300 K for $H||ab$ for the $Ba_{1-x}Eu_xFe_2As_2$ series.

increasing-T, suggesting a non trivial regime, clearly distinct from a Fermi liquid. For $x = 0.01$ we show in Fig. 5.15a that this intriguing behavior was found for crystals grown from different fluxes.

Fig.5.15b displays the T-dependence of the Eu^{2+} ESR g-value for T $>$ 200 K and $H||ab$. As the crystals are very thin platelets, we use the data for $H||ab$ that allow us to neglect the demagnetization factors to determine the g-values [121]. As previously reported for $EuFe_2As_2$, $Eu_{0.5}K_{0.5}Fe_2As_2$ and $EuFe_{2-x}Co_xAs_2$, we found a T-independent $g \approx 2$ for the Eu^{2+} ESR lines in $Ba_{1-x}Eu_xFe_2As_2$ for $T > T_{SDW}$. In fact, the high-T Eu^{2+} g-values are also independent of x. For the samples with narrower ESR ΔH ($x < 0.20$) we were able to determine with higher precision a g-value of 2.04(2). This is a more accurate g-value than those published for the concentrated compounds, which possess a much broader ΔH. As it can be seen in Fig.5.15b, the g-value of 2.04(2) is a reasonable mean g-value for all x in this T-range. However, although this is a reasonable approximation it must be taken cautiously due to the limitations in our analysis for the broader lines.

From the data in Figs.5.11-5.15, we extracted the phase diagram in Fig.5.16. Both T_{SDW} and T_N decrease with $1 - x$ and for $x < 0.5$ the Eu^{2+} AFM transition is no longer observable. Interestingly, the decreasing Korringa rate follows qualitatively the suppression of T_{SDW} before it disappears at $0.10 < x_c < 0.20$.

To gain a microscopic understanding of this evolution, a detailed analysis of the ESR data is needed. We consider the simplest scenario for the treatment of the exchange interaction, $J_{fs}\mathbf{S}.\mathbf{s}$, between a localized Eu^{2+} $4f$ electron spin ($\mathbf{S}$) and the free *ce* spins ($\mathbf{s}$) of the host metal, where "*bottleneck*", "*dynamic*", electron-electron correlation effects, **q**-dependence exchange and multi-

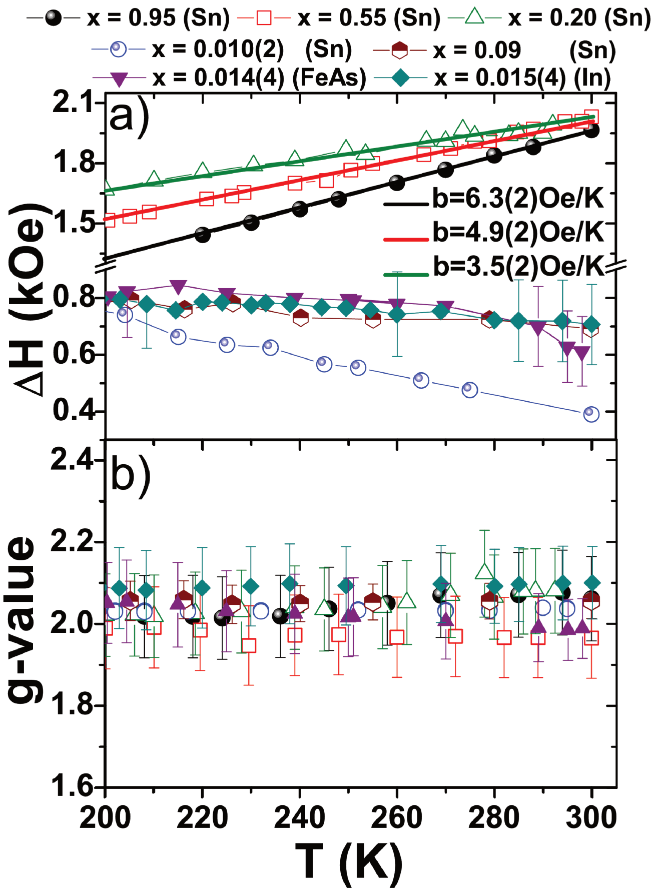

Figure 5.15: T- dependence of the a) linewidth ΔH and b) g-value. The data for x= 0.01 (In) and x= 0.01 (FeAs) were taken in powderized crystals and several small crystals, respectively.

ple bands effects are not present [122]. Those are reasonable assumptions because when "*dynamic*" effects are present the g-values are usually strongly T-dependent and when the bottleneck effect is relevant the Korringa rate decreases with increasing concentration of the magnetic ions [122]. None of these effects are observable in our ESR data of Fig. 5.15 for the studied T-range.

Therefore, in this simple case, the ESR g-shift (Knight shift) [123] and the Korringa rate [124] can be written as:

$$\Delta g = J_{fs}\; \eta\left(E_F\right), \tag{5.1}$$

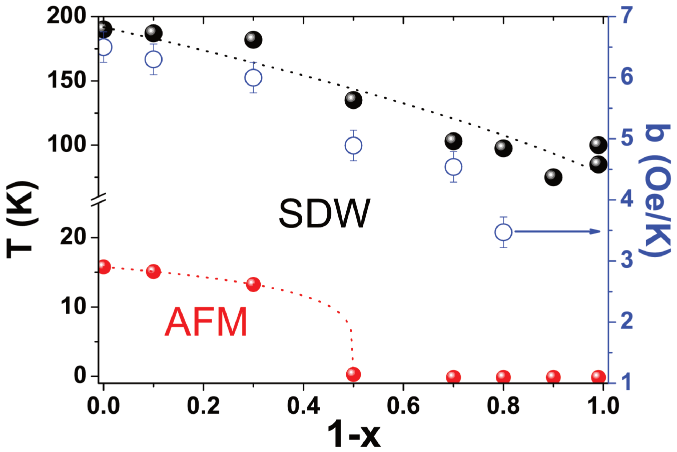

Figure 5.16: $Ba_{1-x}Eu_xFe_2As_2$ phase diagram displaying the Eu^{2+} AFM transition temperature (red circles), the Fe^{2+} SDW transition temperature (black circles), and the Korringa rate b (blue open circles).

and

$$\frac{d\left(\Delta H\right)}{dT} = \frac{\pi k}{g\mu_B}\ J_{fs}^2\ \eta^2\left(E_F\right), \tag{5.2}$$

where J_{fs} is the effective exchange interaction between the Eu^{2+} local moment and the *ce* in the absence of *ce* momentum transfer [125], $\eta(E_F)$ the "*bare*" density of states (DOS) for one spin direction at the Fermi surface (FS), k the Boltzman constant, μ_B the Bohr magneton and g the Eu^{2+} g-value. When Eqs 1-2 are applicable, the relation $\frac{d(\Delta H)}{dT} = \frac{\pi k}{g\mu_B}\ (\Delta g)^2$ holds. Using the g-value of Eu^{2+} in insulators as 1.993(2), $(\pi k/g\mu_B) = 2.34$ x10^4 Oe/K and replacing $\Delta g \approx 0.05(2)$, we found a $b \approx 150(50)$ Oe/K for the Eu^{2+} resonance [74].

That value is much larger than the measured values of b for $x \geqslant 0.20$ (see Figs. 5.15-5.16). Therefore, the approximations made in Eqs. 5.1-5.2 are not valid for these compounds and we have to consider a $\mathbf{q}$-dependent exchange interaction, $J_{fs}(\mathbf{q})$, and perhaps conduction electron-electron $(e-e)$ correlations [126, 127]. $J_{fs}(\mathbf{q})$ is the Fourier transform of the spatially varying exchange.

Considering only the wave-vector dependence of the exchange interaction, $J_{fs}(\mathbf{q})$, the exchange parameters in Eqs. 1-2 become $J_{fs}(\mathbf{0})$ and $< J_{fs}^2(\mathbf{q}) >$, respectively. At the Eu^{2+} site the g-shift probes the *ce* polarization ($\mathbf{q}= 0$) and the Korringa rate the *ce* momentum transfer ($0 \leq \mathbf{q} \leq 2k_F$) averaged over the FS [125].

To evaluate the possible contribution of $e-e$ correlations in our ESR data, we need to estimate the Pauli magnetic susceptibility [126, 127]. The electronic contribution to the heat capacity for the $BaFe_2As_2$ compound is reported to be $\gamma = 16$ mJ/mol-K^2 [89]. Assuming a free *ce* gas model for $BaFe_2As_2$, $\gamma = (2/3)\pi k^2 \eta(E_F)$, we calculate a DOS at the Fermi level (E_F), $\eta(E_F) =$ 3.34 states/eV mol-spin. Then, one finds an electronic spin susceptibility, $\chi_e = 2{\mu_B}^2\eta(E_F)$, of $\approx 3 \times 10^{-4}$ emu/FU. That is one order smaller than the $\chi_0 = 2(1) \times 10^{-3}$ emu/mol-Oe measured for all compounds (Fig. 5.12). This suggests that an *e*-*e* exchange enhancement contributes to the *ce* spin susceptibility in $Ba_{1-x}Eu_xFe_2As_2$. It is known that in the presence of such an enhancement, the host metal *ce* spin susceptibility can be approximated by $\chi_0 = 2\ \mu_B^2\ \frac{\eta(E_F)}{1-\alpha}$, where α accounts for the $e-e$ interaction, (1 - α)$^{-1}$ is the Stoner enhancement factor, and $\eta\,(E_F)$ is the "*bare*" DOS for one spin direction at E_F. An α value of $\approx 0.85(5)$ is estimated assuming that the enhancement in χ_0 is only due to the $e-e$ interaction.

In the presence of $e-e$ exchange enhancement and a **q**-dependence of the exchange interaction, $J_{fs}(\mathbf{q})$, the *g*-shift (Eq.5.1) and the thermal broadening of the linewidth (Eq. 5.2) may be re-written as:

$$\Delta g = J_{fs}(\mathbf{0})\ \frac{\eta\,(E_F)}{1-\alpha}\ , \tag{5.3}$$

and

$$\frac{d\,(\Delta H)}{dT} = \frac{\pi k}{g\mu_B} < J_{fs}^2(\mathbf{q}) > \eta^2\,(E_F)\ \frac{K(\alpha)}{(1-\alpha)^2}\ , \tag{5.4}$$

where $K(\alpha)$ is the Korringa exchange enhancement factor [76, 77]. From ref.[77], $\alpha \approx 0.85(5)$ corresponds to K(α) = 0.2(1). Then, using $\eta(E_F) = 3.34$ states/eV mol-spin, $\Delta g = 0.05(2)$, $\alpha \approx 0.9$, K(α) = 0.2(1) and *b* values, we extracted $J_{fs}(0) = 2(1)$ meV for all *x* values and $(< J_{fs}^2(\mathbf{q}) >^{1/2}) = 2.0(8), 1.5(8), 1.0(8)$ for $x = 0.95$, 0.55, 0.20, respectively.

It is evident that the relative value of $< J_{fs}^2(\mathbf{q}) >^{1/2}$ is clearly diminishing with decreasing *x* for $Ba_{1-x}Eu_xFe_2As_2$ for $x \geqslant 0.20$ even though we have a large uncertainty in its exact numerical value. $J_{fs}(q)$ is the Fourier transform of the spatially varying exchange and therefore its decreasing value implies that (*i*) the electron bands with appreciable overlap with the Eu^{2+} 4*f* states are becoming more anisotropic (less *s*-like) and that (*ii*) they are, in average, further away from the Eu^{2+} sites in real space. As Eu^{2+} and Ba^{2+} have the same valence, this evolution of the electronic structure is likely to be caused by subtle changes in the tetragonal crystal structures (and consequently in the Fe-As bonds) of $EuFe_2As_2$ ($c/a = 3.1006$) and $BaFe_2As_2$ ($c/a = 3.2849$) [128]. Band structure calculations and angle resolved photoemission spectroscopy (ARPES) experiments for $BaFe_2As_2$ and $EuFe_2As_2$ have shown that there are differences in the FS topology between the two compounds even though the Fe 3*d* DOS are nearly the same close to E_F [129, 130]. Interestingly, local-density approximation (LDA) calculations show that for slightly smaller Fe-As distances there is a down-shift of the Fe $3d_{x^2-y^2}$ hole band near Γ (i.e., an increase in the $x^2 - y^2$ occupation) leading to a suppression of the Fe magnetism [130]. Moreover, ARPES experiments have shown that the size of the hole pocket near Γ in $EuFe_2As_2$ is $2-3$ times larger than in $BaFe_2As_2$ (Fig. 5.17), again in agreement with an increasing xy occupation in the Ba-rich extreme. In fact, our results in quantum oscillations (see Section 3.3.2) evidentiate larger Fermi surfaces in the $EuFe_2As_2$ compound. In the ESR data, these FS changes are reflected in the evolution of $J_{fs}(\mathbf{q})$ with x.

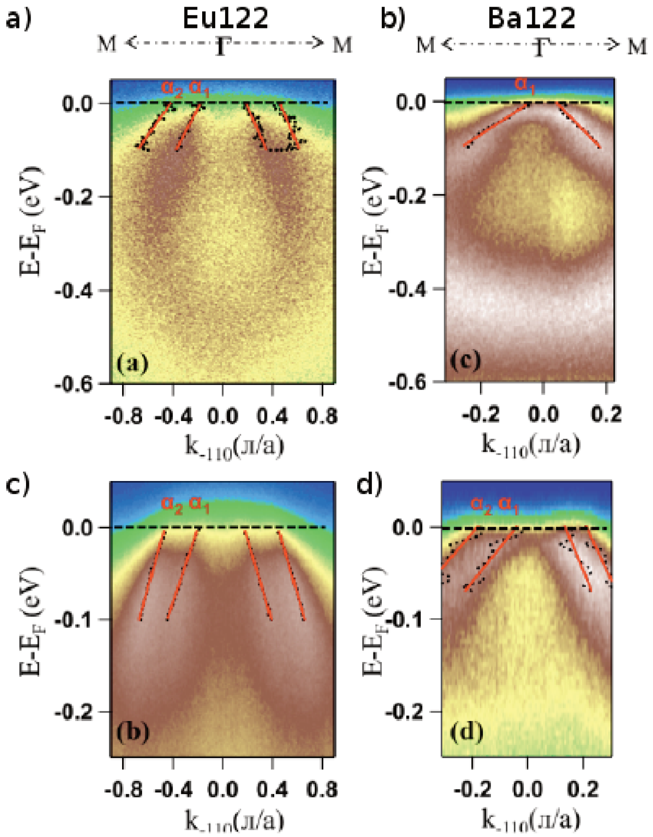

Figure 5.17: ARPES dispersion for (a) $BaFe_2As_2$ and (b) $EuFe_2As_2$ at 300 K and (c-d) at 30 K. Figure extracted from [129].

Furthermore, changes in the tetrahedron shape directly affect the crystal field at the Fe site and can tune the orbital contributions to the Fermi surface. In this manner, the observed behavior suggests a partial localization of the itinerant Fe $3d$ bands at the FeAs plane, (in other words, an increase in the xy occupation) as we suppress the SDW phase from the Eu to the Ba-rich extreme.

It is worth noting that our scenario is in complete agreement with the data on the concentrated Eu regime in the literature. A slower Korringa rate b also has been obtained when K or Co were introduced in $EuFe_2As_2$ [43, 44, 45].

In addition, DFT+DMFT calculations show that when correlations become important, such as in $BaFe_2As_2$, the changes in the physical properties are mainly due to the variation in two key structural parameters: the iron-pnictogen distance and the tetraedron shape. The first one controls the overlap between iron and pnictogen atoms and hence makes iron electron more localized (itinerant) with increasing (decreasing) distance. The second parameter controls the crystal field levels, which in turn controls the orbital occupancies. A deviation from ideal tetrahedron (109.5°) enchances the crystal field splitting between $t2g$ and eg orbitals and therefore generates charge transfer from $t2g$ to eg orbitals. Orbital differentiation becomes crucial in this case since the xy orbital loses most charge among the $t2g$'s orbitals. Thus, it starts to play a special role due to the kinetic frustration: the xy orbital is effectively insulating since the effective nearest neigbour Fe-Fe $t_{xy,xy}$ hopping vanishes [23]. In this manner, decreasing iron-pnictogen distances and deviations from the ideal tetrahedron cause an increase of the xy orbital occupancy, which in turn weakens the magnetic moment. These effects can be observed in the Fermi surface since an increase in the xy orbital occupancy results in the decrease of the hole pocket size. In fact, angle resolved photoemission spectroscopy (ARPES) show that the size of the hole pockets near Γ in $EuFe_2As_2$ is $2-3$ times larger than in $BaFe_2As_2$, in agreement with the fact that the hole carrier mobility dominates in $EuFe_2As_2$ as compared to $BaFe_2As_2$ in the paramagnetic phase [129].

Now we turn our attention to the more diluted regime ($x < 0.20$). The observed decreasing of $< J_{fs}^2(\mathbf{q}) >^{1/2}$ for $x \geqslant 0.20$ may suggest that the Korringa rate for the Eu^{2+} diluted regime will be very small and the Eu^{2+} ESR ΔH would be T-independent in this T-interval. However, this mechanism can not explain the ΔH broadening observed for T> T_{SDW} in the $x < 0.20$ samples as T is lowered.

We seek a possible explanation for this behavior by further analyzing the low-T $\rho(T)$ and heat capacity data for the samples in the Eu^{2+} low-x regime. The inset of Fig. 5.13 shows such data for the $x = 0.1$ sample. We speculate that the observed behavior is reminiscent of Kondo single impurity regime with a Kondo temperature $T_K \approx 5 - 10$ K. As such, this result suggests that for $x < 0.20$, any kind of inter-site Eu^{2+}-Eu^{2+} short range magnetic correlation disappears leading to the emergence of intra-site only AFM coupling of the Eu^{2+} $4f$ and the ce. In this Kondo-like interaction, the ce tend to screen the localized Eu^{2+} ions leading to faster relaxation and ΔH broadening as T decreases. This effect would become even more dramatic at lower-T if the ΔH were not already strongly enhanced by the presence of the SDW phase in all studied samples. Interestingly, the claim for the presence of Kondo single impurity effect interaction for the Eu^{2+} ions in the 122 system has also been made in the case of $EuFe_2P_2$ [131].

In order to unambiguously establish the increase of localization of the $3d$ Fe electrons at the FeAs plane as the magnetic SDW phase is suppressed in 122-systems, we have then studied the series of $Ba_{1-x}Eu_xFe_{2-y}TM_yAs_2$ high quality single crystals (TM stands for the transition metals Co, Cu, Mn, Ni, and Ru) grown by In-flux. In this case, we can probe both Ba and FeAs planes through substitution with Eu^{2+} and Mn^{2+}/Cu^{2+}, respectively. We use the Eu concentration $x_{Eu} = 0.20$ as a reference compound to probe how the spin dynamics evolves as a function TM substitution. We choose this compound because it is the one with lowest Eu concentration that still has a Korringa relaxation.

Starting with the physical properties of the studied single crystals, Fig. 5.18a displays the T-dependence of the normalized electrical resistivity. Room-T values of $\rho(T)$ varies in the range $0.2 - 0.8$ mΩ.cm and $0.02 - 2.8$. For $x = 0.2$, the Eu reference compound, a metallic behavior is observed down to T_{SDW} where a sudden drop can be identified in the curve at 137 K. As we substitute Fe by the transition metals $y^{Ru} = 0.01$, $y^{Ni} = 0.11$, $y^{Cu} = 0.09$, and $y^{Co} = 0.12$ we observe a suppression of this SDW phase with smaller transition temperatures of 135 K, 102 K, 98 K, and 86 K, respectively. Except for the ruthenium compound, which has very low transition metal substitution, the resistivity starts to increase at T_{SDW} as typically found for doped samples in the $BaFe_2As_2$ systems [4]. For the samples with $x = 0.0$ we also observe a SDW phase suppression in comparison with the parent compound $BaFe_2As_2$ ($T_{SDW} = 140$ K): for $y^{Mn} = 0.1$ $T_{SDW} = 78$ K and for $y^{Cu} = 0.1$ the SDW phase is fully suppressed and superconductivity occurs at $T_c = 3.8$K (inset of Fig. 5.18). Superconductivity also emerges for Co and Ni substitutions in the europium compounds (x ~ 0.2) with $T_c = 22$K and 6K, respectively (inset of Fig. 5.18a).

Fig.5.18b shows the magnetic susceptibility as a function of temperature for $H = 1$ kOe parallel to the *ab*-plane. For all samples, $\chi(T)$ can be fitted to a Curie-Weiss law plus a T-independent Pauli term, $\chi(T) = \chi_0 + C/(T - \theta_{CW})$ (solid lines). We obtained an effective moment $\mu_{eff} \approx 8\mu_B$ for Eu^{2+} ions for all y values and an electronic spin susceptibility of $\chi_0 = 2(1) \times 10^{-3}$ emu/mol-Oe for all compounds. The SDW transition is nearly undistinguishable in the Eu-rich samples due to the Eu^{2+} large magnetic contribution. The inset of Fig. 5.18b shows the superconducting transition at low-field (H = 20 Oe).

Fig.5.18c shows T-dependence of the specific heat per mole divided by temperature for the selected single crystals. For $x = 0.2$, the reference compound, one sharp peak indicates the spin-density wave (SDW) transition at 137 K (green arrow). As we substitute Fe by the transition metals we observe a suppression of this SDW phase (other arrows). Interestingly, there is a rise in C/T at low-T which is not found for $x = 0$, as we observed before.

Fig. 5.19 shows the X-Band ($\nu \sim 9.5$ GHz) ESR spectra at T= 300 K. A single ESR resonance is observed for all x and y values. The ESR lines have an asymmetric Dysonian character (skin depth smaller than the sample size [75]). However, to increase signal to noise ratio, we have powdered the samples and consequently the lineshapes have become more symmetric (Lorentzian-like).

From fitting to the resonances at various-T using the appropriate admixture of absorption and dispersion (solid lines), we obtained both ΔH and g-value T-dependence, shown in Fig. 5.20. For

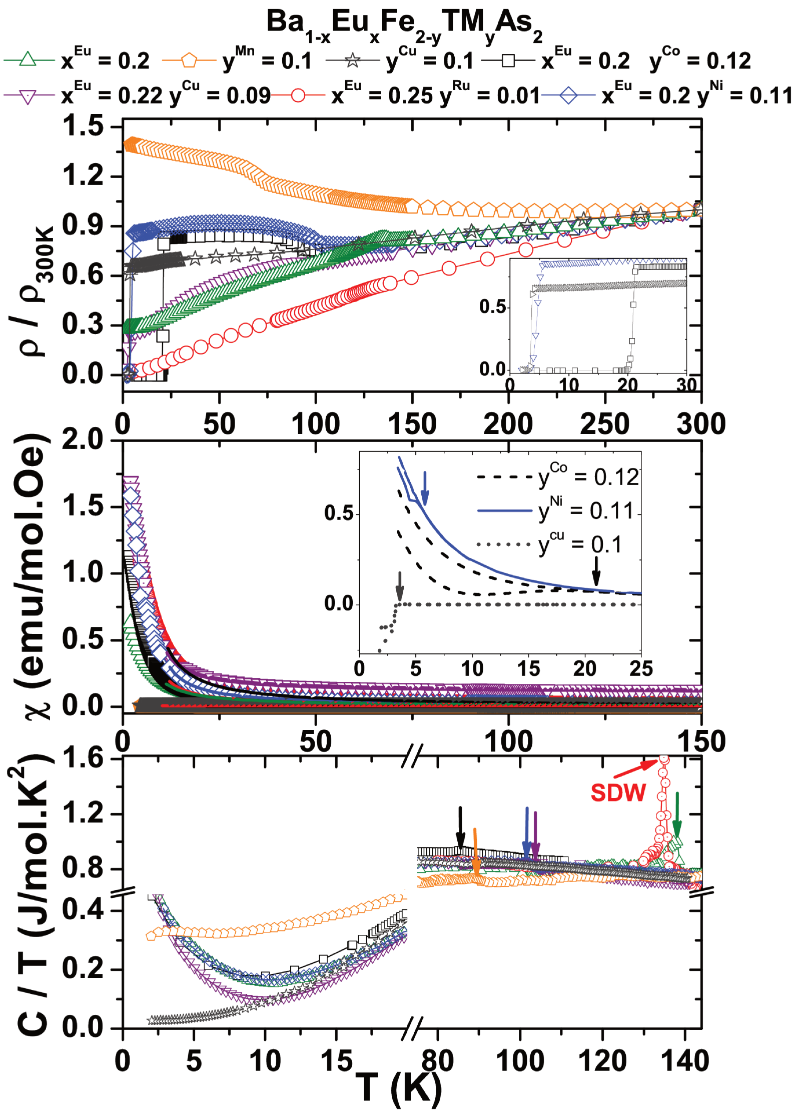

Figure 5.18: Physical properties of $Ba_{1-x}Eu_xFe_{2-y}TM_yAs_2$ single crystals (TM for transition metals Co, Cu, Mn, Ni, and Ru). The inset shows a) the resistivity going to zero at the superconducting transition, b) zero-field cooling/field cooling magnetic susceptibility.

the Eu^{2+} resonance, we observe a nearly isotropic linear (Korringa-type) increase of the ΔH with increasing-T for T > T_{SDW}. From linear fits to the $\Delta H(T)$ for T > T_{SDW} we extracted the values of the Korringa rate $b = \Delta H/\Delta T$. It is evident that b systematically decreases with the transition metal substitution y. On the other hand, for the Mn^{2+}/Cu^{2+} resonances there is a competition between spin-spin interaction (that broadens the linewidth as we lower the temperature) and spin-conduction electron interaction. In the high-temperature range the Korringa relaxation dominates

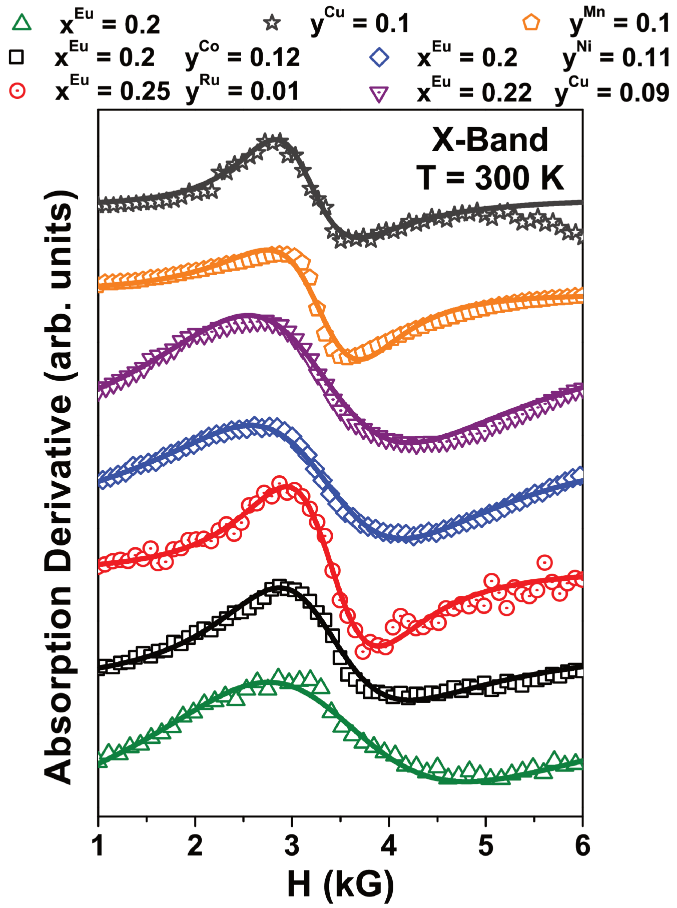

Figure 5.19: X-Band ESR lines at T= 300 K for selected $Ba_{1-x}Eu_xFe_{2-y}TM_yAs_2$ single crystals.

and we obtain $b = 1.5$ and 3.5 for Mn^{2+} and Cu^{2+} resonances, respectively (inset of Fig. 5.20a).

Fig. 5.20b displays the T-dependence of the Eu^{2+} ESR g-value for $T > 150$ K. As previously reported for $EuFe_2As_2$, $Eu_{0.5}K_{0.5}Fe_2As_2$ and $EuFe_{2-x}Co_xAs_2$, we found a T-independent $g \approx 2$ for the Eu^{2+} ESR lines in $Ba_{1-x}Eu_xFe_2As_2$ for T > T_{SDW}. In fact, the high-T Eu^{2+} g-values are also independent of x, within the error bars, and equal to 2.04(4). For the samples with narrower ESR ΔH (M = Co, Cu, and Ru) we were able to determine with higher precision a g-value of 2.05(3). This is a more accurate g-value than those published for the concentrated compounds, which displays a much broader ΔH. As it can be seen in Fig. 5.20b, the g-value of 2.05(3) is a reasonable mean g-value for all x in this T-range. As we obtained again an electronic spin susceptibility of $\chi_0 = 2(1) \times 10^{-3}$ emu/mol-Oe for all compounds the same arguments used on the previous experiments on $Ba_{1-x}Eu_xFe_2As_2$ are valid here. Consequently, we discharge the changes of DOS and the evolution of the electron-electron interaction as a dominant contribution for the Korringa suppression as a function of transition metal doping. We then extracted $J_{fs}(0) = 2(1)$ meV for all x and y values and the q-dependence ($< J_{fs}^2(\mathbf{q}) >^{1/2}$) shown in Table 5.2.

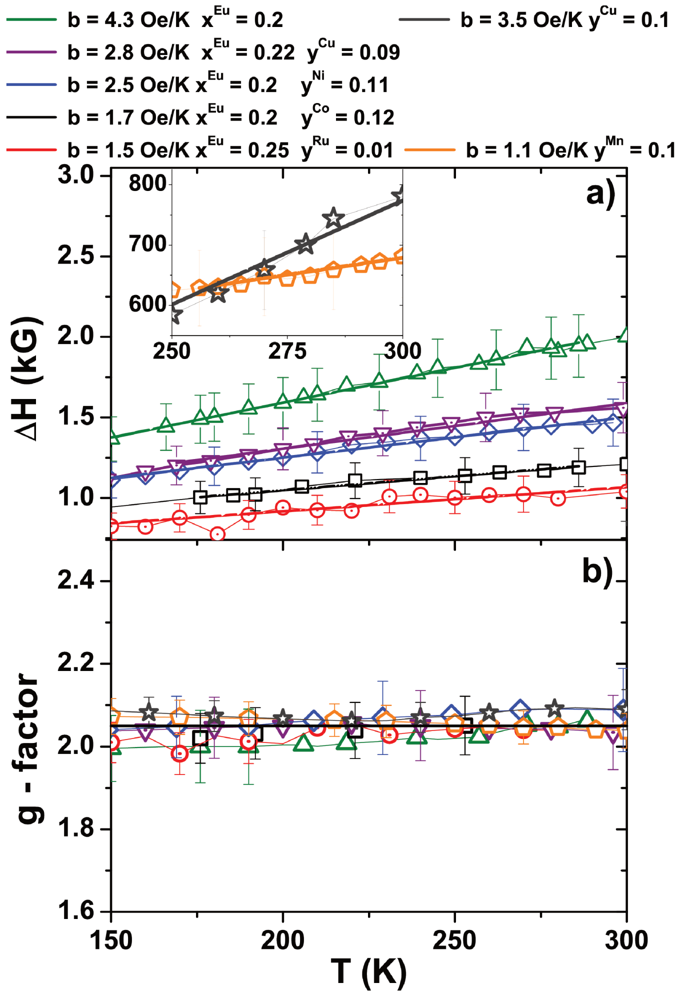

Figure 5.20: T- dependence of the a) linewidth ΔH and the b) g-value taken in powderized crystals

From the data in Figs. 5.18-5.20, we extracted the diagram in Fig. 5.21. When the ESR probe is out of plane (Fig. 5.21a) we observe that both T$_{SDW}$ and b values are suppressed with respect to their values for $Ba_{0.8}Eu_{0.2}Fe_2As_2$ as we substitute transition metals in the Fe site, as one would expect from the previous results. Furthermore, when the probe is in-plane (Fig. 5.21b) we observe exactly the opposite: the Korringa rate b increases as we suppress the SDW phase. These results together evidentiate that the relative value of $< J_{fs}^2(\mathbf{q}) >^{1/2}$ is clearly diminishing with increasing y when the probe is out of the FeAs plane in $Ba_{0.8}Eu_{0.2}Fe_{2-y}TM_yAs_2$. On the

Sample	ESR $\langle J^2(q)\rangle^{1/2}$ (meV)
$Ba_{0.8}Eu_{0.2}Fe_{1.9}As_2$	1.4(8)
$BaFe_{1.9}Cu_{0.1}As_2$	1.2(5)
$Ba_{0.78}Eu_{0.22}Fe_{1.91}Cu_{0.09}As_2$	1.1(5)
$Ba_{0.8}Eu_{0.2}Fe_{1.89}Ni_{0.11}As_2$	1.0(5)
$Ba_{0.8}Eu_{0.2}Fe_{1.88}Co_{0.12}As_2$	0.9(5)
$Ba_{0.75}Eu_{0.25}Fe_{1.99}Ru_{0.01}As_2$	0.8(5)
$BaFe_{1.88}Mn_{0.12}As_2$	0.7(5)
$Ba_{0.99}Eu_{0.01}Fe_{1.9}Co_{0.1}As_2$	0.5(4)

Table 5.2: Experimental ESR exchange interaction ($< J^2_{fs}(\mathbf{q}) >^{1/2}$) for the compounds in the $Ba_{1-x}Eu_xFe_{2-y}TM_yAs_2$ series.

other hand, $< J^2_{fs}(\mathbf{q}) >^{1/2}$ increases when the probe is in the FeAs plane. $J_{fs}(q)$ is the Fourier transform of the spatially varying exchange and therefore its decreasing value in the first case suggests that the electron bands with appreciable overlap with the Eu^{2+} $4f$ states are becoming more anisotropic (less s-like) and are, in average, further away from the Eu^{2+} sites in real space (more xy) as we suppress the magnetism and induce superconductivity. It is also clear that there is no unambiguous systematics between the magnitude of the SDW phase suppression and the magnitude of the Korringa rate suppression, specially for the ruthenium substitution. This is because the particularities in the bands' distortions can behave differently for each transition metal. For instance, if the substitution is not coherent, interference can occur between the $3d$ bands and consequently suppress more effectively b than T_{SDW}.

In summary, we employed a microscopic spin probe to study the suppression of the SDW magnetic phase in the $BaFe_2As_2$ compound by transition metal substitution. We evidenced that, independent on the transition metal, the $3d$ electrons localize at the FeAs plane due to the changes in structural parameters as we suppress the SDW phase. Decreasing Fe-As distances and deviations from the ideal tetrahedron angle decrease the crystal field splitting that in turn increases the occupancy of the Fe $3d_{xy}$ orbital, which is more insulating. Therefore, the itinerant SDW order and the ordered magnetic moment decreases and magnetic-mediated superconductivity can emerge.

Now that we have determined by an independent technique the exchange parameter $\langle J^2(q)\rangle^{1/2}$ and the g value, we are able to analyse our set of data considering the conventional Abrikosov-Gorkov (AG) formalism (equation 2.38):

$$\left|\frac{\Delta T_c}{\Delta c}\right| = \frac{\pi^2}{8k_B}\langle J^2(q)\rangle_{E_F}\eta(E_F)(g_J-1)^2J(J+1) \tag{5.5}$$

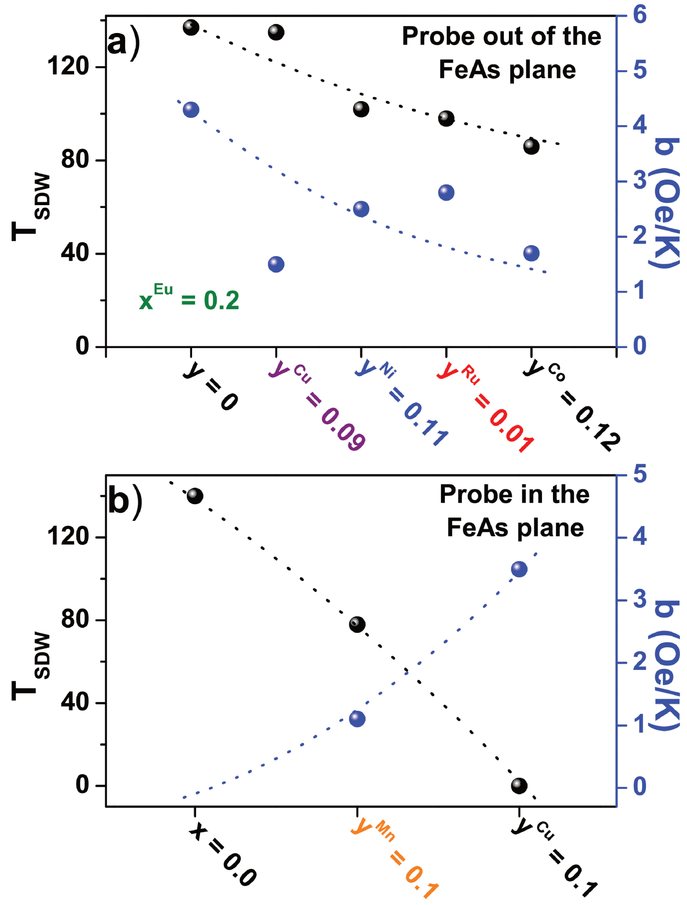

Figure 5.21: Dependence of T_{SDW} and b as a function of the (a) out-of-plane and (b) in-plane substitution in $BaFe_2As_2$.

From the EDS data we have the impurity concentration Δc (in %) and from the specific heat γ value we obtain the density of states. As discussed before, since the g-value does not change, the density of states is the same for all compounds. Therefore, from the experimental ΔT_c^{exp} we can extract the exchange $\langle J^2(q)\rangle^{1/2}$ from the AG equation and compare it with the experimental value from the ESR data. In the same way, from the experimental exchange $\langle J^2(q)\rangle^{1/2}$ we can extract the ΔT_c^{AG} and compare it with the experimental value. In the case of a conventional superconductor, these two values are equal and several ESR studies have verified that this is indeed the case [132, 133, 134]. However, in the case of unconventional superconductivity both magnetic and nonmagnetic impurities can influence the pairing mechanism. Moreover, the magnetic impurity may have an additional pair-breaking mechanism. Therefore, the AG formula does

Sample	c (%)	g	$\mid \Delta T_c^{exp} \mid$ K	$\mid \Delta T_c^{AG} \mid$ K	$\langle J^2(q)\rangle^{1/2}$ ESR (meV)	$\langle J^2(q)\rangle^{1/2}$ AG (meV)
$BaFe_{1.9}Cu_{0.1}As_2$	5	2.08(3)	22	0.003	1.2(5)	102.6(4)
$BaFe_{1.88}Mn_{0.12}As_2$	6	2.05(2)	≥ 26	0.013	0.7(5)	$\geq$ 30.7(3)
$BaFe_{1.895}Co_{0.100}Mn_{0.005}As_2$	0.25	2.06(2)	6	0.0008	0.8(5)	92.3(3)
$Ba_{0.8}Eu_{0.2}Fe_{1.9}Co_{0.1}As_2$	20	2.04(2)	4	0.32	1.4(8)	5.0(3)
$Ba_{0.99}Eu_{0.01}Fe_{1.9}Co_{0.1}As_2$	1	2.04(2)	2	0.002	0.5(4)	15.7(3)
$Lu_{1-x}Gd_xNi_2B_2C$	0.5	2.035(7)	0.3	0.3	10(4)	11(3)
$Y_{1-x}Gd_xNi_2B_2C$	2.1	2.03(3)	0.9	0.9	9(3)	10(2)
$La_{1-x}Gd_xSn_3$	0.4	2.010(10)	0.5	0.5	20(2)	≈20

Table 5.3: Experimental and calculated parameters for compounds of the $Ba_{1-x}Eu_xFe_{2-y}TM_yAs_2$ series.

not apply. Consequently, the exchange parameter extracted from the AG equation is not equal to the ESR experimental value and the calculated T_c suppression, ΔT_c^{AG}, will be different from the experimental one, ΔT_c^{exp}. Table 5.2 displays the calculated $\langle J^2(q)\rangle^{1/2}$ for key compounds in the $Ba_{1-x}Eu_xFe_{2-y}TM_yAs_2$ series and also for two conventional superconductors (RNi$_2$B$_2$C and LaSn$_3$). For the FeAs compounds $\Delta T_c = T_c - T_{c,0}$ was obtained in comparison with the optimally doped $BaFe_{1-x}Co_xAs_2$ ($T_{c,0} = 26$ K).

One can clearly see that the $\langle J_{fs}^2(q)\rangle^{1/2}$ values calculated by the AG equation are not in agreement with the ESR values when the impurity substitution is in the FeAs plane. On the other hand, Eu-substituted compounds exhibit a good agreement with the calculated values. This is an evidence that the FeAs compounds do not behave as conventional superconductors. Nevertheless it is clear that a non-conventional magnetic impurity pair-breaking is present and must be associated with the local Cu^{2+} and Mn^{2+} spins, as previously discussed. Furthermore, this non-conventional magnetic impurity pair-breaking mechanism decreases as a function of pressure. Therefore, to gain qualitative insight about this new pair breaking mechanism, we propose a simple spin-dependence of ΔT_c with the impurity magnetic spin (S) and with pressure (P):

$$\Delta T_c = S(S+1)(a - bP), \tag{5.6}$$

where $\Delta T_c = T_{c,0} - T_c$ and $a - b$ are parameters to be determined by the T_c values at ambient pressure and at the maximum applied pressure. We choose a linear dependence with pressure motivated by the same dependence of the Kondo temperature (T_K) on pressure in several Ce-based heavy fermion compounds [135, 136, 137, 138, 139]. It is well known for these materials that pressure enhances both valence fluctuations and the hybridization between $4f$ and conduction band electron states. As a result, the Kondo temperature increases.

By applying equation 5.6 to the Cu^{2+} ($S = 1/2$) compound ($T_c = 4$ K at $P = 0$ and $T_c = 10$ K at $P = 23$ kbar) we obtained the linear fit displayed in Fig. 5.22. Subsequently, by using the same linear dependence for the Mn^{2+} compound and changing only the spin to $S = 5/2$ we obtained a low limit for the critical pressure $P_c \sim 66$ kbar necessary for the emergence of superconductivity. This critical pressure value is in agreement with the experimental fact that no superconducting transition was observed for the Mn-substituted compounds up to 25 kbar (see Fig. 4.2.1b). In fact, the real critical pressure could be even higher due to effects of short-range Neel pair-breaking fluctuations that were not taken into account [140].

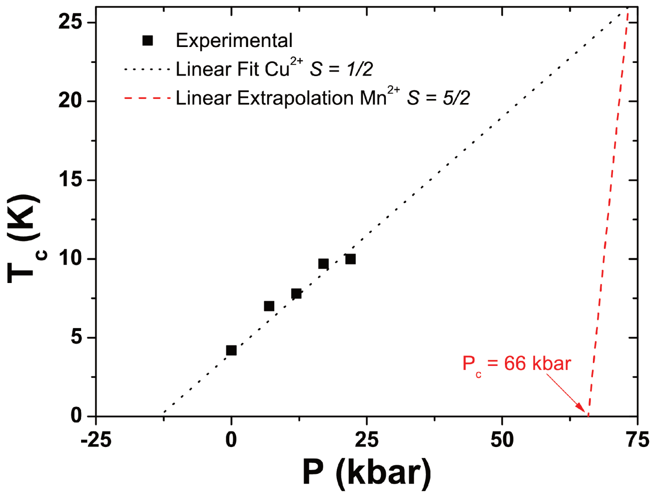

Figure 5.22: Linear fit of T_c as a function of pressure for Mn- and Cu-substituted compounds.

For completeness, we finish this chapter with the study of the magnetic analog $EuIn_2As_2$ that has a comparable Eu antiferromagnetic transition temperature ($T_N = 16$ K) with $EuFe_2As_2$ ($T_N = 16$ K) but no contributions of the Fe $3d$ bands to the Fermi surface. Its smaller ordering temperature is in agreement with the smaller separation between Eu first neighbors ions (a= 3.907 Å) in comparison with $EuIn_2As_2$ where a= 4.2067 Å .

$EuIn_2As_2$ crystallizes in the hexagonal $P6_3/mmc$ space group ($a = 4.207$ Å and $c = 17.889$ Å) which contains layers of Eu^{2+} cations separated by $[In_2As_2]^{2-}$ layers along the crystallographic c-axis. The field-dependent magnetic susceptibility shows an anisotropy with respect to crystallographic orientation below $T \sim 45$ K and an AFM ordering at $T_N = 16$ K. The anisotropic low-T data also indicate that there are both strong ferromagnetic intra-layer and weaker AFM inter-layer magnetic interactions between the Eu^{2+} ions. Transport measurements revealed negative colossal magnetoresistance which presumably evolves to some extent from the magnetic scattering of the conduction electrons (ce) by the Eu^{2+} spins [141].

The global physical properties of our single crystals of $EuIn_2As_2$ are presented in Fig. 5.23.

Panel a) of Fig. 5.23 displays the magnetic susceptibility as a function of temperature for a magnetic field $H = 1$ kOe applied parallel to the hex-plane and to the c-axis. $\chi(T)$ shows a Curie-Weiss (CW) behavior at high-T followed by an AFM transition at $T_N = 16\,K$, as previously reported [141]. From the CW magnetic susceptibility fittings for $T < T_N$ (solid lines in Fig. 5.23a) we obtained for both directions a CW temperature of $\theta_{CW} \approx 16$ K and an effective moment of $\mu_{eff} \approx 7.4\mu_B$ for Eu^{2+} in $EuIn_2As_2$, which is in agreement with the theoretical value.

The T-dependence of electrical resistivity measured in our single crystals of $EuIn_2As_2$ is shown in Fig.5.23b. A metallic behavior is observed in the paramagnetic regime and a clear peak appears at $T_N = 16$ K. This peak resembles the behavior observed for EuB_6 single crystals where the presence of magnetic polarons dominate the electron scattering near the ferromagnetic transition [142].

The AFM transition can also be clearly observed in lower panel c) of Fig.5.23, which shows the specific heat per mole divided by temperature. The sharp main peak in C/T corresponding to the onset of AFM order can be seen at $T_N \approx 16\,K$ in very good agreement with the temperature where the maximum in the magnetic susceptibility occurs (see Fig.5.23a). The estimated magnetic entropy recovered at T_N roughly reaches the value of Rln8 expected for the whole Eu^{2+} S= 7/2 (not shown).

Figure 5.24 shows the ESR spectra measured at T= 100 K at X-Band and Q-Band. In both cases we observe a single ESR resonance with a Dysonian lineshape resonance which is characteristic of localized magnetic moments in a lattice with a skin depth smaller than the size of the sample particles [75]. From the fitting of the resonances to the appropriate admixture of absorption and dispersion, we obtain at T= 100 K a g-factor $g = 1.95(1)$ and linewidth $\Delta H = 600(30)$ Oe in X-Band and $g = 1.98(1)$ and $\Delta H = 660$ (30) Oe for Q-Band for $H||c$. On the other hand, for H||hex-plane we obtain at T= 100 K a g-factor $g = 2.00(1)$ and linewidth $\Delta H = 480(20)$ Oe in X-Band and $g = 2.01(1)$ nd $\Delta H = 470$ (20) Oe for Q-Band.

Using the g-value of Eu^{2+} in insulators as 1.993(2) we extract for both bands an apparent small g-shift which is negative ($\Delta g < 0$) for H $||c$ and positive ($\Delta g > 0$) for H ||hex-plane [74]. This small effect may be an indicative of an anisotropic Eu^{2+}–Eu^{2+} magnetic coupling which seems to be consistent with the previous suggestion that there are ferromagnetic Eu^{2+}–Eu^{2+} interactions in the hex-plane and a weaker antiferromagnetic Eu^{2+}–Eu^{2+} interactions between the layers [141]. However, we can not rule out the contribution of demagnetization effects on this apparent g-

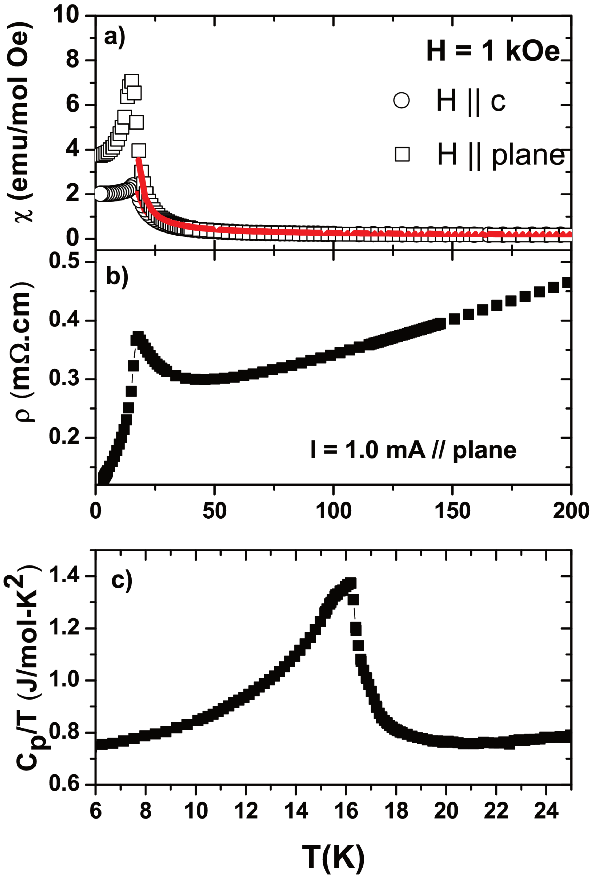

Figure 5.23: Temperature dependence of macroscopic physical properties of $EuIn_2As_2$ single crystals. a) Magnetic susceptibility with applied field H= 1kOe parallel to the *hex*-plane and to the *c*-axis. b) Electrical in-plane resistivity. c) Specific heat per mole divided by temperature.

anisotropy.

Interestingly, the Eu^{2+} ESR ΔH also show an anisotropic behavior in Fig. 5.24. ΔH is clearly narrower for the H ||hex-plane orientation for both X and Q-Bands. Furthermore, the Eu^{2+} ESR ΔH is nearly frequency/field independent for H ||hex-plane but show a measurable broadening at Q-band for H $||c$.

The ΔH and the g-value temperature dependence of the ESR line of $EuIn_2As_2$ for both X-Band and Q-Band is presented in Figure 5.25. For both bands, ΔH shows a nearly constant behavior for $T > 100$ K indicating an absence of Korringa-like relaxation of Eu^{2+} spins in this temperature region. At lower temperatures, the ESR ΔH starts to broaden as a consequence of the development of short range magnetic correlation. The X-Band data show a linewidth maxima at $\sim 16\,\mathrm{K}$ for

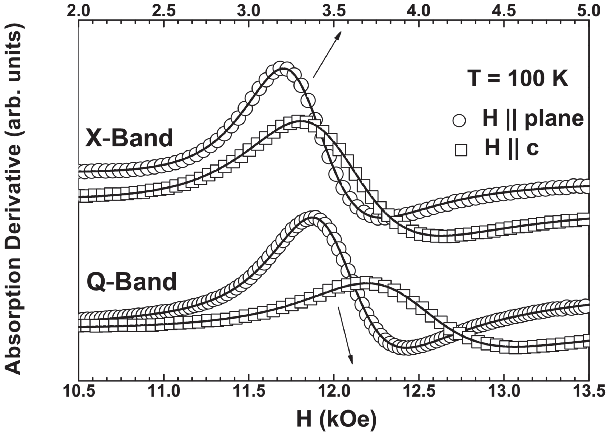

Figure 5.24: X and Q-Band Eu^{2+} ESR spectra at T= 100K for H parallel to the hex-plane and to the c-axis of $EuIn_2As_2$ single crystals.

both orientations. It is worth noting that ESR linewidth maxima do not necessarily occur at T_N as it can be affected by the details of the field dependent short range correlations. These correlations define how the distribution of local fields decrease as the long range ordered state develops. For fields of $\sim 1\,T$ (Q-Band) the magnetic susceptibility data show that T_N slightly decreases for H||c. For H||hex-plane no AFM transition is observed, suggesting that the H||hex-plane orientation is the easy axis for a weak ferromagnetic ordering (canted antiferromagnetism). The Q-Band data show a slightly higher linewidth maximum temperature for H||c, suggesting that at higher fields, stronger magnetic correlations start to affect the Eu^{2+} ESR linewidth at higher-T. At the same temperature regions, we observe a strong anisotropy in the g-value which is probably associated with the anisotropic internal field felt at the Eu^{2+} site. The internal field is also dependent on the applied magnetic field direction and strength. In particular we note that the Q-Band g-factor for H||plane increases strongly due to the presence of weak ferromagnetic ordering.

In order to understand the anisotropic field and temperature dependence of the ESR ΔH shown in Fig. 5.24 and 5.25, different contributions to the ESR linewidth must be considered. There are two types of resonant line broadening in solids: homogeneous and inhomogeneous broadening. Homogeneous ESR linewidth is inversely proportional to the so-called $spin-spin$ relaxation time, T_2 [74]. It occurs when the magnetic resonance signal results from a transition between two levels of spins which are not sharply defined, but instead, are somewhat intrinsically broadened. The main contributions to homogeneous broadening are: (1) dipolar interaction between like spins, (2) spin-lattice interaction, (3) interaction with radiation field, (4) diffusion of excitation throughout the sample, and (5) motionally narrowing fluctuations of local fields [74, 78].

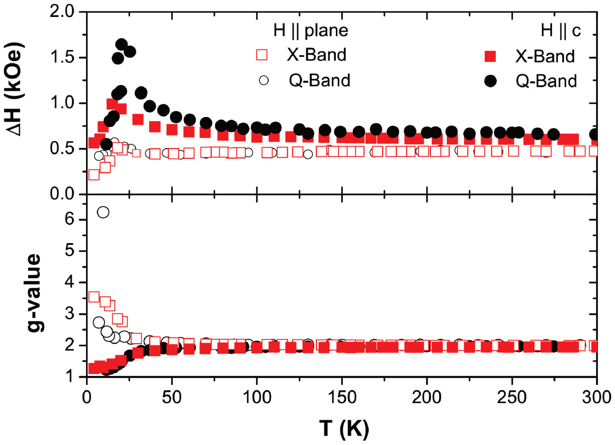

Figure 5.25: Temperature dependence of Eu^{2+} ESR ΔH and g-factor in Q- and X-Bands.

On the other hand, an inhomogeneously broadened resonant line is one which consists of a spectral distribution of individual lines merged into an overall line or envelope. For instance, a distribution of local fields caused by unresolved fine and/or hyperfine structure, g-value anisotropy, strain distribution and/or crystal irregularities that exceed the natural linewidth ($2/\gamma T_2$, γ is the gyromagnetic factor) will cause the spins in various parts of the sample feel different field strengths [74, 78].

In this way the resonance will be artificially broadened in an inhomogeneous manner. In the cases of inhomogeneous broadening caused by g-value anisotropy and related strain distribution and/or crystal irregularities, the ESR linewidth are expected to increase as a function of magnetic field. From the ΔH on data in Fig. 5.25 we can conclude that anisotropic ESR ΔH revealed a small inhomogeneous contribution when $H||c$ its a measurable broadening at Q-band.

To further explore the microscopic origin of the Eu^{2+} ESR ΔH anisotropy and its small inhomogeneous contribution when $H||c$ we have performed detailed angular dependent ESR and electrical resistivity experiments in the paramagnetic regime, Fig. 5.26. The comparison between the anisotropy in Eu^{2+} ESR ΔH with that in the electrical resistivity is important in this case because an anisotropic exchange interaction between the Eu^{2+} $4f$ electrons and the *ce* would result in similar angular dependence of both physical quantities [142].

In Fig. 5.26, we observe a small anisotropy in the resistivity that increases with applied magnetic field when the field is rotated from hex-plane to the c-axis. The resistivity values are systematically larger for $H||c$. On the other hand, ESR ΔH shows a much larger anisotropy but it also increases with H, being larger for Q-Band. Although the ΔH is also larger for $H||c$ the angular dependence of the ΔH is obviously very distinct from that in the resistivity. This indicates that the anisotropy in these physical quantities can not have an unique common origin.

In fact the anisotropy found for Eu^{2+} ESR ΔH is reminiscent of the crystalline electrical field (CEF) anisotropy found for S= 7/2 ions in hexagonal systems [143, 144, 145]. Therefore, the Eu^{2+} ESR ΔH in $EuIn_2As_2$ is mainly a result of an exchanged narrowed ΔH with a distribution of local fields caused by unresolved fine (CEF splitting) and perhaps hyperfine structure. As such, for $H||c$, the CEF splitting is larger and generates a broader envelope line. In this direction, this inhomogeneous contribution in ΔH is large enough to overcome the exchange narrowing effect and present the broadening in Q-band.

Therefore, the small anisotropy in the resistivity data may reflect to some extent an anisotropic magnetic scattering due to an anisotropic exchange interaction between the Eu^{2+} $4f$ electrons and the *ce*. However this effect, if present in the Eu^{2+} ESR ΔH anisotropy, would be overcome by the hexagonal crystal field and the Eu^{2+}-Eu^{2+} exchange narrowing effect.

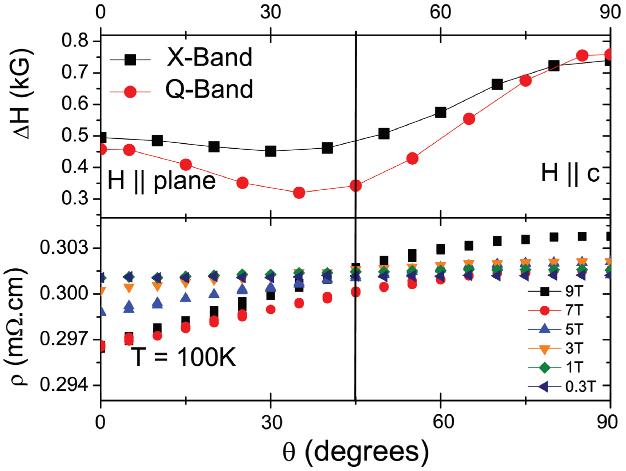

Figure 5.26: (upper panel) Q- and X-Bands Eu^{2+} ESR ΔH anisotropy at T = 100 K. (lower panel) Resistivity anisotropy for several applied magnetic fields at T = 100 K.

In a broader scenario it is interesting to compare these results for $EuIn_2As_2$ with the Fe-analog $EuFe_2As_2$. The absence of Korringa behavior for concentrated $EuIn_2As_2$ for $T > 100\,K$ provides an irrefutable confirmation that the behavior described above for the FeAs-based compounds is indeed due to the relaxation of Eu^{2+} via Fe 3d-electrons.

Chapter 6

Conclusions and Perspectives

In this work we presented a systematic study of the intermetallic tetragonal compound $BaFe_2As_2$ (space group $I4/mmm$) as a function of three parameters: Eu substitution in the Ba crystallographic site, transition metal (TM) substitution (TM = Mn, Co, Ni, Cu, and Ru) in the Fe site, and/or applied hydrostatic pressure. Our main goal consisted in understanding the microscopic interplay between magnetism and superconductivity in this class of materials. For this purpose, we have grown approximately 400 single crystals with Sn-, In- and/or FeAs- fluxes. In particular, our innovative In-flux method has resulted in extremely high quality single crystals which allowed us to obtain higher transition temperatures, narrower NMR lines, and less disordered crystals.

Initially, we have found by EXAFS measurements that both applied pressure and K-/Co-substitutions are responsible for a shortening of the Fe-As bond length accompanied by a suppression of the SDW magnetic phase. Furthermore, our XANES measurements indicated no observable change in the Fe K edge spectra of $BaFe_2As_2$ under Co substitution, implying that Co is not charge doping the Fe ions. Secondly, our ESR data for $Ba_{1-x}Eu_xFe_2As_2$ have shown that a decrease in the Eu concentration x induces a decrease of the Korringa rate in the paramagnetic state. To understand this result, we have studied the $EuIn_2As_2$ compound that showed no Korringa behavior, indicating that the bands with appreciable overlap with the Eu^{2+} $4f$ states are the $3d$ Fe conduction bands at the Fermi surface. Therefore, analysing our results in the presence of $e-e$ exchange enhancement and $\mathbf{q}$-dependent exchange interaction, $J_{fs}(\mathbf{q})$, we inferred that a decrease in $J_{fs}(\mathbf{q})$ reflects the fact that the $3d$ electron bands are becoming more anisotropic (less s-like) and are, in average, further away from the Eu^{2+} sites in real space. We speculated that this behavior is associated to a partial localization of the Fe $3d$ electrons within the FeAs plane, i.e., an increase of the xy and/or x^2-y^2 orbital contributions to the $3d$ bands at the Fermi surface. In order to confirm such scenario, we have systematically studied $Ba_{1-x}Eu_xFe_{2-y}TM_yAs_2$ single crystals

(TM for transition metals Co, Cu, Mn, Ni, and Ru) probing both Ba and FeAs planes through substitution with Eu^{2+} and Mn^{2+}/Cu^{2+} respectively. We first used the $x_{Eu} = 0.20$ sample as a reference compound to probe how the spin dynamics evolves as a function of the transition metal substitution and we observed that the Korringa rate b systematically decreases with decreasing T_{SDW} independent of the substituted TM. Secondly, we performed ESR experiments with paramagnetic probes in the FeAs plane Mn^{2+}/Cu^{2+} and we observed an increase of the Korringa rate with decreasing T_{SDW}, as expected. However, there is no unambiguous systematics between the magnitude of the SDW phase suppression and the magnitude of the Korringa rate suppression, specially for the ruthenium substitution. This is because the particularities in the bands' distortions can behave differently for each transition metal. For instance, if the substitution is not coherent, interference can occur between the $3d$ bands and consequently suppress more effectively b than T_{SDW}. In addition, we have also performed electrical resistivity measurements under hydrostatic pressure in $BaFe_{1.9}TM_{0.1}As_2$ (TM = Mn, Co, Cu, and Ni) single crystals with applied pressures up to $P \lesssim 25$ kbar motivated by the fact that the localization effects mentioned above are not the only parameters that matter when it comes to the emergence of USC. Not only we must suppress the SDW magnetic phase by tuning a control parameter, but the emergent superconducting state has to be robust against competing order parameters and pair-breaking mechanisms (such as Cu, Mn and Cr local moments) associated with substitution and/or strain. Our results demonstrated constrasting behavior of hydrostatic pressure effects on nearly optimally substituted $BaFe_{2-x}TM_xAs_2$ (TM = Co, Cu, and Ni) high quality single crystals grown using the In-flux method. For Co and Ni-substitution, T_c increases only ~ 2 K at a rate $dT_c/dP \sim 0.1$ K/kbar, consistent with the nearly optimal doping region. On the other hand, in the Cu-substituted sample T_c increases ~ 6 K at a rate $dT_c/dP \sim 0.3$ K/kbar. This huge T_c enhancement by a factor of ~ 2.5 with pressure and the local Cu^{2+} ESR line provide strong evidence that the hybridization between the Cu $3d$ bands and the conduction bands increases with pressure and, consequently, the impurity scattering by the Cu local moments decreases due to the pressure induced delocalization of the Cu $3d$ electrons.

In summary, our results have shown that the tuning of a microscopic local structural parameter (the Fe-As distance) is directly related to the suppression of the SDW magnetic phase in the iron-pnictides. In addition, this decrease in d_{FeAs} changes the crystal field scheme for these compounds and induces an increase of the xy/x^2-y^2 orbital contributions to the $3d$ bands at the Fermi surface. We speculate that these orbitals are related to the superconducting pairing, as in the case of the cuprates.

Although we have a solid scenario for the physical properties of the $BaFe_2As_2$ compound, the present work opens the possibility of further systematic ESR studies of the superconducting state, the investigation of electrical resistivity at higher pressures (diamond anvil pressure cell) and the search for a generalization of our results to other families of iron-based SCs. But most importantly, the results constructed during this thesis, together with the knowledge gathered in other families of unconventional superconductors, may guide the search for new superconductors.

Appendix A

List of Publications

The papers published during this thesis are enumerated cronologically in the following list. The publications directly related to the results discussed in the text are marked with an asterisk.

1. ***P. F. S. Rosa**, B. Zeng, C. Adriano, T. M. Garitezi, T. Grant, Z. Fisk, L. Balicas and P. G. Pagliuso. Quantum oscillations in the parent pnictide $EuFe_2As_2$. To be submitted to Physical Review B.

2. C. Adriano, F. Rodolakis, **P. F. S. Rosa**, D. Ai, J. Zhao, M. A. Continentino, Z. Fisk, J. C. Campuzano, and P. G. Pagliuso. Probing the hybridization gap in heavy fermions by temperature dependent ARPES. To be submitted to Nature Communications.

3. ***P. F. S. Rosa**, C. Adriano, T. M. Garitezi, T. Grant, Z. Fisk, and P. G. Pagliuso. Pressure effect on magnetic pair-breaking in Cu-substituted $BaFe_2As_2$ single crystals. To be submitted to Phys. Rev. Lett.

4. ***P. F. S. Rosa**, C. Adriano, T. M. Garitezi, T. Grant, Z. Fisk and P. G. Pagliuso . Site specific spin dynamics in $BaFe_2As_2$. To be submitted to Phys. Rev. Lett.

5. **P. F. S. Rosa**, L. A. S. de Oliveira, C. B. R. de Jesus, K. O. Moura, C. Adriano, W. Iwamoto, T. M. Garitezi, K. R. Pirota, and P. G. Pagliuso. Low-dimensional magnetic frustration in intermetallic nanowires. Submitted to Nature Nanocommunications in 07-12-2013 (NCOMMS-13-06345).

6. C. B. R. de Jesus, **P. F. S. Rosa**, T. M. Garitezi, G. G. Lesseux, R. R. Urbano, C. Rettori, and P. G. Pagliuso. Electron spin resonance of the half-Heusler antiferromagnet GdPdBi. Submitted to Solid State Communications on 08-05-2013.

7. **P. F. S. Rosa**, W. Iwamoto, L. M. Holanda, R. A. Ribeiro, P. G. Pagliuso, C. Rettori, and M. A. Avila. Magnetic polaton effect in the $Sr_{8-x}Eu_xGa_{16}Ge_{30}$ clathrates probed by electron spin resonance. Phys. Rev. B. **87** 224414, 2013.

8. *T. M. Garitezi, C. Adriano, **P. F. S. Rosa**, E. M. Bittar, L. Bufaiçal, R. L. de Almeida, E. Granado, T. Grant, Z. Fisk, M. A. Avila, R. A. Ribeiro, P. L. Kuhns, A. P. Reyes, R. R. Urbano, and P. G. Pagliuso. Synthesis and characterization of $BaFe_2As_2$ single crystals grown by In-flux technique. Brazilian Journal of Physics, 43 (2013).

9. ***P. F. S. Rosa**, C. Adriano, W. Iwamoto, T. M. Garitezi, T. Grant, Z. Fisk, and P. G. Pagliuso. Evolution of Eu^{2+} spin dynamics in $Ba_{1-x}Eu_xFe_2As_2$. Phys. Rev. B. **86**, 165131 (2012).

10. ***P. F. S. Rosa** , C. Adriano, T. M. Garitezi, R. A. Ribeiro, Z. Fisk, and P. G. Pagliuso. Electron spin resonance of the intermetallic antiferromagnet $EuIn_2As_2$. Phys. Rev. B **86**, 094408 (2012).

11. O.F. de Lima, R. L. de Almeida, T. M. Garitezi, C. Adriano, **P. F. S. Rosa**, P. G. Pagliuso. Irreversibility lines and anomalous Meissner effect in $Ba(Fe_{1-x}Co_x)_2As_2$ superconducting crystals. Physics Procedia 36 (2012) 1661 - 1666.

12. *E. M. Bittar, C. Adriano, T. M. Garitezi, **P. F. S. Rosa**, L. Mendonça-Ferreira, F. Garcia, G, de M. Azevedo, P. G. Pagliuso, and E. Granado. Co-Substitution Effects on the Fe Valence in the $BaFe_2As_2$ Superconducting Compound: A Study of Hard X-Ray Absorption Spectroscopy. Phys. Rev. Lett. **107**, 267402 (2011).

13. *E. Granado, L. Mendonça-Ferreira, F. Garcia, G. de M. Azevedo, G. Fabbris, E. M. Bittar, C. Adriano, T. M. Garitezi, **P. F. S. Rosa**, L. F. Bufaiçal, M. A. Avila, H. Terashita, and P. G. Pagliuso. Phys. Rev. B **83**, 184508 (2011).

Bibliography

[1] J. Paglione and R. L. Greene. High-temperature Superconductivity in Iron-Based Materials. *Nature Physics*, 6(645), 2010.

[2] Y. Kamihara et al. *J. Am. Chem. Soc.*, 130(3296), 2008.

[3] M. Rotter et al. *Physical Review B*, 78(02503(R)), 2008.

[4] G. R. Stewart. *Reviews of Modern Physics*, 83:1589–1652, 2011.

[5] P. G. Pagliuso et al. Multiple phase transition in Ce(Rh,Ir,Co)In_5. *Physica B: Condensed Matter*, 312:129–131, 2002.

[6] G. Knebel, D. Aoki, J.-P. Brison, and J. Flouquet. The quantum critical point in $CeRhIn_5$: A resistivity study. *J. Phys. Soc. Jpn.*, 77(114704), 2008.

[7] E. Hanamura, N. T. Dan, and Y. Tanabe. Excitonic cluster model of strongly correlated electronic systems. *J. Phys.: Condens. Matter*, 12(22), 2000.

[8] M. Hucker. Structural aspects of materials with static stripe order. *Physica C: Superconductivity*, 481:3–14, 2012.

[9] Y. Liu et al. Aliovalent ion-doped $BaFe_2As_2$: Single crystal growth and superconductivity. *Physica C: Superconductivity*, 470:S513–S515, 2010.

[10] H. Wadati, I. Elfimov, and G. A. Sawatzky. *Physical Review Letters*, 105(157004), 2010.

[11] A. Khasanov et al. Mossbauer studies of the superconducting cobalt/nickel-doped $BaFe_2As_2$. whither go the injected electron(s)? *J. Phys.: Condens. Matter*, 23(202201), 2011.

[12] J. Munevar et al. Interplay between superconductivity and antiferromagnet ism in some iron-pnictides single crystals studied by ^{57}Fe mossbauer spectroscopy. *http://arxiv.org/pdf/1111.5853v1*, 2011.

[13] G. Levy et al. Probing the role of Co substitution in the electronic structure of iron pnictides. *Physical Review Letters*, 109(07701), 2012.

[14] S. Ideta et al. Dependence of carrier doping on the impurity potential in transition-metal-substituted FeAs-based superconductors. *Physical Review Letters*, 110(107007), 2013.

[15] P. G. Pagliuso et al. Structurally tuned superconductivity in heavy-fermion CeMIn_5 ($M =$ Co, Ir, Rh). *Physica B: Condensed Matter*, 320(1-4), 2002.

[16] P. G. Pagliuso et al. *J. Appl. Phys.*, 99(08P703), 2006.

[17] K. Kubo and T. Hotta. Orbital-controlled superconductivity in f-electron systems. *J. Phys. Soc. Jpn.*, 75(083702), 2006.

[18] E. Bauer et al. *Physical Review Letters*, 93(147005), 2004.

[19] H. Sakakibara et al. Multiorbital analysis of the effects of uniaxial and hydrostatic pressure on T_c in the single-layered cuprate superconductors. *Physical Review B*, 86(134520), 2012.

[20] Y. Ohta et al. Apex oxygen and critical temperature in copper oxide superconductors: Universal correlation with the stability of local singlets. *Physical Review B*, 43(2968), 1991.

[21] J. D. Jorgensen et al. Structural features that optimize high temperature superconductivity. *Recent Developments in High Temperature Superconductivity.Lecture Notes in Physics*, 475:1–15, 1996.

[22] J. D. Thompson et al. Interplay of magnetism, structure and superconductivity in heavy-fermion systems CeMIn$_5$ and PuMGa$_5$. *J. Alloys and Compounds*, 408(9):16–20, 2006.

[23] Z. P. Yin, K. Haule, and G. Kotliar. Kinetic frustration and the nature of the magnetic and paramagnetic states in iron pnictides and iron chalcogenides. *Nature Materials*, 10:932–935, 2011.

[24] P. Richard et al. Fe-based superconductors: an angle-resolved photoemission spectroscopy perspective. *Rep. Prog. Phys.*, 74, 124512 (2011).

[25] M. D. Limsden and A. D. Christianson. Superconductivity in iron compounds. *J. Phys.: Condens. Matter*, 22 203203 (2010) and references therein.

[26] R. A. Ewings et al. Itinerant spin excitations in SrFe$_2$As$_2$ measured by inelastic neutron scattering. *Physical Review B*, 83(214519), 2011.

[27] S. Ikeda et al. Magnetic Interactions on Single-Crystal EuFe$_2$As$_2$ studied by ^{57}Fe Mossbauer spectroscopy. ,

[28] H. S. Jeevan et al. Electrical resistivity and specif heat of single-crystalline $\mathrm{EuFe_2As_2}$: a magnetic analog of $\mathrm{SrFe_2As_2}$. *Phys. Rev. B*, 78 052502 (2008).

[29] H. S. Jeevan et al. Interplay of antiferromagnetism, ferromagnetism, and superconductivity in $\mathrm{EuFe_2(As_{1-x}P_x)_2}$ single crystals *Phys. Rev. B*, 83 054511 (2011).

[30] H. S. Jeevan et al. Superconductivity and magnetism in K-doped $\mathrm{EuFe_2As_2}$. *J. Phys.: Condens. Matter*, 21 265701 (2009).

[31] S. Jiang et al. Superconductivity and local-moment magnetism in $\mathrm{Eu(Fe_{0.89}Co_{0.11})_2As_2}$ *Phys. Rev. B*, 80 184514 (2009).

[32] C. F. Miclea et al. Evidence for a reetrant superconducting state in $\mathrm{EuFe_2As_2}$ under pressure. *Phys. Rev. B*, 79 212509 (2009).

[33] J. H.-Martin et al. Magnetic structure of $\mathrm{EuFe_2As_2}$ as determined by resonant x-ray scattering. *Phys. Rev. B*, 80 134411 (2009).

[34] K. H. J. Buschow and F. R. de Boer. *Physics of Magnetism and Magnetic Materials.* Kluwer, New York 2003.

[35] M. Tinkham. *Introduction to Superconductivity.* McGraw-Hill, 1975.

[36] A. A. Abrikosov and L. P. Gorkov. Contribution to the theory of superconducting alloys with paramagnetic impurities. *Soviet Physics JETP*, 12, 6 (1961).

[37] J. L. Sarrao et al. Plutonium-based superconductivity with a transition temperature above 18 K. *Nature*, 420, 6913 (2002).

[38] T. Moriya and K. Ueda. Spin fluctuations and high temperature superconductivity. *Advances in Physics*, 49, 555 (2000).

[39] A. Chubukov Pairing mechanism in Fe-based superconductors. *Annual review of Condensed Matter Physics*, 3 57 (2012).

[40] R. Flint and P. Coleman Heavy electrons and the sympletic symmetry of spin. *Nature Physics*, 8 643 (2008).

[41] T. Tzen Ong and P. Coleman Local Quantum Criticality of an Iron-Pnictide Tetrahedron. *Phys. Rev. Lett.*, 108 107201 (2012).

[42] E. Dengler et al. Strong reduction of the Korringa relaxation in the spin-density wave regime of $\mathrm{EuFe_2As_2}$ observed by electron spin resonance. *Physical Review B*, 81(024406), 2010.

[43] N. Pascher et al. *Physical Review B*, 82(054525), 2010.

[44] J. J. Ying et al. *Physical Review B*, 81(052503), 2010.

[45] F. A. Garcia et al. *New. J. Phys.*, 14(063005), 2012.

[46] N. W. Aschroft and N. D. Mermin. *Solid State Physics.* Saunders College, Philadelphia, 1976.

[47] K. N. R. Taylor and M. I. Darby. *Physics of Rare Earth Solids.* Chapman and Hall Ltd, 1972.

[48] E. C. Stoner Collective electron ferromagnetism *Proceedings of the Royal Society A.* 165. 922 (1938).

[49] L. P. Gor'kov The G-L equations from BCS *Sov-Phys. JETP* 9, 1364 (1959).

[50] P. W. Anderson Theory of dirty superconductors *J. Phys. Chem. Solids.* 11, 26 (1959).

[51] Y. Nambu *Phys. Rev.* 117, 648 (1960).

[52] G. M. Eliashberg Theory of dirty superconductors *Sov. Phys. JETP* 11, 696 (1960).

[53] J. R. Schrieffer, D. J. Scalapino and J. W. Wilkins *Phys. Rev. Lett.* 10, 336 (1963).

[54] B. T. Matthias, et al *Proc. Natl. Acad. Sci.* 64, 459 (1969).

[55] E. Bucher, et al *Phys. Rev. B* 11, 440 (1975).

[56] F. Steglich, et al *Phys. Rev. Lett.* 43, 1892 (1979).

[57] M. R. Norman. *Unconventional Superconductivity.* Book chapter for "Novel Superfluids", vol. 2, eds. K. H. Bennemann and J. B. Ketterson, Oxford University Press.

[58] J. G. Bednorz and K. A. Muller *Z. Phys. B* 64, 189-193 (1986).

[59] G. E. Pake and T. L. Estle *The Physical Principles of Electron Paramagnetic Resonance.* W. A. Benjamin, 1973.

[60] F. de Groot et al. *J. Phys.: Condens. Matter* 21, 104207 (2009).

[61] R. A. Bair and W. A. Goddard *Phys. Rev. B* 22, 2767 (1980).

[62] B. Ravel and M. Newville *J. Synchrotron Radiat.* 12, 537 (2005).

[63] S. Blundell. *Magnetism in Condensed Matter.* Oxford University Press, 2001.

[64] H. K. Onnes. *Commun. Phys. Lab. Univ. Leiden. Suppl.*, 29, 1911.

[65] N. E. Phillips. Heat capacity of aluminum between 0.1° K and 4.0° K. *Phys. Rev.*, 114(3):676–685, 1959.

[66] C. Petrovic et al. Heavy-fermion superconductivity in $\mathrm{CeCoIn_5}$ at 2.3 k. *J. Phys.: Condens. Matter*, 13(17), 2001.

[67] N. J. Curro et al. Unconventional superconductivity in $\mathrm{PuCoGa_5}$. *Nature*, 434(622-625), 2005.

[68] H. Kontani and S. Onari. Orbital-fluctuation-mediated superconductivity in iron pnictides: Analysis of the five-orbital hubbard-holstein model. *Physical Review Letters*, 104(157001), 2010.

[69] J. P. Hague et al. Unconventional pairing in bipolaronic theories. *Physica C: Superconductivity*, 460:1121–1122, 2007.

[70] P. W. Anderson. The resonating valence bond state in $\mathrm{La_2CuO_4}$ and superconductivity. *Science*, 235(4793):1196–1198, 1987.

[71] I. I. Mazin. Superconductivity gets an iron boost. *Nature*, 464:183–186, 2010.

[72] D. S. Inosov et al. Normal-state spin dynamics and temperature-dependent spin-resonance energy in optimally doped $\mathrm{BaFe_{1.85}Co_{0.15}As_2}$. *Nature Physics*, 6(1483):178–181, 2010.

[73] M. Yi et al. Symmetry-breaking orbital anisotropy observed for detwinned $\mathrm{Ba(Fe_{1-x}Co_x)_2As_2}$ above the spin density wave transition. *PNAS*, 108(17), 2010.

[74] A. Abragam and B. Bleaney. *EPR of Transition Ion.* Clarendon Press, Oxford, 1970.

[75] F. J. Dyson. *Phys. Rev.*, 98:349, 1955.

[76] A. Narath and H. T. Weaver. *Phys. Rev.*, 175(373), 1968.

[77] R. W. Shaw and W. W. Warren. *Physical Review B*, 3(1562), 1971.

[78] C. P. Poole and H. A. Farach. *Relaxation in Magnetic Resonance.* Academic Press, 1971.

[79] S. E. Barnes. Theory of electron spin resonance of magnetic ions in metals. *Adv. in Physics*, 30(6):801–938, 1981.

[80] Z. Fisk and J. P. Remeika. *Growth of single crystals from molten metal fluxes*, volume 12. Elsevier Science Publishers, chapter 81 edition, 1989.

[81] *Physical Property Measurement System - Heat Capacity Option User's Manual.*

[82] *Physical Property Measurement System - Resistivity Option User's Manual*, 2004.

[83] *Application Note on Pcell 15/30*

[84] S. E. Sebastian. *Iron-based Superconductors - Materials, Properties and Mechanisms.* Pan Stanford, chapter 4: quantum oscillations in iron pnictide superconductors edition, 2012.

[85] M. McElfresh. *Fundamentals of magnetism and magnetic measurements. Featuring Quantum Design's magnetic property measurement system.*, 1994.

[86] D. C. Koningsberger and R. Prins. *X-ray absorption : principles, applications, techniques of EXAFS, SEXAFS, and XANES.* John Wikey, New York, NY, 1988.

[87] *EMX User's Manual*, 1995.

[88] A. S. Sefat et al. Structure and anisotropic properties of $BaFe_{2-x}Ni_xAs_2$ (x=0, 1, and 2) single crystals. *Physical Review B*, 79(094508), 2009.

[89] M. Rotter et al. Spin-density-wave anomaly at 140 k in the ternary iron arsenide $BaFe_2As_2$. *Physical Review B*, 78(020503(R)), 2008.

[90] S. Ishida et al. Manifestations of multiple-carrier charge transport in the magnetostructurally ordered phase of $BaFe_2As_2$. *Physical Review B*, 84(184514), 2011.

[91] M. A. Tanatar et al. Pseudogap and its critical point in the heavily doped $Ba(Fe_{1-x}Co_x)_2As_2$. from c-axis resistivity measurements. *Physical Review B*, 82(134528), 2010.

[92] S. K. Kim et al. Combined effects of pressure and ru substitution on $BaFe_2As_2$. *prb*, 84(134525), 2011.

[93] M. Rotter et al. Antiferromagnetic ordering and structural phase transition in $BaFe_2As_2$ with Sn incorporated from the growth flux. *Physical Review B*, 79(064504), 2009.

[94] E. D. Bauer et al. Electronic inhomogeneity in a Kondo lattice. *PNAS*, 108(6857), 2011.

[95] R. R. Urbano et al. Interacting antiferromagnetic droplets in quantum critical $CeCoIn_5$. *Physical Review Letters*, 99(146402), 2007.

[96] R. R. Urbano et al. Competing orders in underdoped $Ba_{1-x}K_xFe_2As_2$. *J. Phys. Conf. Ser.*, 273(012107), 2011.

[97] R. R. Urbano et al. Distinct high-t transitions in underdoped $Ba_{1-x}K_xFe_2As_2$. *Physical Review Letters*, 105(107001), 2010.

[98] K. Kitagawa et al. Commensurate itinerant antiferromagnetism in $\mathrm{BaFe_2As_2}$. ^{75}As-NMR studies on a self-flux grown single crystal. *J. Phys. Soc. Jpn.*, 77(114709), 2008.

[99] A. P. Dioguardi et al. Local magnetic inhomogeneities in $\mathrm{Ba(Fe_{1-x}Ni_x)_2As_2}$ as seen via ^{75}As NMR. *Physical Review B*, 82(140411(R)), 2010.

[100] S. -H. Baek et al. Microscopic ^{75}As NMR. study of the effect of impurities on the first-order spin-density-wave transition in $\mathrm{BaFe_2As_2}$. *Physical Review B*, 78(212509), 2008.

[101] J.-Ph. Reid et al. Nodes in the gap structure of the iron arsenide superconductor $\mathrm{Ba(Fe_{1-x}Co_x)_2As_2}$ from c-axis heat transport measurements. *Physical Review B*, 82(064501), 2010.

[102] Y. Nakajima et al. Suppression of the critical temperature of superconducting $\mathrm{Ba(Fe_{1-x}Co_x)_2As_2}$ by point defects from proton irradiation. *Physical Review B*, 82(220504(R)), 2010.

[103] N. Ni et al. Effects of Co substitution on thermodynamic and transport properties and anisotropic Hc2 in $\mathrm{Ba(Fe_{1-x}Co_x)_2As_2}$ single crystals. *Physical Review B*, 78(214515), 2008.

[104] M. A. Tanatar et al. Pseudogap and its critical point in the heavily doped $\mathrm{Ba(Fe_{1-x}Co_x)_2As_2}$ from c-axis resistivity measurements. *Physical Review B*, 82(134528), 2010.

[105] E. Arushanov et al. Scaling of the temperature-dependent resistivity in 122 iron-pnictide superconductors. *Supercond. Sci. Technol.*, 24(105004), 2011.

[106] N. Ni et al. Temperature versus doping phase diagrams for $\mathrm{Ba(Fe_{1-x}}TM_x\mathrm{)_2As_2}$ ($TM =$ Ni,Cu,Cu/Co) single crystals. *Physical Review B*, 82(024519), 2010.

[107] Z. Xu et al. Ni doping effect and phase diagram of Ni-doped $\mathrm{BaFe_2As_2}$. *Physica C*, 470:S447, 2010.

[108] A. Thaler et al. Physical and magnetic properties of $\mathrm{Ba(Fe_{1-x}Ru_x)_2As_2}$ single crystals. *Physical Review B*, 82(014534), 2010.

[109] H. Xiao et al. Filamentary superconductivity across the phase diagram of $\mathrm{Ba(Fe,Co)_2As_2}$. *Physical Review B*, 86(064521), 2012.

[110] M. G. Kim et al. *Physical Review Letters*, 109(167003), 2012.

[111] R. M. Fernandes et al. *Physical Review B*, 85(140512(R)), 2012.

[112] P. L. Alireza et al. *J. Phys.: Condens. Matter*, 21(012208), 2009.

[113] M. Rotter et al. *Physical Review Letters*, 101(107006), 2008.

[114] C. Wang et al. *EPL*, 83(67006), 2008.

[115] J. G. Analytis et al. Quantum oscillations in the parent pnictide $\mathrm{BaFe_2As_2}$: Itinerant electrons in the reconstructed state. *Physical Review B*, 80(064507), 2009.

[116] R. R. Urbano et al. *Physical Review Letters*, 105(107001), 2010.

[117] M. Rotter et al. *Physical Review Letters*, 101(107006), 2008.

[118] T. M. Garitezi et al. *Brazilian Journal of Physics*, 48(XXXXX), 2013.

[119] N. Ni et al. *Physical Review B*, 78(214515), 2008.

[120] Y. Su et al. *Physical Review B*, 79(064504), 2009.

[121] R. R. Urbano et al. *Physical Review B*, 73(115123), 2006.

[122] C. Rettori. *Physical Review B*, 10(1826), 1974.

[123] K. Yosida. *Phys. Rev.*, 106(893), 1957.

[124] J. Korringa. *Physica*, 16(601), 1950.

[125] D. Davidov. *Solid State Comm.*, 12(621), 1973.

[126] T. Moriya. *J. Phys. Soc. Jpn.*, 18(516), 1963.

[127] A. Narath. *Phys. Rev.*, 163(232), 1967.

[128] U. Alver. *Physical Review B*, 64(180402 (R)), 2001.

[129] T. Setti. *Electronic structure studies of ferro-pnictide superconductors and their parent compounds using angle-resolved photoemission spectroscopy (ARPES).* PhD thesis, Tech. Universitat Berlin, 2011.

[130] C. Krellner. *Physical Review B*, 78(100504), 2008.

[131] C. Feng et al. *Physical Review B*, 82(094426), 2010.

[132] P. G. Pagliuso et al. Electron spin resonance of Gd^{3+} in the normal state of $R\mathrm{Ni_2B_2C}$ ($R =$ Y,Lu). *Physical Review B*, 57(6), 1998.

[133] E. M. Bittar et al. Electron spin resonance study of the $\mathrm{LaIn}_{3-x}\mathrm{Sn}_x$ superconducting system. *Journal of Physics: Condensed Matter*, 23(45):455701, 2011.

[134] M. B. Maple Dependence of s-Æ exchange on atomic number in rare earth dialuminides *Solid State Communications*, 8 22, 1915-1917 1970.

[135] S. M. Ramos et al. Superconducting Quantum Critical Point in $\mathrm{CeCoIn}_{5-x}\mathrm{Sn}_x$. *Physical Review Letters*, 105, 126401 (2010).

[136] E. N. Hering et al. Pressure-temperature-composition phase diagram of $\mathrm{Ce}_2M\mathrm{In}_8$ (M = Rh, Ir) *Physica B: Condensed Matter,* 378 (2006).

[137] J. C. Cooley et al. High pressures and the Kondo gap in $\mathrm{Ce_3Bi_4Pt_3}$. *Physical Review B* 55, 12 (1997).

[138] A. Percheron et al. Resistivities of $\mathrm{CeAl_3}$ and $\mathrm{LaAl_3}$ compounds under pressure. *Solid State Communications* 12, 1289 (1973).

[139] B. Bellarbi et al. High-pressure valence instability and T_c maximum in superconducting $\mathrm{CeCu_2Si_2}$. *Physical Review B* 30, 1182 (1984).

[140] R. M. Fernandes and A. J. Millis. Suppression of superconductivity by Neel-type magnetic fluctuations in the iron pnictides. *Physical Review Letters* 110, 117004 (2013).

[141] A. M. Goforth et al. *Inorg. Chem.*, 47(23):11048–56, 2008.

[142] R. R. Urbano et al. *Physical Review B*, 70(140401(R)), 2004.

[143] P. M. Zimmerman et al. *Physical Review B*, 6(2783), 1972.

[144] J. Nagel and K. Baberschke. *Crystal Field Effects in Metals.* Plenum, New York, p. 66, edited by a. furrer edition, 1977.

[145] G. Lacueva et al. *Physical Review B*, 31(6245), 1985.